

Numerical study of flow boiling in micro/mini channels

Qingming LIU
刘清明

Doctoral thesis 2017

Supervisor
Björn E. Palm

Co-supervisor
Joachim Claesson

Department of Energy Technology
School of Industrial Engineering and Management
KTH Royal Institute of Technology
SE 100-44 Stockholm

ISBN 978-91-7729-342-2
TRITA-REFR Report 17/02
ISSN 1102-0245
ISRN KTH//REFR/17/02-SE

士不可以不弘毅

任重而道远

仁以为己任

不亦重乎

死而后已

不亦远乎

The unexamined life is not worth living.

Contents

Contents	i
Abstract	iii
Sammanfattning	1
Preface.....	2
Journal papers	2
Conference papers	2
Acknowledgement.....	3
1 Introduction.....	4
2 State of the art.....	7
2.1 Boiling phenomena.....	7
2.2 Computational fluid dynamics modeling of boiling.....	11
3 Numerical framework.....	15
3.1 Governing equations	15
3.2 Discretization schemes.....	17
3.3 Pressure-velocity coupling.....	19
3.4 Interface capturing methods.....	20
3.5 Phase change modeling.....	24
3.6 Initial and boundary conditions.....	25
3.7 Validations	25
Summary.....	33
4 Nucleate to confined bubbly flow transition.....	34
4.1 Boundary and initial conditions.....	34
4.2 A comparison with a visualization	35
4.3 A simple model of bubble merging	36
4.4 Multiple bubbles merging	43
4.5 Summary.....	48
5 Confined bubbly flow regime	50
5.1 Single confined bubble	50
5.2 Multi confined bubbles moving in micro channels	54

Summary.....	60
6 Slug to annular flow transition	60
6.1 Initial and boundary conditions.....	61
6.2 A validating case	62
6.3 Flow regime transition.....	64
6.4 Summary.....	71
7 Conclusions.....	73
7.2 Future plans and suggestions	74
Nomenclature.....	75
References	77

Abstract

Boiling phenomena in micro scale has emerged as an interesting topic (J. R. Thome, Revellin, Agostini, & Park, 2008) due to its complexity and increasing usage in micro electronic and mechanical systems (MEMS). Despite extensive research efforts (H. Chen, Xu, Xie, Xing, & Li, 2014; Dhir, Abarajith, & Li, 2007; Satish G. Kandlikar, 2010a), heat transfer mechanism remains unclear. There have been two ways to estimate the heat transfer coefficient of flow boiling in macro channels: 1) an average value for the whole boiling process, and 2) local heat transfer coefficient as a function of vapor quality. The latter method has been proven to be better in micro channels because different flow regimes have different heat transfer characteristics. Experimental visualization has discovered five main flow regimes: nucleate boiling, isolated bubbles, confined bubbly flow, elongated bubbly (or slug) flow, and annular flow. Two of these patterns (confined bubbles and slug flow) are rarely found in macro channels and are believed to have very different heat transfer mechanisms to that of nucleate boiling.

The development of a phenomenological model demands a deep understanding of each flow regime as well as the transition process between them. While studies in every individual flow pattern are available in literature, the mechanisms of transition processes between them remain mysterious. More specifically, how the isolated bubbles evolve into a confined bubbly flow, and how this further evolves into elongated bubbles and finally an annular flow. The effects of boundary conditions such as wall heat flux, surface tension, and interfacial velocity are unclear, too.

The novelties (or aims) of this thesis are to develop and validate a new numerical algorithm, perform a comprehensive numerical study on these transition processes, uncover the transition mechanisms and investigate effects of boundary and operating conditions.

Firstly, a sophisticated and robust numerical model is developed by combining a coupled level set method (CLSVOF) and a non-equilibrium phase change model, which enables an accurate capture of the two-phase interface, as well as the interface temperature.

Secondly, several flow regime transitions are studied in this thesis: nucleate bubbles to confined bubbly flow, multi confined bubbles moving consecutively in a micro channel, and slug to annular flow transition. Effects of surface tension, heat flux, mass flux, and fluid properties are examined. All these regimes are studied separately, which means an appropriate initial condition is needed for each regime. The author developed a simplified model based on energy balance to set the initial and boundary conditions.

The nucleate to confined transition process has been found to consist of three stages: sliding, merging and post-merging stages. The latter two stages are both extremely fast processes which take less than one millisecond. The dynamics and heat transfer are very different in these three stages.

After the merging of nucleate small bubbles, the larger confined bubbles move along the tube consecutively. The first bubble has the highest growth rate and the rest have similar lower growth rates. Their movements still obey the lubrication theory.

The transition from slug to annular regime is complicated where the expansion of the bubble makes a notch at the end of the annulus. This notch will contract and produce small droplets when the bubble and the annulus coalesce. The bubble growth is enhanced by the transition process.

Keywords: numerical, boiling, micro channel, phase change.

Sammanfattning

Flöda kokning i mikro-kanal har varit ett intressant forskning ämne på grund av sin komplexitet och ökande användning i mikro elektroniks och mekanikal systemer (MEMS). Fastan forskning ansträngning, vissa delar av fenomenon är fortfarande inte helt förstås.

Värmeöverföring mekanism är inte klart. Det finns två metoder att beräkna värmeöverföring koefficient av flöda kokning i makro kanaler: 1) ett genomsnitt värde för hela kokning processen; 2) lokal värmeöverföring som ett funktion av ånga kvalitet. Den senare metoden är bättre i mikro kanaler eftersom olika flytande regimen har olika värmeöverföring karakteristik. Experiment visningar har upptäckte fyra huvudsakliga flöda regimen: bubbelkokning, begränsad bubblig flöde, snigel flöde, och ringformig flöde. Två av de är sällan i makro kanaler och tros att ha väldig annorlunda värmeöverföring mekanism än bubbelkokning.

Utveckling av fenomenologikal modell behöver djup förståelse av varje flöde regimen och övergång processen mellan de. Medan studie på alla individuella flöde mönster är tillgängliga i litteraturer, mekanismer av övergångar processer vara kvar mystiska.

Syftet med denna avhandling är att utföra en omfattande numerisk undersökning av dessa övergångsprocesser. En sofistisk och robust numeriska modell utvecklas dess huvudsakliga nyhet är kombinationen av kopplade nivåinställning metod (CLSVOF) och en icke-jämviktas fasförändring modell, som möjliggör en ackurat tillfångatagande av två-fas-gränsytan, såväl som gränssnittstemperaturen.

De övergående flödesregimer som studerades i detta papper innefattar: bubblor till begränsad bubblande flöde, multibegränsade bubblor som konsekutivt rör sig i mikro-kanal, och slug till ringformigt flöde övergång. Effekter av ytspänning, värmefflöde, massflöde, och vätske egenskaper undersöks. Alla dessa regimer studeras separat, vilket innebär en lämplig inledande tillstånd behövs för varje regim. Författaren utvecklade förenklad modell baserad på energibalansen för att ställa in initiala och randvillkor.

Den bubbel till begränsad övergångsprocessen befinns vara bestod av tre faser: glidande, sammanslagning och efter sammanslagning stadier. De två senare stegen är båda extremt snabba processer som tar mindre än en millisekund. Dynamiken och värmeöverföring är mycket olika i dessa tre steg.

Efter sammanslagningen av bubbel små bubblor, större begränsade bubblorna rör sig längs röret i följd. Första bubblan har högsta tillväxthastighet. Deras rörelser följer fortfarande smörjning teori.

Övergång från slug till ringformig är komplicerad där expansionen av bubblan gör en skåra vid slutet av ringen. Detta hack kommer att krympa och producerar små droppar när bubblan och ringen sammansmältning. Den bubblornas tillväxten förstärks av övergångsprocessen .

Preface

This thesis consists of my six years work at the department of energy technology, KTH Royal Institute of technology and is based on four journal papers and two conference papers, which are listed below.

Journal papers

Liu, Q. and Palm, B. (2016). "Numerical study of bubbles rising and merging during convective boiling in micro-channels." *Applied Thermal Engineering* **99**:1141-1151.

Liu, Q. Wang, W. and Palm, B. (2017). "A numerical study of the transition from slug to annular flow in micro-channel convective boiling." *Applied Thermal Engineering* **112**:73-81.

Liu, Q. Wang, W. and Palm, B. (2017). "Numerical study of the interactions and merge of multiple bubbles in micro channel flow boiling." *International Communications in Heat and Mass Transfer* **80**:10-17.

Liu, Q. and Palm, B. (submitted to *International Communications in Heat and Mass Transfer*). "On the dynamics and heat transfer of flow boiling bubble chain in micro-channels."

Conference papers

Liu, Q. and Palm, B. (2014). "A numerical study of bubbles growing during flow boiling in micro-channel." *4th Micro and Nano Flow Conference. London, UK.*

Liu, Q. Anglart, H. and Palm, B. (2012). "A numerical study of bubbles growing during flow boiling in micro-channel." *Asme 2012 10th International Conference on Nanochannels, Microchannels, and Minichannels. Rio Grande, Puerto Rico, USA*

Acknowledgement

First and foremost, I would like to thank my supervisor Prof Björn Palm, for giving me the opportunity to come to beautiful Stockholm and study in this wonderful school (KTH). Throughout my six and half year study here, he has always been a mentor.

I also appreciate the help from co-supervisor associate Professor Joachim Claesson, and co-author Profssor Henryk Anglart and Dr Wujun Wang who is not only a colleague but also a friend.

I am grateful that emeritus Professor Eric Granryd, Professor Victoria Martin and Per Lundqvist, associate Professor Paul Petrie-Repar and Rahmat Khodabandeh, PhD students Monika Ignatowicz, Pavel Maknatch, and Patricia Monzo have offered insightful comments throughout my research seminars. To other lovely colleagues in the department, I feel lucky that I have been working with you.

To my dear friends in Stockholm, I truly appreciate your friendship which has accompanied me going through Nordic winters.

Last but not the least, I want to thank my parents and my wife, without whom this thesis would have not been possible.

1 Introduction

Despite economic fluctuations, world energy demands keep increasing. As a study shows (bp, 2016), world energy consumption will increase by 34% between 2014 and 2035, or by about 1.5-2% per year (Fig. 1.1). In certain application areas, such as electronic device cooling in the information and communication industry, and battery cooling in electric cars, energy usage is growing at a much faster pace. In a typical data center, roughly 33% of the total electricity is allocated for thermal management (Kheirabadi & Groulx, 2016). As is shown in Fig. 1.2, total global electricity usage in data centers has increased from approximately 152 billion kW h/year in 2005 to 238 billion kW h/year in 2010; roughly 1.3% of global electricity use (Garimella, Persoons, Weibel, & Yeh, 2013). The electric car market is growing even faster. Nowadays, most data centers apply air cooling and electric car batteries are cooled by liquid. These technologies are economical, and are easy to construct and maintain, but are not energy efficient.

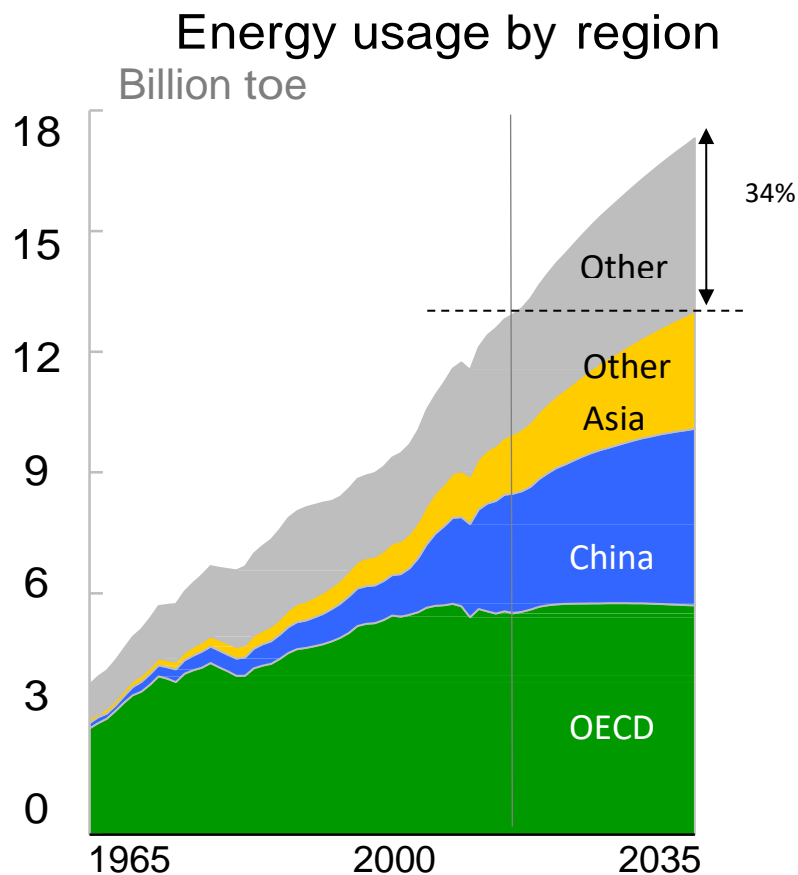


Fig. 1.1 World energy outlook (bp, 2016)

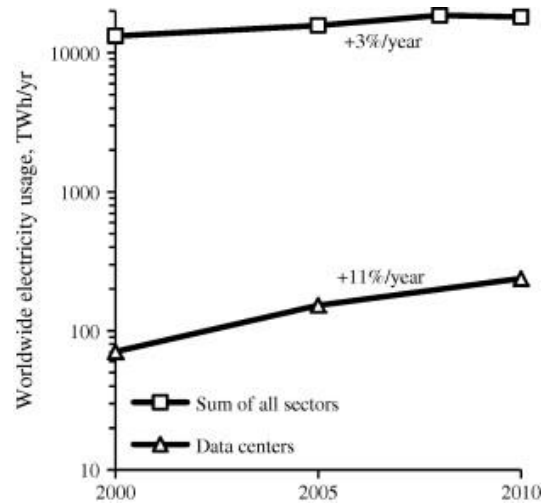


Figure 1.2

Worldwide electricity usage from 2000 until 2010: contribution of data centers (Δ) compared to the sum of all sectors. (Garimella et al., 2013)

On the other hand, the cooling density of these devices is increasing rapidly. For example: mobile communication network upgrades from 3G to 4G in less than a decade, and data exchange by mobile devices growing more than tenfold. Heat generated by an electronic chip can be as high as 300 W/cm^2 , which is much higher than that of air cooling capacity – usually 10 W/cm^2 (Macro Magnini, 2012).

To cool high heat flux devices and achieve high energy efficiency at the same time, micro channel boiling is becoming an inevitable and promising choice. This is largely attributable to micro channels' high surface-to-volume ratio as well as boiling's high heat transfer rate. Latent heat transferred during the boiling process is usually far greater than that in convection. Another factor behind the heat transfer enhancement is the local turbulence induced by bubble generation or interactions during the first stage of boiling: nucleate. Unfortunately, the mechanism of these boiling phenomena – whether in macro or micro structures – is not fully understood. According to Hsu and Graham (Hsu & Graham, 1961), three mechanisms control the nucleate boiling process: bubble agitation, vapor-liquid exchange, and evaporation. However, how the nucleate occurs, and how multi nucleate sites interact, are still too complicated to study. Thus the heat transfer coefficient calculation, which is vital for design, still very much depends on empirical or semi-empirical correlations. Among these correlations, one of the most popular for pool boiling was proposed by Cooper (Cooper, 1984), who used some 6000 pool boiling data points from published sources related to more than 100 experiments. The heat transfer coefficient for flow boiling is, however, a little more difficult due to more boiling patterns than in pool boiling. There are two groups of method for estimating this: 1) calculating an average heat transfer coefficient for the whole flow boiling process; and 2) calculating the local heat transfer coefficient as a function of vapor quality. Both methods are based on the pool boiling heat transfer coefficient, although in different ways (Webb & Gupte, 1992): enhancement, superposition and asymptotic. The enhancement model calculates the convective boiling heat transfer coefficient as an enhanced single-phase heat transfer

coefficient. On the other hand, the superposition model assumes that the convective boiling is the sum of nucleate boiling and convective evaporation. The asymptotic model is similar to the superposition model but with power function added to both parts.

Using the asymptotic (or superposition) model to calculate local heat transfer coefficient is believed to have high accuracy in most cases. This has also proved to be true in micro scale tubes. The key to this calculation is the evolution flow patterns as the function of vapor quality. Experimental visualizations from literature have shown that there are five major flow patterns in micro/mini scale channels: nucleate, isolated bubbles, confined bubbly flow, elongated bubbly flow, and annular flow. Of these, annular flow is the longest in most cases. It usually presents 70% of the total length of a tube. These flow patterns have appearance and heat transfer mechanisms. Studies of every individual flow pattern have been reported in published literature (J. R. Thome et al., 2008). Nevertheless, a vital question still remain unclear: How do these flow patterns evolve from one to another? They are also believed to play an important role, but are rarely studied. Only few visualization results (Owhaib, 2009) have shown that the transition from nucleate to confined bubbly flow seems more chaotic than that from elongate bubbles to annular flow. As far as the author is aware, no research on them has been reported and the mechanism is still mysterious, which is mostly due to both the small scale and extremely short time (less than a few milliseconds).

The objective of this thesis is to perform a comprehensive numerical study of these transition processes. The choice of numerical tools over experimental means is due to the fact that computational fluid dynamics (CFD) methods have the capability to investigate problems (especially in micro/mini scale) in a more detailed and accurate way, i.e. to measure the temperature, velocity or pressure inside vapor bubbles or the inner wall. In order to achieve this, the author has implemented a new numerical algorithm by combining two existing methods, and validated it against classic theory or published experiment data. By using the new method, the mechanism of these transition processes inside micro channel flow boiling is investigated.

2 State of the art

2.1 Boiling phenomena

Boiling has been a subject of interest for research since the early 20th century due to its wide industrial applications such as power plants, oil refineries, and refrigeration. Theoretical analysis of the phenomena, however, has developed much more slowly because of its complexity.

Rohsenow (Rohsenow, 1951) proposed one of the earliest nucleate boiling correlations, based on the bubble agitation mechanism. One of the most widely used pool boiling heat transfer coefficients is correlated by Cooper (Cooper, 1984), where some 6000 pool boiling data points from published resources, relating to over 100 experiments, were used. The correlation is based on reduced pressure:

$$h_{pool} = 55P^{0.12-0.2\log\epsilon} (-\log P_R)^{-0.55} M^{-0.5} q^{0.67} \quad (1)$$

Where M is the molecular weight, q is the heat flux, p is the reduced pressure and ϵ is the surface roughness.

The first generalization of flow boiling heat transfer coefficients was proposed by Chen (J. C. Chen, 1966). This was based on the idea that flow boiling can be seen as a combination of nucleate boiling and forced convection boiling. A more sophisticated form of this correlation is defined by the equation

$$h_{fb} = h_{nb}^m + h_{cb}^n \quad (2)$$

Where h_{nb} and h_{cb} are the nucleate boiling and forced convection heat transfer coefficient respectively. Exponents m and n are larger than 1. Similar correlations have been proposed ever since (Gungor & Winterton, 1986; Satish G Kandlikar, 1990; Shah, 1982).

These correlations have been supported by experimental visualizations (T. Chen & Garimella, 2006; Owlaib, 2009; Tibirica & Ribatski, 2014). It has been found that there are different flow patterns in flow boiling. Among them, the major five are bubbly flow, slug flow, annular flow, annular flow with entrainment, and dry-out region. The heat transfer mechanism of the bubbly flow regime is believed to be nucleate boiling dominant and the rest are more forced convection dominant.

As Fig. 2.1 shows, recent experimental studies (Ali, Palm, & Maqbool, 2011; Anwar, Palm, & Khodabandeh, 2015; Maqbool, 2012; Wu, Marcinichen, & Thome, 2013) have proved that flow boiling in micro channels has similar flow regimes, but also has two additional flow regimes: confined bubbly and slug flow (Fig. 2). The heat transfer mechanism is also believed to be flow pattern based. A phenomenological model (J. R. Thome, Dupont, & Jacobi, 2004) has been proposed for estimating heat transfer coefficient. Kandlikar (Satish G. Kandlikar, 2010b) has analyzed the similarities and differences between micro and macro channels.

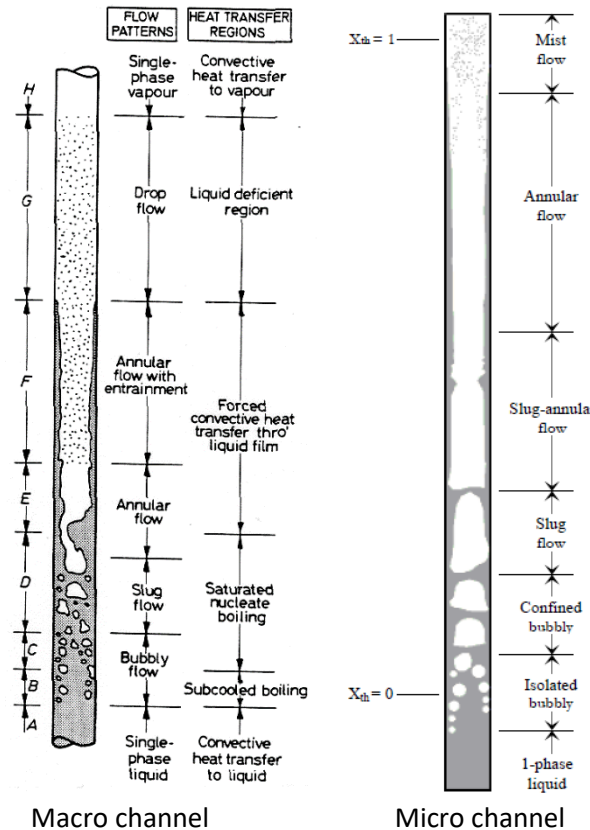


Figure 2.1 Flow patterns (J R. Thome & Collier, 1994)

It has been found that the differences are produced by the change of relative magnitude of the five forces exerted on the two-phase flow, namely: inertia, surface tension, shear, gravity, and evaporation momentum force. As the scale decreases, surface tension and shear force increase, gravity decreases, and inertia and evaporating momentum are unaffected. It is shown in Fig. 2.2 that the surface tension is the dominant force in micro channels (diameter $< 1\text{e-}3\text{m}$).

Since the whole process of flow boiling is very complex and each of its flow patterns has different characteristics, it is natural for researchers to focus on one flow regime at a time. The upstream flow pattern (bubbly flow) has been studied extensively. For instance, vapor bubbles' departure in forced convection boiling has been studied (Klausner, Mei, Bernhard, & Zeng, 1993). It was found that a vapor bubble typically slides along the heating wall after it departs from the wall. Van Helden, Van der Geld, and Boot (1995) performed an experiment on the bubble detachment from an artificial cavity in a plane wall of a vertical rectangular channel. Their experiments show a difference in takeoff direction between vapor and nitrogen bubble. Steam bubbles take off into the liquid, while nitrogen bubbles more or less slide parallel to the wall. Okawa, Ishida, Kataoka, and Mori (2005) conducted a visual study to elucidate the rise characteristics of vapor bubbles after the departure from a nucleation site in forced convective boiling. They also observed that bubbles slide up along the vertical wall before they depart. Van der Geld (2009) summarized prediction methods for the motion and deformation of a bubble that is created by

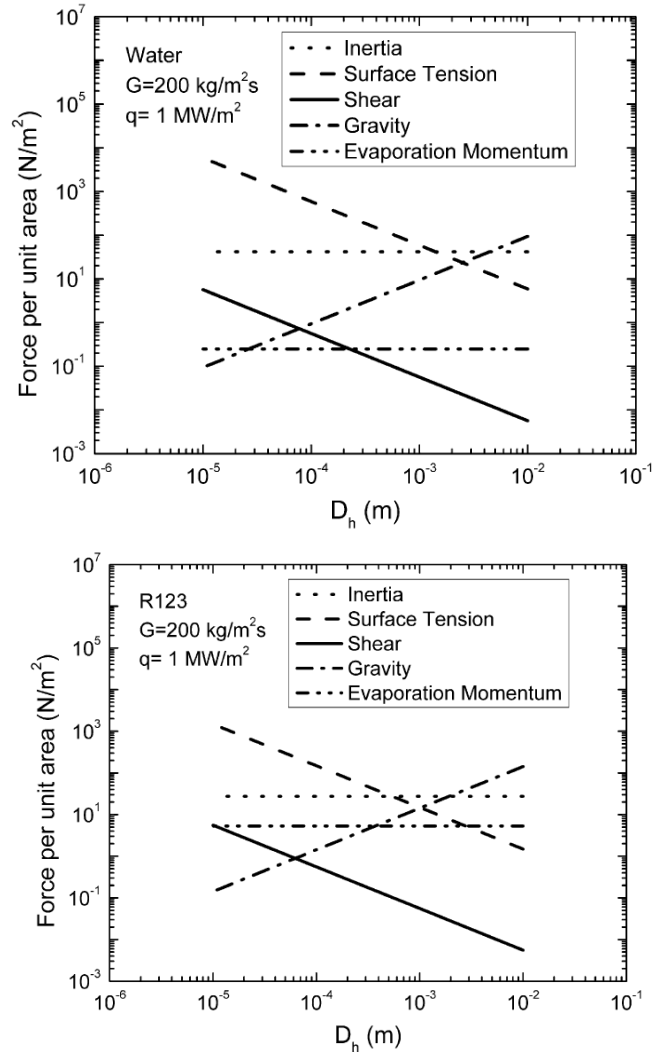


Figure 2.2 a) Scale effect of tube diameter on various forces during flow boiling of water, $G=50 \text{ kg/m}^2\text{s}$, $q=1 \text{ MW/m}^2$; b) Scale effect of tube diameter on various forces during flow boiling of R123, $G=200 \text{ kg/m}^2\text{s}$, $q=1 \text{ MW/m}^2$ (Satish G. Kandlikar, 2010a).

boiling at a wall, at times before and after detachment, with a focus on added mass forces in the vicinity of the wall. They found that the possibility to apply added mass coefficients derived in potential flows was also valid for flows with vorticity.

The confined bubbly flow is larger, which make it is relatively easy to visualize. Kenning, Wen, Das, and Wilson (2006) investigated a bubble growth in a capillary tube closed at one end and vented to the atmosphere at the other. The tube was initially filled with uniformly superheated water. They measured the rate of axial growth and the varying pressure at the closed end. They then used them to test and develop one-dimensional models for bubble growth applicable to the more complex conditions of confined-bubble flow boiling in micro channels. Issues included the thickness of the liquid films around confined bubbles and changes in saturation temperature due to the changes in pressure generated by bubble motion. Barber, Brutin, Sefiane, and Tadrist (2010) conducted a detailed imaging and analysis of the two-phase flow in a single microchannel geometry (hydraulic diameter 0.727 mm), using a refrigerant FC-72, to investigate the effect of

channel confinement on bubble growth. They observed periodic pressure fluctuations across the microchannel which is caused by the bubble dynamics and instances of vapor blockage during confined bubble growth in the channel. Very recently, Tibirica and Ribatski (2014) investigated the fundamental characteristics of bubble departure during flow boiling in microscale channels. They found that bubbles can depart from the wall with a diameter much smaller than the channel's diameter.

Adiabatic models for the prediction of bubble velocity in a two-phase flow without phase change have been developed (Bretherton, 1961; Taylor, 1961). According to these models, both the bubble terminal velocity and the film thickness are a sole function of capillary number. When boiling is involved, however, the dynamics of the bubbles becomes complicated. Evaporating film is found to accelerate bubbles (Han & Shikazono, 2010), and the increase in film thickness is restricted by the bubble acceleration. They proposed a new correlation to predicate the film thickness by including Bond number. Agostini, Revellin, and Thome (2008) investigated R134a elongated bubble velocities in micro channels. They found that bubble velocities increase with increasing bubble length and also increase with increasing channel diameter. Instantaneous heat transfer rate around consecutive Taylor bubbles has been studied in a relatively large channel (Fershtman, Shemer, & Barnea, 2016).

Annular flow represents 80% of channel length in most cases. Qu and Mudawar (2003) measured the saturated flow boiling heat transfer coefficient in water-cooled micro channels. They developed an annular flow model that included droplet entrainment and captured the unique overall trend of decreasing heat transfer coefficient with increasing vapor quality in the low vapor quality region. The droplet entrainment is difficult to calculate, thus a model to predicate it was proposed (Cioncolini, Thome, & Lombardi, 2009). Their model is based on the core flow Weber number that is a controlling dimensionless group in determining the wall shear stress and associated frictional pressure gradient of annular flows. Han, Kanno, Ahn, and Shikazono (2015) measured the thickness of this film and found that a flat interface model overestimates it. They developed a new empirical correlation considering the effect of the non-flat gas-liquid interface, which showed good agreement with experiment data.

Literature on the study of multi bubbles and interactions between bubbles during flow boiling is limited. However, similar phenomena without heat transfer have already been observed (Batchelor & Green, 1972). Bhaga and Weber (1980) conducted a visualization of two bubbles rising in line in liquid and calculated their Reynolds number. It was found that the Reynolds number of the trailing bubble increases during the rising process, while that of the leading one remains constant. The interaction of two bubbles rising side by side has been studied (Legendre, Magnaudet, & Mougin, 2003).

Bubbles' interaction and coalescence in boiling phenomena is more complicated. Zhang and Shoji (2003) studied the physical mechanism of nucleate site interaction in pool boiling. Their research revealed that there is not only hydrodynamic interaction, but also thermal interaction which together lead to bubble coalescence. The bubble separation distance affects bubble

coalescence and the bubbling-cycle duration decreases with a decreasing separation distance (T. Chen & Chung, 2003). Golobic, Petkovsek, and Kenning (2012) investigated bubble growth and horizontal coalescence in saturated pool boiling on titanium foil, using high-speed IR thermography. The interaction between bubbles before coalescence was found to be asymmetrical. During coalescence, the movement of liquid under both bubbles caused changes in the wall heat flux that also depended on pre-cooling. Siedel, Cioulachtjian, and Bonjour (2008) presented experimental results of pentane pool boiling on two adjacent nucleation sites. Bubbles' growth has been recorded using a high-speed camera under various wall superheat conditions. Oscillations were observed during growth, showing the interaction of one bubble with the preceding bubble released from the same nucleation site. Lateral coalescence has been visualized and the images have brought to the fore the capillary effects on the distortion of the interface.

In addition to the interaction and coalescence in pool boiling and nucleate boiling, bubbles also coalesce in flow boiling. A one-dimension heat transfer model for evaporation of coalescing bubbles in micro channels has been proposed (Consolini & Thome, 2010). It assumes that heat transfer occurs only by conduction through the thin liquid film trapped between the bubbles and the wall.

2.2 Computational fluid dynamics modeling of boiling

Thanks to the advancements in both computing hardware and algorithms, computational fluid dynamics (CFD) has become a popular tool in boiling study. There are several advantages of CFD over experimental and modeling studies. One is that it can examine flow phenomena at very small scales and in very short times. Two of the major challenges in CFD study of boiling phenomena are interface reconstruction and interface temperature calculation.

Regarding interface reconstruction, two popular tools are available: the volume of fluid (VOF) and level set methods. Both have merits and drawbacks. With the volume of fluid method, the volume fraction function is not continuous at the interface, thus estimation can become very inaccurate when the interface is severely deformed. In macro scale simulation, the effect of surface tension force is not significant and the surface is not severe distorted. However, as mentioned in the previous section, the surface tension becomes the dominant force when the channel diameter is smaller than a few millimeters. At this scale, the interface curvature is large enough to produce "spurious velocities" around it. A large number of publications have been published to overcome this problem by developing new algorithms on the body force calculation.

Renardy and Renardy (2002) proposed a parabolic reconstruction of surface tension for the VOF method. They used a quadratic representation of the interface instead of a linear reconstruction. Their results show that the "spurious velocities" have been reduced.

Lörstad and Fuchs (2004) improved the VOF method by replacing the common first-order surface tension model with a second-order model. They introduced a distance function based on volume fraction to reconstruct the interface.

Francois et al. (2006) developed a pressure-correction VOF method. Within the algorithm they devised a continuum and a sharp interface representation. They found that the sharp surface tension method yields an abrupt pressure jump across the interface, whereas the continuous surface tension method results in a smoother transition. Both methods, however, yield spurious velocities of the same order, the origin of which is due solely to errors in curvature.

M. Sussman, Fatemi, Smereka, and Osher (1998) developed a constrained algorithm to reduce the mass error from 3% to 1%.

Olsson and Kreiss (2005) proposed a conservative level set method by adding an intermediate step after the standard advection. This step can ensure the smoothness of the level set function profile and the interface thickness is preserved.

Considering the complementary advantages and disadvantages of the level set and VOF methods, it is natural to develop a coupled method.

Mark Sussman and Puckett (2000) used the VOF method to improve the mass conservation of the level method. In their algorithm, both the level set and the VOF are solved. The interface curvature is estimated by level set and the intercept of interface line is corrected by the VOF to ensure mass conservation. The volume fraction field is then “truncated” by the level set function, i.e. it removes spurious volumes (“flotsam”), generally created by rounding off errors, that exist more than one grid cell length from the zero level set. Later on they developed a second order algorithm based on the original one by calculating the interface curvature from the volume fraction instead of the level set function (Mark Sussman, 2003).

Subsequently, improved CLSVOF (G. Son & Hur, 2002), Mass Conserved LS (van der Pijl, Segal, Vuik, & Wesseling, 2005) and Adaptive CLSVOF (Yang, James, Lowengrub, Zheng, & Cristini, 2006) methods were put forward. Just as with the original CLSVOF by Sussman, all of these methods need to solve both the level set and the volume fraction advection equations.

D. L. Sun and Tao (2010) developed a simpler coupled method where only the volume fraction equation is solved and the level set function is calculated using a simple iterative geometric operation. Since their model uses the VOF to capture the interface, an exact mass conservation is obtained.

In addition to coupled methods, other efforts have also been made to improve mass conservation. For example, Nourgaliev, Wiri, Dinh, and Theofanous (2005) have shown that reducing the spatial discretization errors in Eq. (13) can also improve mass conservation.

G. Son, Dhir, and Ramanujapu (1999) used a level set function to study a growing and departing bubble on a horizontal surface. They used a finite difference scheme to solve the governing equations and considered the effect of micro layer evaporation. Later on, they (G. Son, Ramanujapu, & Dhir, 2002) investigated the growth, departure, and merging of bubbles on a single nucleate site. They found that the bubble diameter at departure is not influenced by the bubble merging pattern to any great degree.

Welch and Rachidi (2002) presented a study of film boiling with a prescribed heat flux including conjugate heat transfer. They used a VOF algorithm and found that the solid wall acts as a heat sink or source that attenuates the temperature fluctuations on the solid boundary.

Li and Dhir (2007) applied the same method to study single bubble dynamics during flow boiling. They also took into account the effect of micro-layer evaporation. The bubble liftoff diameter was found to decrease with bulk flow velocity, but increases when the component of gravity normal to the heater surface is decreased. The pressure difference that develops between lower and upper parts of the bubble during the sliding motion helps the bubble liftoff from the surface for the vertical up-flow boiling case and reduced gravity conditions.

Mukherjee and Kandlikar (2005) studied a vapor bubble growing in superheated liquid inside a microchannel using the level set method. They found that the bubble initially grows at a constant rate, but its length increases rapidly when it fills the channel cross-section and expands in a longitudinal direction. This increase in growth rate is due to the thin layer of liquid between the walls and its interface, where a high rate of evaporation takes place.

Kunkelmann and Stephan (2010) implemented a volume of fluid solver of OpenFOAM. They included contact line evaporation.

Nichita, Zun, and Thome (2010) utilized a level set method coupled with the VOF method. They implemented it into the commercial CFD code FLUENT. The level set equation is solved by a weighted essentially non-oscillatory scheme. By doing this they reduced approximately 51% of spurious currents compared with the VOF method.

M. Magnini, Pulvirenti, and Thome (2013b) developed a height function algorithm to capture the gas-liquid interface. They used this to study an elongated bubble in a microchannel using of a phase change model proposed by Hardt and Wondra. According to their findings, the heat transfer coefficient increases monotonically as film thickness decreases. They (M. Magnini, Pulvirenti, & Thome, 2013a) also studied the influence of leading and sequential bubbles on slug flow in micro channels. The sequential bubble is found to grow at a slower rate than the leading one.

Ling, Son, Sun, and Tao (2015) investigated bubble growth and merging in micro channel flow boiling. They adopted a three-dimensional coupled VOF and level set method. Their results showed that the merging can produce a temporal growth in heat flux, while the thin liquid film between the bubble and the wall is the main reason for the high heat flux in microchannel boiling flow.

The Lattice Boltzmann method has emerged as an attractive approach due to its parallelize-friendly nature. T. Sun, Li, and Yang (2013) used it to study bubble growth and departure during flow boiling. It has been found that the bubble departure diameter and the release frequency are proportional to gravitation in quiescent fluid. Gong and Cheng (2013) investigated

continuous and periodic bubble nucleation, growth, and departure from a heated surface in pool boiling.

which has a better estimation on the interface, is not naturally mass conserved, and loses mass during calculations. Concerning the phase change, the use of an equilibrium model is easy to implement but leads to poor interface temperature estimation, especially when the interface curvature is high. This is because an increasing interface curvature will increase interface pressure, which further increases saturated temperature, thus violating the constant saturated temperature assumption. Until very recently, these two challenges have been addressed using the coupled level set method (CLSVOF) and the non-equilibrium model respectively. The CLSVOF model was developed by Mark Sussman & Puckett (2000). They used the level set method to calculate interface curvature and the VOF method to constrain mass, thus combining the merits of these two methods while overcoming their disadvantages. The non-equilibrium model (Hardt & Wondra, 2008) dynamically calculates the interface temperature during every time step. This is different to the equilibrium model, where it is a constant.

3 Numerical framework

Advances in computer science have facilitated computational fluid dynamics (CFD) in recent decades. Compared to experimental studies, the advantages of CFD are based on the small scale and short time span of micro channel flow boiling. Before the widespread use of CFD, experimental tools experienced difficulties measuring temperatures and pressure at such a small scale. However, the less chaotic two-phase flow in mini/micro channels has made it simpler to model using CFD than in larger channels.

As with other fluid dynamic phenomena, flow boiling is governed by the well-known Navier-Stokes equations as follows:

$$\frac{\partial \rho}{\partial t} + \nabla \cdot (\rho \mathbf{u}) = \dot{\rho} \quad (3)$$

$$\rho \left(\frac{\partial \mathbf{u}}{\partial t} + \mathbf{u} \cdot \nabla \mathbf{u} \right) = -\nabla P + \nabla (\mu (\nabla \cdot \mathbf{u} + \nabla \cdot \mathbf{u}^T)) + \rho g + \mathbf{F}_\sigma \quad (4)$$

$$\rho C_p \left(\frac{\partial T}{\partial t} + \mathbf{u} \cdot \nabla T \right) = \Phi + \nabla \cdot (k \nabla T) + H_e \quad (5)$$

These are the continuity equation (3), the momentum equation (4), and the energy equation (5). For multiphase simulation, an additional interface equation should be solved.

The difficulty of flow boiling CFD modeling in micro channels is primarily caused by two challenges: the interface tracking algorithm and the phase change model. Surface tension dominance flow makes interface tracking more difficult because interfacial curvature increases as channel dimension decreases. The surface tension force \mathbf{F}_σ at the interface is also difficult to calculate accurately. The energy source H_e caused by boiling in the energy equation will also become a problem when the interface cannot be reconstructed correctly. To overcome these two major problems, a non-equilibrium smeared phase change model is implemented alongside the coupled level set and VOF method via user-defined functions of the software ANSYS FLUENT 14.5.

3.1 Governing equations

The Navier-Stokes equations are non-linear partial differential equations (PDE) and cannot be solved analytically yet. For given general initial conditions, it is even not clear that smooth solutions always exist in three-dimensional space (Feireisl, Novotný, & Petzeltová, 2001). Therefore, discretization schemes are employed to transfer the non-linear PDEs to a matrix of linear equations. In other words, numerical solutions give answers at discrete points (grid points in geometry) instead of continuous and smooth space (Anderson & Wendt, 1995). Among these discretization schemes, the most commonly used are finite difference, finite volume and finite element method.

The idea of finite difference (FD) is straightforward. Taking velocity \mathbf{u} in a one-dimensional space as an example, if u_{i+1} denotes velocity at the $(i+1)$ th grid point, it can be expressed as Taylor series as

$$u_{i+1} = u_i + \left(\frac{\partial u}{\partial x} \right)_i \Delta x + \left(\frac{\partial^2 u}{\partial x^2} \right)_i \frac{(\Delta x)^2}{2} + \dots \quad (6)$$

Then

$$\left(\frac{\partial u}{\partial x}\right)_i = \frac{u_{i+1} - u_i}{\Delta x} + o(\Delta x) \quad (7)$$

This is called a forward scheme since it uses information at point $i+1$ and an analogy can be drawn for a backward scheme. The computational domain is usually divided into hexahedra grids, and the solution will be obtained at each grid node. It should be noted that both schemes have only first-order accuracy. In order to achieve second-order accuracy, information from both the $(i+1)$ th and the $(i-1)$ th grid point needs to be used.

$$\left(\frac{\partial u}{\partial x}\right)_i = \frac{u_{i+1} - u_{i-1}}{\Delta x} + o(\Delta x)^2 \quad (8)$$

Due to its simple implementation, finite difference was very popular in the early stage of CFD (1960-1980s), especially in non-phase-change problems. Since it solves the differential form of the N-S equations, a discontinuity (or a shock) of the dependent function would usually lead to divergence. Very fine mesh could help to reduce the problem, but at a high cost in terms of computational load.

The finite volume method (FVM), on the contrary, has better performance on shock problems. This is because it actually solves an integrated form (or weak form) of N-S equations, instead of solving the differential form. In this method the computational domain is divided into cells (finite volume) rather than nodes, and the dependent values (velocity, temperature, etc.) are stored in the cell centers. For instance, if u_i denotes velocity at the i th cell center, the steady continuity equation without source in one-dimensional space and be rewritten as:

$$\iiint_{i-1/2}^{i+1/2} \left(\frac{\partial u}{\partial x}\right)_i = 0 \quad (9)$$

, where $i-1/2$ and $i+1/2$ denote the faces of the cell.

By applying Gauss Theorem, this becomes

$$\iint_{i-1/2}^{i-1/2} u_{i-1/2} - \iint_{i+1/2}^{i+1/2} u_{i+1/2} = 0 \quad (10)$$

$u_{i-1/2}$ can be interpolated by neighborhood cell values depending on the interpolate scheme.

The basic advantage of the FVM over FD is that it does not require a structured grid. In addition, as mentioned above, any discontinuity of velocity u within $[i-1/2, i+1/2]$ will also disappear in this integrated form, thus making the numerical solution more stable.

The finite element method divides the computational domain into small sub-domains (finite elements), and solves the dependent variables in the nodes connecting these sub-domains. In this sense, it differs from the FVM where cell values are used. On the other hand, it also solves a weak form of the PDEs, i.e. a production of the integration form of the PDEs and a test function in each sub-domain.

$$\iiint_{i-1}^{i+1} f t_i \left(\frac{\partial u}{\partial x}\right)_i = 0 \quad (11)$$

, where f_t is the test function. When f_t is equal to 1 in every sub-domain, it is equal to the finite volume method. And when $\iiint_{i-1}^{i+1} f_t = 0$, it is the finite difference method. In other words, the dependent functions are represented by basis functions (generally polynomials) instead of simple interpolation as in the FVM and FD.

The FVM is generally more robust in fluid dynamics, and some of the most successful CFD software is based on it, e.g. ANSYS FLUENT (commercial), ANSYS CFX (commercial), STAR CCM+ (commercial), and OpenFOAM (free). In this thesis, the FVM is used to solve the integrated form of governing equations as follows:

$$\int_V \frac{\partial \rho}{\partial t} dV + \oint_A \rho \mathbf{u} \cdot d\mathbf{A} = \int_V \dot{\rho} dV \quad (12)$$

$$\int_V \rho \frac{\partial \mathbf{u}}{\partial t} dV + \oint_A \rho \mathbf{u} \cdot \mathbf{u} d\mathbf{A} = \oint_V \rho \mu \nabla^2 \cdot \mathbf{u} dV + \int_V (-\nabla P + \rho \mathbf{g} + \mathbf{F}_\sigma) dV \quad (13)$$

$$\int_V \rho \frac{\partial C_p T}{\partial t} dV + \oint_A \rho \mathbf{u} T d\mathbf{A} = \oint_A \rho \Phi \nabla T d\mathbf{A} + \int_V H_e dV \quad (14)$$

, where V is the cell volume and A is the cell face vector.

3.2 Discretization schemes

3.2.1 Temporal discretization

For transient problems, the governing equations must be discretized in time. Taking the velocity, for example, a first order accurate temporal discretization is as follows:

$$\frac{\partial \mathbf{u}}{\partial t} = f(\mathbf{u}) \quad (15)$$

$$\frac{\mathbf{u}^{n+1} - \mathbf{u}^n}{\Delta t} = f(\mathbf{u}^n) \quad (16)$$

Where $n+1$ and n is the number of time steps and Δt is the time step. If higher order accuracy is needed, one can write the second order discretization as

$$\frac{3\mathbf{u}^{n+1} - 4\mathbf{u}^n + \mathbf{u}^{n-1}}{\Delta t} = f(\mathbf{u}^n) \quad (17)$$

The above schemes are explicit since the variable in the right hand side of the equation is the previous time step. In order to achieve higher accuracy and stability, an implicit scheme is usually applied, although more computational loads are needed. This has the following form:

$$\frac{\mathbf{u}^{n+1} - \mathbf{u}^n}{\Delta t} = f(\mathbf{u}^{n+1}) \quad (18)$$

3.2.2 Spatial discretization

As is shown in equations (12), (13), and (14), face values need to be calculated. The interpolate schemes need to be carefully addressed according to different boundary and operating conditions.

Second order upwind

The second order upwind scheme is straightforward. The philosophy is to estimate the face value from its upstream cell volume. Let “i” be the cell number, “i+1/2” “i-1/2” are the face of this cell, and the flow direction is from “i-1/2” to “i+1/2”. Then the velocity at the outer surface “i+1/2” can be found using the equation

$$\mathbf{u}_{i+1/2} = \mathbf{u}_i \quad (19)$$

This is called first order upwind. Higher order accuracy can be achieved using the equation

$$\mathbf{u}_{i+1/2} = \mathbf{u}_i + \nabla \cdot \mathbf{u}_i \cdot \mathbf{r} \quad (20)$$

, where \mathbf{r} is the vector points from cell center to face.

QUICK scheme

In quadrilateral and hexahedral meshes, where unique upstream and downstream faces and cells can be identified (Ansys, 2011), the QUICK scheme is a promising discretization method due to its high-order accuracy. The name “QUICK” stands for quadratic upstream interpolation for convective kinematics. It uses three cell points to calculate the face value, where two of them are upstream. Take velocity at cell “i”, for example, which can be found using the following equation:

$$\mathbf{u}_{i+1/2} = c \left(\frac{\Delta x_i}{\Delta x_i + \Delta x_{i-1}} \mathbf{u}_{i-1} + \frac{\Delta x_{i-1}}{\Delta x_i + \Delta x_{i-1}} \mathbf{u}_i \right) + (1 - c) \left(\frac{\Delta x_{i-2}}{\Delta x_{i-2} + \Delta x_{i-1}} \mathbf{u}_{i-1} - \frac{\Delta x_{i-1}}{\Delta x_{i-2} + \Delta x_{i-1}} \mathbf{u}_{i-2} \right) \quad (21)$$

, where c is a coefficient with a value between 0 and 1. QUICK scheme is used for the phase change equation in this paper.

MUSCL scheme

The monotonic upstream-centered scheme for conservative laws (MUSCL) can provide a high order of accuracy for partial differential equations, especially when shocks exist. A third order of the MUSCL scheme can be calculated from the following equation:

$$\mathbf{u}_{i+1/2} = c * \mathbf{u}_{i+1/2,cd} + (1 - c) \mathbf{u}_{i+1/2,sou} \quad (22)$$

, where $\mathbf{u}_{i+1/2,cd}$ is the central difference scheme and can be calculated using the equation

$$\mathbf{u}_{i+1/2,cd} = \frac{\mathbf{u}_i + \mathbf{u}_{i+1}}{2} + \frac{(\nabla \cdot \mathbf{u}_i \cdot \mathbf{r}_i + \nabla \cdot \mathbf{u}_i \cdot \mathbf{r}_i)}{2} \quad (23)$$

, and $\mathbf{u}_{i+1/2,sou}$ is defined in the second order upwind scheme. One of the main advantages of the MUSCL scheme is the ability to overcome shock problems at the interface of two-phase simulations. This scheme is used for convection term in the continuity equation, the momentum equation and the energy equation.

Gradient scheme

The diffusive terms in the momentum (shear force) and energy (conduction) still have gradient after the integration over the finite volume. As usual, take velocity at cell “i” for example, which can be calculated by applying the Gauss theorem.

$$\nabla \cdot \mathbf{u}_i = \frac{\oint_A \mathbf{u}_{i,f}}{V} = \frac{\oint_{i+1/2} \mathbf{u}_{i+1/2} + \oint_{i-1/2} \mathbf{u}_{i-1/2}}{\Delta x_i} \quad (24)$$

Face values $\mathbf{u}_{i-1/2}$ and $\mathbf{u}_{i+1/2}$ can be calculated from either cell values or node values. Usually, node-based estimation has higher accuracy, albeit at the expense of time and computational load. This is primarily because a finite volume usually has more nodes (at least two) than cells (one). In this study, all gradients are computed using node-based evaluation.

3.3 Pressure-velocity coupling

The pressure term in the momentum equation needs a special iterate algorithm to couple with the velocity field.

3.3.1 SIMPLE algorithm

One of the most common algorithms is the semi-implicit method for pressure linked equations (SIMPLE). The principle of this algorithm is to use a divergence-free velocity field to correct momentum equation. If we consider potential flow, given a guessed pressure p^* , then velocity field \mathbf{u}^* can be solved using the momentum equation (surface tension is neglected) as:

$$\frac{\mathbf{u}^* - \mathbf{u}^n}{\Delta t} + \mathbf{u}^*(\nabla \cdot \mathbf{u}^*) + \mu \nabla^2 \cdot \mathbf{u}^* = \nabla p^* \quad (25)$$

, where \mathbf{u} and p denote velocity and pressure function respectively. The guessed velocity field may not satisfy the continuity equation and needs to be corrected. The exact solution \mathbf{u}^{n+1} can be obtained by adding a correction term \mathbf{u}' :

$$\mathbf{u}^{n+1} = \mathbf{u}^* + \mathbf{u}' \quad (26)$$

$$\nabla \cdot \mathbf{u}^{n+1} = 0 = \nabla \cdot \mathbf{u}^* + \nabla \cdot \mathbf{u}' \quad (27)$$

The analogy for pressure is

$$p^{n+1} = p^* + p' \quad (28)$$

$$\nabla p^{n+1} = \nabla p^* + \nabla p' \quad (29)$$

Substituting them together with the continuity equation with the momentum equation, for incompressible flow ($\nabla \cdot \mathbf{u}^{n+1} = 0$), we get the following equation:

$$\frac{\mathbf{u}^{n+1} - \mathbf{u}^n}{\Delta t} + \mathbf{u}^{n+1}(\nabla \cdot \mathbf{u}^{n+1}) + \mu \nabla^2 \cdot \mathbf{u}^{n+1} = \nabla p^{n+1} \quad (60)$$

Subtracting the guess momentum equation we get

$$\frac{\mathbf{u}^{n+1} - \mathbf{u}^*}{\Delta t} + [\mathbf{u}^{n+1}(\nabla \cdot \mathbf{u}^{n+1}) - \mathbf{u}^*(\nabla \cdot \mathbf{u}^*)] + \mu \nabla^2 \cdot \mathbf{u}^* = \nabla p' \quad (71)$$

$$\nabla \cdot \mathbf{u}^{n+1} = 0 \quad (82)$$

This yields

$$\frac{\mathbf{u}^{n+1} - \mathbf{u}^*}{\Delta t} - \mathbf{u}^*(\nabla \cdot \mathbf{u}^*) + \mu \nabla^2 \cdot \mathbf{u}^* = \nabla p' \quad (93)$$

Take divergence

$$\frac{-\nabla \cdot \mathbf{u}^*}{\Delta t} + \nabla \cdot (\mathbf{u}^* \nabla \cdot \mathbf{u}^*) + \mu \nabla^3 \cdot \mathbf{u}^* = \nabla^2 p' \quad (104)$$

This is the so-called pressure correction equation. By solving this equation we get pressure correction p' . Substituting it with equation (33) we get corrected velocity \mathbf{u}' and updated velocity \mathbf{u}^{n+1} respectively. The solution may not converge at this time. In this case, more iteration is needed to get an accurate solution.

Note that this algorithm has used velocity divergence to correct pressure and velocity fields. Hence, it is only valid for incompressible flow. For compressible flow, special treatment is needed. The discretized momentum equation and pressure correction equation are solved implicitly, and the velocity correction equation is solved explicitly. This is why the algorithm is called “semi-implicit”.

3.3.2 PISO algorithm

Although the SIMPLE algorithm is generally more accurate than explicit methods, its iteration process makes time-dependent calculations rather expensive. In light of this, a non-iterative variation called pressure implicit with splitting of operator (PISO) was proposed by Issa (1986) to overcome this disadvantage. This utilizes the splitting of operators in the discretization of momentum and pressure equations so that the fields obtained with each time step are close approximations of the exact solutions. Unlike the SIMPLE method, where only one corrector step is used, the PISO method usually uses two or three corrector steps for velocity and pressure fields to obtain higher accuracy. The order of accuracy depends not only on the number of corrector steps but also on the time steps, thus a small time step (corresponding courant number <1) is generally preferred for the PISO scheme. Compared to iterative methods such as SIMPLE, PISO and other non-iterative methods are faster, and are therefore more suitable for transient flow. In this paper, all transient calculations are performed using the PISO scheme on pressure and velocity coupling.

3.4 Interface capturing methods

Interface reconstruction has been a major challenge in multiphase simulations. In general, it can be divided to two major groups: interface capturing and interface tracking. While the interface tracking schemes -including the front tracking (Tryggvason et al., 2001) and Lagrangian

methods- usually track the interface explicitly, the interface capturing methods – including level set and volume of fluid – implicitly capture the interface. As shown in Fig.3.1, in interface tracking methods, the mesh usually changes while the mesh in interface capturing methods usually remains structured. Due to its simplicity on implementation, especially for three-dimensional cases, the interface capturing methods have been developed and utilized in this thesis.

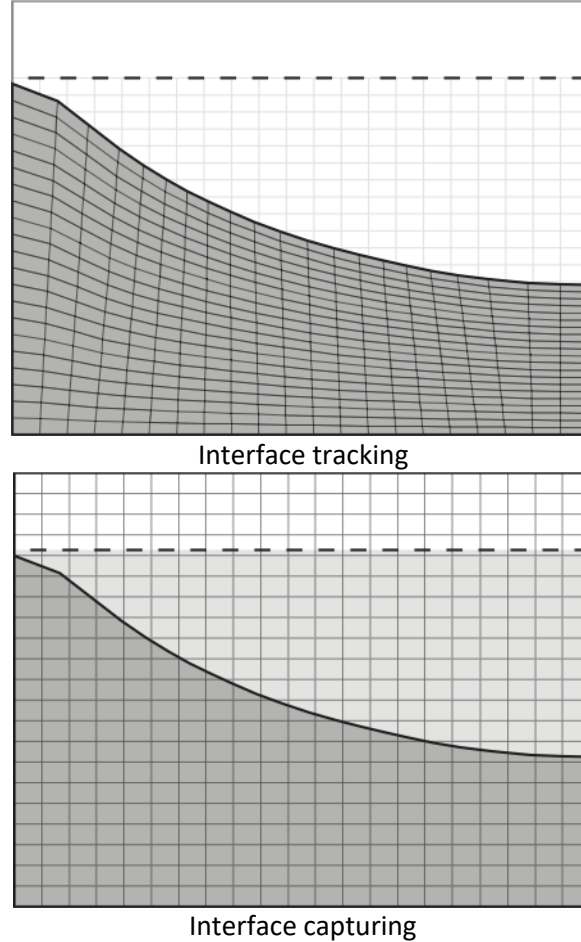


Figure 3.1 Two interface reconstruction methods

3.4.1 Volume of Fluid method

The Volume of Fluid (VOF) method (Hirt & Nichols, 81) is one of the most popular interface capturing methods. It is a one fluid method, where the two phases are actually treated as single phases with variant properties. This reduces computational load because only one set of Navier-Stocks equations and a volume fraction advection equation (equation 6) need to be solved. In addition, a volume fraction equation should be solved (equation 35).

$$\frac{\partial \alpha}{\partial t} + \nabla \cdot (\alpha \mathbf{u}) = -\frac{\dot{\rho}}{\rho_v} \quad (35)$$

All the physical properties, such as density, viscosity and thermal conductivity, are the average values of all the phases in the cell and have the following form:

$$\Phi = \sum_1^n \Phi_i \alpha_i \quad (36)$$

, where α_i is the volume fraction of the phase i in each computational cell. Taking two-phase flow as an example, the subscript i can be omitted and the value of the primary phase can be assigned as in equation (37).

$$\alpha(x, t) = \begin{cases} 1 & \text{if } x \in \text{primary phase} \\ (0,1) & \text{if } x \in \text{interface } \Gamma \\ 0 & \text{if } x \in \text{secondary phase} \end{cases} \quad (37)$$

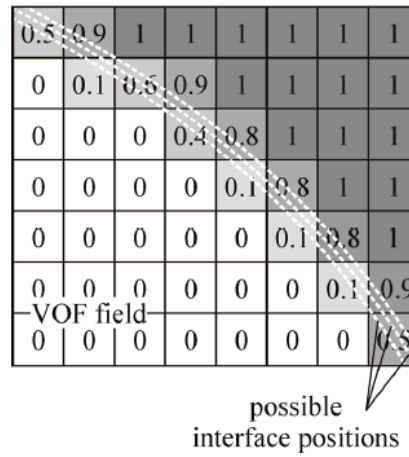


Figure 3.2 The VOF method

The principle of the VOF method is shown by Fig. 3.2. The interface usually spreads across two or three cells, which implies that the VOF method is not a tracking method but merely a capture method because it only gives the interface position but not the direction. Reconstruction of the interface normal vector needs extra effort. Youngs (1982) developed a piecewise linear interface calculation (PLIC) method based on the idea that the interface can be represented by a line in two dimensions or a plane in three dimensions. The vector normal to the interface can be calculated using the equation

$$\mathbf{n} = \frac{\nabla \alpha}{|\nabla \alpha|} \quad (38)$$

After the interface has been reconstructed, the surface tension force in the momentum equation () can be calculated as (Brackbill, Kothe, & Zemach, 1992):

$$\mathbf{F}_\sigma = -\sigma \mathbf{k} \nabla \alpha \quad (39)$$

, where \mathbf{k} is the curvature calculated using the equation

$$\mathbf{k} = \nabla \cdot \mathbf{n} = \nabla \cdot \frac{\nabla \alpha}{|\nabla \alpha|} \quad (40)$$

3.4.2 The level set method

Unlike the VOF method, the level set method (Osher, 1993; Mark Sussman, Smereka, & Osher, 1994) is by nature continuous. The idea of the level set is simple: a given interface is represented by a zero level set function, and each phase is represented by either a positive or a negative level set function.

In other words, the level set function is a signed distance function to the interface as follows:

$$\phi(x, t) = \begin{cases} +|d| & \text{if } x \in \text{primary phase} \\ 0 & \text{if } x \in \text{interface } \Gamma \\ -|d| & \text{if } x \in \text{secondary phase} \end{cases}, \quad (41)$$

Fig. 3.3 shows a two-dimensional level set function sketch. The shortest distance is d in equation (41).

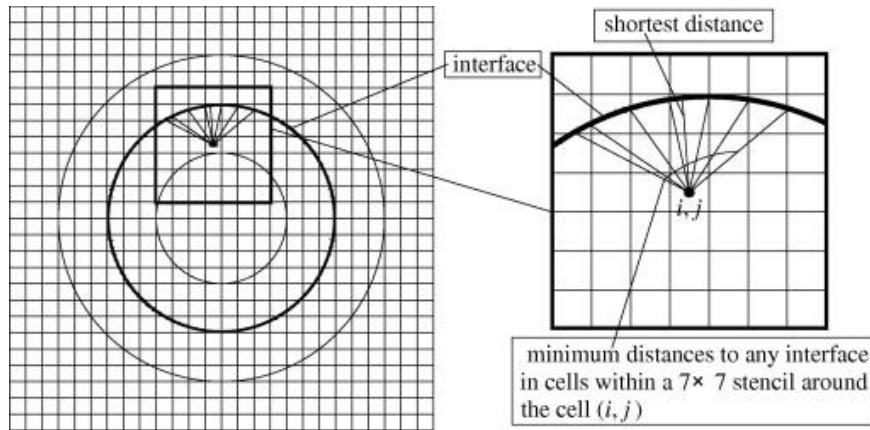


Fig.3.3 Sketch of the level set method (D. L. Sun & Tao, 2010)

The motion of the level set function is solved by the advection of the level set function ϕ with the velocity field. This elementary equation is:

$$\frac{\partial \phi}{\partial t} + \nabla \cdot (\phi \mathbf{u}) = 0. \quad (42)$$

The level set function tends to lose its distance function characteristic ($|\nabla \phi| = 1$) after advection; thus it is necessary to reinitialize it as a signed distance function every time step. The reinitialized equation is:

$$\frac{\partial \phi}{\partial t} + \text{sign}(\phi) * (1 - |\nabla \phi|) = 0. \quad (43)$$

The reconstruction of the interface and the calculation of the surface tension are similar to that of the VOF method (i.e. the interface normal vector is solved using a level set gradient).

$$\mathbf{n} = \frac{\nabla\phi}{|\nabla\phi|} \quad (44)$$

$$\mathbf{k} = \nabla \cdot \frac{\nabla\phi}{|\nabla\phi|} . \quad (45)$$

It should be noted that when $|\nabla\phi| = 1$, the curvature calculation merely becomes a Laplacian operation. The reconstruction of the interface is not needed in the level set method, because the interface face is explicitly given by the zero level set function. Despite the simplicity of curvature estimation, there is more numerical error when using the advection equation (42). A common symptom is loss/gain of mass.

3.4.3 The coupled level set and VOF method

The advantages of the VOF method and the level set method are complementary, which makes it interesting from a research point of view to combine these two methods – i.e. to utilize the VOF method to locate the interface position and the level set method to calculate the interface normal vector. Mark Sussman & Puckett (2000) published the first coupled level set and VOF method in 2000. The algorithm can be summarized as the following steps:

- Solve the volume fraction equation.
- For all interface cells ($0 < \alpha < 1$), initialize the level set function as

$$\phi = 1 - 2\alpha$$
- Solve the reinitialized equation (14), and calculate the curvature using the level set function.
- Update the density by volume fraction, use the new curvature to calculate the surface tension force, and solve the transport equations.

3.5 Phase change modeling

Formulation of the interface phase change model is another challenge in diabatic multiphase simulation. The key point is how to estimate the interface temperature. Traditional simulation assumes that the interface temperature is equal to the saturate temperature. This approximation is generally valid and simple to implement. However, kinetic study has shown that the interface temperature deviates from the saturate temperature significantly when the evaporation is high. In micro channel boiling, this deviation cannot be neglected any longer. A more accurate but expensive alternative is the non-equilibrium phase change model, where the interface temperature is calculated rather than set as a constant. The heat flux across the interface (or heat jump) is then defined as the following equation:

$$q_e = \frac{T_{int} - T_{sat}}{R_{int}} , \quad (46)$$

where T_{int} is the interface temperature and R_{int} is the interfacial resistance defined by equation (47)

$$R_{int} = \frac{2 - C_e}{2C_e} \frac{\sqrt{2\pi R_{gas}} T_{sat}^{3/2}}{h_{lg}^2 \rho_v}, \quad (47)$$

where C_e is the evaporation (or accommodation) coefficient, R_{gas} is the gas constant, h_{lg} is the latent heat and T_{sat} is the saturated temperature.

3.6 Initial and boundary conditions

Three different sizes of micro channels are studied with corresponding phenomena. Boundary conditions such as wall heat flux and mass flux are also varied to ensure a more comprehensive study. All cases utilized constant heat flux conditions, which is an ideal approximation of micro-electronics cooling by neglecting wall conduction. Two refrigerants (r134a, r245fa) are chosen, as the former is widely used in industrial applications and the latter is the most likely alternative. The details of the simulations are listed in Table 3.1.

Table 3.1 Initial and boundary conditions for simulation cases

	Single bubble	Merging of bubbles	Slug to annular
Diameter mm	1.24	0.64	0.4
Length mm	5		
Heat flux kw/m ²	15-105	14/28	80/160
Mass flux kg/s	125-375	56/112	400
Refrigerant	R134a	R134a	R245fa
Saturation temperature K	305	300.15	304.15

3.7 Validations

The numerical models are validated by comparison to both analytical results and experiments. Specifically, the surface tension model is validated by both the lubrication theory and Shikazono's experiments, the coalescence model is validated by Bhaga's experimental visualization results, and the phase change model is validated by both the classic one-dimensional Stefan problem and an empirical correlation. All these validations have already been presented in our published papers (Liu & Palm, 2016; Liu, Wang, & Palm, 2017a) and are summarized in this section. Besides, flow transitions in each chapter of the thesis are also validated by individual experimental results from literature. The first is the study of R134a flow boiling in a microchannel with a diameter of 0.64mm (Ali, 2010) and the second is the study of r245fa boiling transition in a transparent microchannel with a diameter of 0.4mm (Tibirica & Ribatski, 2014). The sketch of Ali's experiment is shown in Fig. 3.4, while the work done by Tibirica and Ribatski is similar, and is thus not shown.

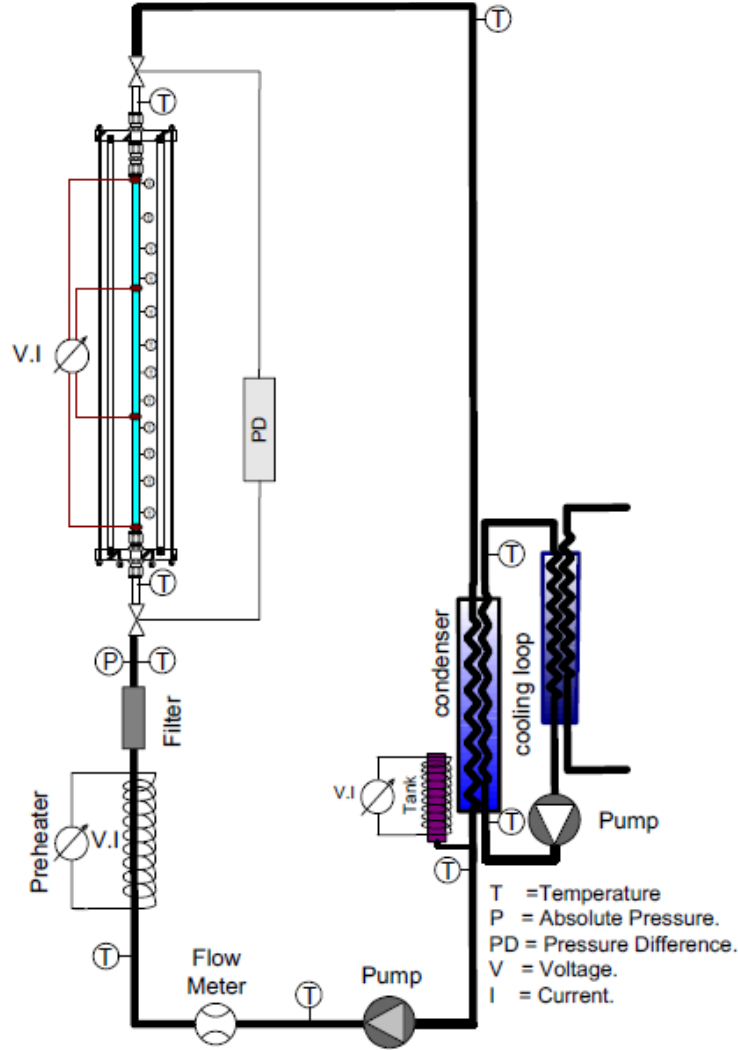


Fig. 3.4 Sketch of the validating experiment (Ali et al., 2011)

3.7.1 Validation of the coupled level set and VOF method

Bretherton (1961) has derived a theory on long bubbles (Taylor bubbles) moving in a viscous fluid. It reveals that the thickness of the thin film trapped between the wall and the bubble obey the lubrication approximation. In other words, it is a function of capillary number (Ca), which can be calculated from equation (49). Recently, a modified lubrication theory for micro/mini channels was proposed by including effects of Reynolds and Weber number (Han & Shikazono, 2009). The governing relations are summarized in equations 48, 49 and 50.

$$\frac{\delta}{D} = \frac{0.67Ca^{2/3}}{1 + 3.31Ca^{2/3} + 0.504Ca^{0.672}Re^{0.589} - 0.352We^{0.629}} \quad (48)$$

$$Ca = \frac{\mu * u_b}{\sigma} \quad (49)$$

$$We = Ca * Re, \quad (50)$$

where δ is the thin film thickness, Ca is the capillary number and We is the Weber number.

We validate the code by simulating an adiabatic R134a bubble moving in an axisymmetric mini channel with a diameter of 0.64mm. The initial film thickness between the bubble and the wall is 0.02mm. The initial bubble consists of a 1.28mm long cylinder and a hemispherical head, and both have a diameter of 0.6mm. The inlet velocity is 0.1m/s. As shown in Table 3.2, viscosity, surface tension and density are altered to get different capillary numbers while the Reynolds number is a constant. Simulations are run until the bubbles' terminal velocity reaches an equilibrium value which can be calculated using Taylor's law (Taylor, 1961)

$$\frac{u_b - u_f}{u_b} = C\sqrt{Ca} \quad (51)$$

, where u_f is the average fluid velocity.

Table 3.2 Simulation parameters for validation of CLSVOF

Operating parameters	Case 1	Case 2	Case 3	Case 4
Reynolds number	7,8	7,8	7,8	7,8
Capillary number	0,004	0,014	0,031	0,069

As illustrated in Fig. 3.5, the shapes of the bubbles at steady state are functions of the capillary number. The liquid film thickness increases with increasing capillary numbers and the rear end of the bubble is slightly upwards, which has been observed by an earlier experimental work (Aussilous & Quéré, 2000). The sketch is not a strictly 1:1 mimic of the bubbles, but with a compression of the x-axis.

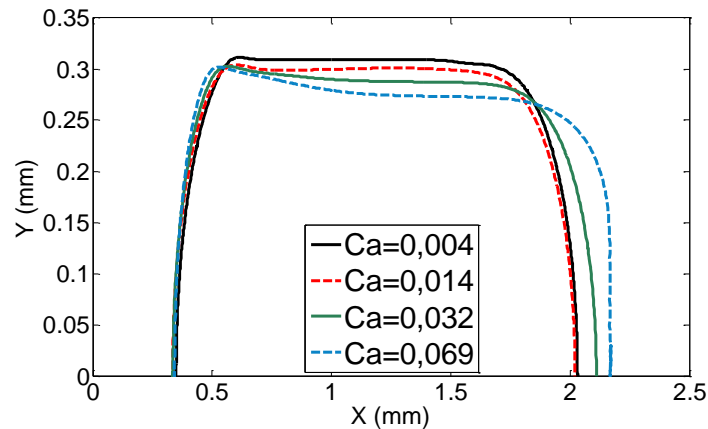


Figure 3.5

Bubbles' shapes at different capillary numbers. Operating conditions: $Re = 7.8$, original bubble radius = 0.32 mm, fluid velocity = $0.1 \frac{m}{s}$, gravity = $9.8 \frac{m}{s^2}$

The film thickness and terminal velocities from the numerical simulation are compared with Han's correlation and Taylor's law at different capillary numbers in Figure 3.6. When the capillary number is relatively high (7×10^{-2}), the numerical simulation slightly underestimates liquid film thickness. This is because the surface tension is usually dominant when the capillary number is smaller than 5×10^{-2} .

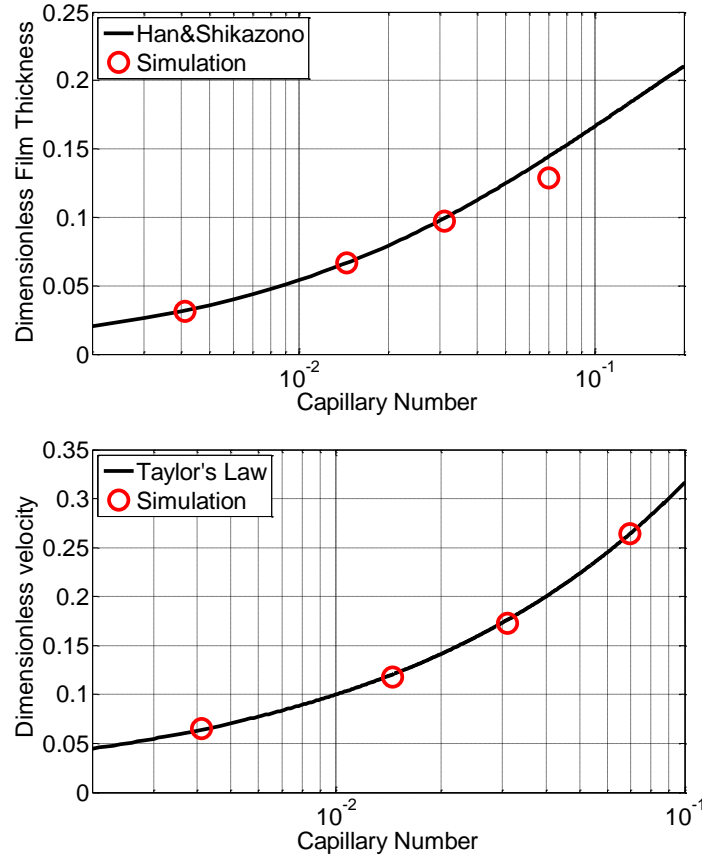


Figure 3.6

Top: Bubbles' dimensionless film thickness ($\frac{2\delta}{D}$) versus capillary numbers. Bottom: Bubbles' dimensionless terminal velocities vs capillary number. The black solid line represents the lubrication theory, and the red circles are the results of the simulation. The dimensionless velocity is defined as $\frac{u_b - u_f}{u_b}$, where u_b is the terminal velocities of bubbles and u_f is the mean fluid velocity. Operating conditions: $Re = 7.8$, original bubble radius = 0.32 mm, fluid velocity = $0.1 \frac{m}{s}$, gravity = $9.8 \frac{m}{s^2}$

3.7.2 Validation of the coalescence model

This validation case investigates co-axial coalescence of two spherical gas bubbles rising in an initially quiescent liquid in an axisymmetric domain. Two identical spherical gas bubbles with diameter $d_0 = 10 \text{ mm}$ are placed on the symmetry axis at the axial positions $z = 1.5d_0$ and $z = 3d_0$. The size of the domain and the grid are $4d_0 \times 8d_0$ and $0.2 \times 0.2 \text{ mm}$ respectively. As listed in Table 3.3, the properties of the fluid are the same as the experimental settings (Brereton & Korotney, 1991). The liquid to gas density and viscosity ratios are 100, which is greater than the value of most refrigerants.

Table 3.3 Properties of the working fluid for validation of the coalescence model

	Density (kg/m ³)	Eo	Mo	Surface Tension N/m	Viscosity Pa*s	Bubble Diameter mm	D to inlet mm	C to C Distance mm
Liquid	1273	16	0.0002	0.078	0.059	0.01	0.015	0.015
Gas	12.73				0.00059			

The top image in Fig. 3.7 illustrates numerical snapshots comparing the experimental results (Brereton & Korotney, 1991) and the lower image shows that the Reynolds number of the leading bubble calculated from the numerical simulation is always close to 50, which is the experimental value obtained by Bhaga and Weber (Bhaga & Weber, 1980).

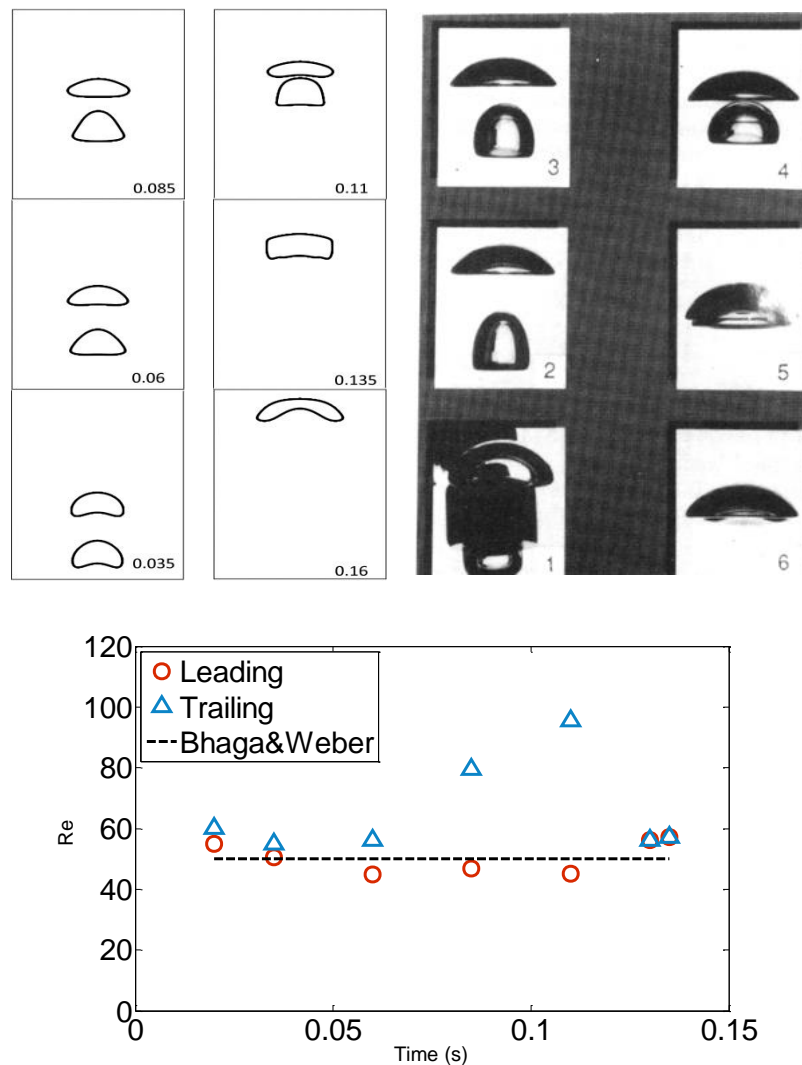


Figure 3.7

Snapshots at different times of the co-axial coalescence of two initially spherical gas bubbles in an initially quiescent liquid in a cylindrical column of , using a time step of 5×10^{-5} s. $E_o = 16$ and $Mo = 2 \times 10^{-4}$. The time difference between subsequent photographs is 0.03s (Brereton & Korotney, 1991).

3.7.3 Validation of the phase change model

The phase change model will be validated using both the classic Stefan problem and a gas bubble growing in a super-heated fluid.

3.7.3.1 Validation against the Stefan problem

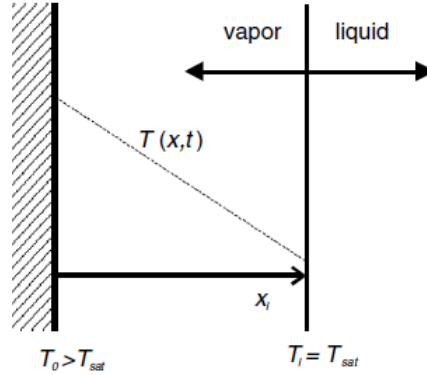


Fig.3.8. Specification of the Stefan problem (Hardt & Wondra, 2008)

The set-up of the validation is identical to that in Hardt and Wondra's paper (2008) and has been done in our published paper (Liu, Wang, & Palm, 2017b). As Fig. 3.8 indicates, heat is transferred from a super-heated and isothermal wall through a thin vapor region to a large liquid phase region. The temperature boundary conditions at the wall and interface are:

$$T(x = 0, t) = T_0, T(x = x_i(t), t) = T_{sat} \quad (52)$$

The initial position of the interface is set to be very close to the wall:

$$x_i(t = 0) = 10^{-6} \text{ m} \quad (53)$$

The analytical solution of the interface is given by Neumann (Gupta, 2003) as follows:

$$x_i(t) = 2\beta \sqrt{\frac{k_v}{\rho c_{pv}}} t \quad (54)$$

Where $\frac{k_v}{\rho c_{pv}}$ is the thermal diffusivity of vapor and β is determined from the error function:

$$\beta \exp(\beta^2) \operatorname{erf}(\beta) = c_{pv} \left(\frac{T_0 - T_{sat}}{\sqrt{\pi} h_{lg}} \right) \quad (55)$$

Table 3.4 Material properties for the Stefan problem

Name	Density	Viscosity	Specific heat	Thermal conductivity	Surface tension	Latent heat
Unit	ρ kg/m^3	μ mPas	Cp J(kg/K)	k $\text{W/(m}^{\circ}\text{K)}$	σ mN/m	h_{lg} J/kg
Vapor	1	10^{-2}	10^3	$10^{-1/-2/-3}$	100	10^6
Liquid	10^3	10	10^3	10^{-1}		

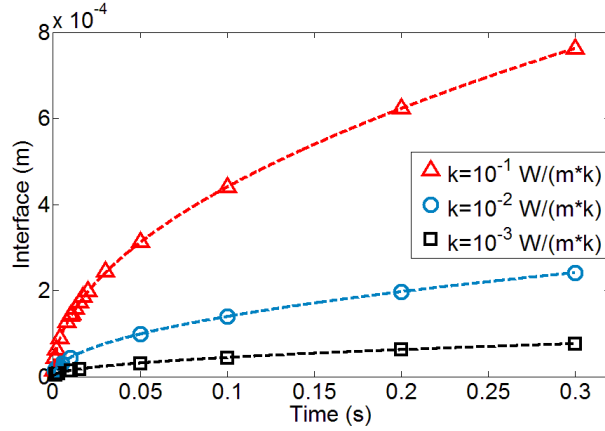


Fig. 3.9. Interface position as a function of time for the Stefan problem in the present paper. The dashed lines and symbols represent analytical and numerical results respectively. Red, blue and black denote fluids with vapor thermal conductivity of 10^{-1} , 10^{-2} , and 10^{-3} W/(m*k) respectively.

Vapor and liquid properties are listed in Table 3.4. The saturation temperature is 373.15K, the wall is super-heated by 10K, and an evaporation coefficient of 1 is chosen. The extension of the computational domain is 1mm.

The numerical results of the interface position as a function of time are compared to analytical values in Fig. 3.9. This indicates that evaporation increases with an increasing thermal conductivity: vapor with higher thermal conductivity makes evaporation of the liquid go much faster.

3.7.3.1 Validation against Scriven's expression

Scriven (Scriven, 1959) has derived an analytical expression for a bubble growing in a super-heated liquid. This indicates that bubble radius is a function of time.

$$R(t) = 2 \beta \sqrt{\alpha t}, \quad (56)$$

where β is the growth constant and α is the liquid thermal diffusivity

$$\beta = \sqrt{\frac{3}{\pi} \frac{\rho_g}{\rho_l} \frac{\Delta T}{\left(\frac{L}{c_l} + \left(\frac{c_l - c_g}{c_l}\right) \Delta T\right)}}. \quad (57)$$

In this section, a spherical R134a gas bubble with an initial radius of 0.1mm is placed in a superheated liquid in an unbounded axisymmetric container. With this radius, the bubble is large enough that the difference in saturation temperature across the interface can be neglected. Gravity is set to be zero and the pressure is 0.84bar. Initially the liquid is quiescent and super-heated with 5K, and the bubble is at saturation state (i.e. $T_{\text{bubble}}=T_{\text{sat}}$). A comparison of numerical results of the bubble radius to Scriven's expression is presented in Fig. 3.10. At time after 1.5ms or bubble radius larger than 0.2mm, numerical simulation tends to slightly overestimate the bubble's growth. This is partly because the unbounded condition is not appropriate for experiments when the bubble is large.

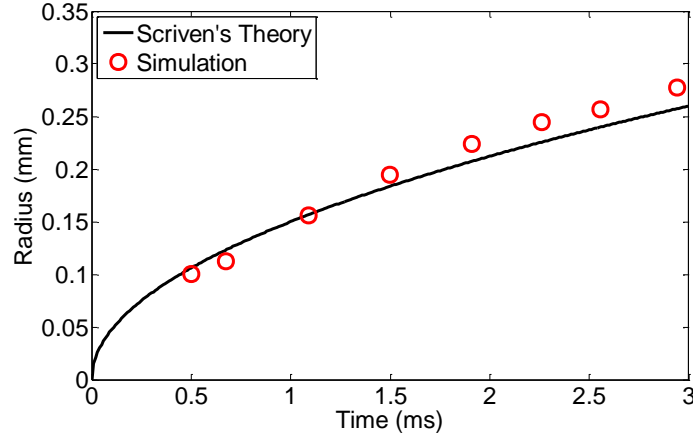


Figure 3.10. Radius of bubbles over time compared with Scriven's theory. Working fluid: R134a. Super heat degree of liquid: **5 K**, and the operating pressure is **0.84 bar**.

3.7.4 Comparison with existing methods

Two cases using the new CLSVOF (coupled level set and VOF) and non-equilibrium smeared phase change models are compared to the existing method (VOF and non-smeared phase change model respectively). Both cases have a spherical vapor bubble rising in superheated liquid in a channel with a diameter of 0.64mm. The liquid density is 1000kg/m³, and vapor density is 10kg/m³. Viscosity for liquid and gas are 10 and 10⁻²mPa*s respectively. The surface tension coefficient is 0.1N/m and the initial bubble diameter is 0.4mm. As shown by Fig. 3.11, bubble shapes using CLSVOF and VOF at 5ms have different appearances. The one calculated by VOF method has more spurious current at the interface, while CLSVOF has better accuracy.

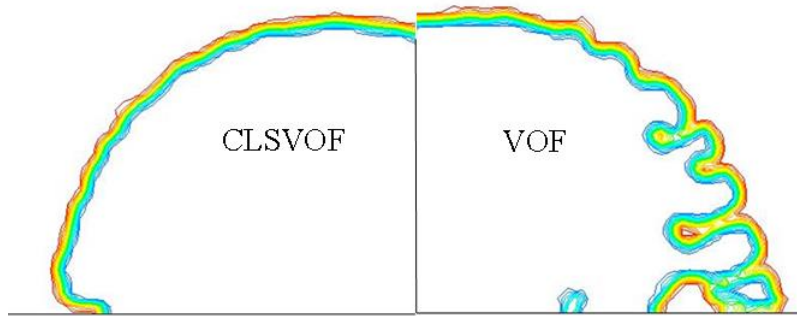


Fig. 3.11. Bubble shapes using different interface tracking methods

The second case concerns the non-equilibrium smeared phase change model. The liquid is set to be five degrees super-heated. Thermal conductivity is 10⁻¹ and 10⁻³ kW/(m*K) for liquid and gas respectively. The latent heat is 10⁶ J/kg and specific heat capacity is 10³ J/(kJ/kg). Simulation results reveal that the smeared phase change model has a smoother interface than the non-smeared model (Fig. 3.12).

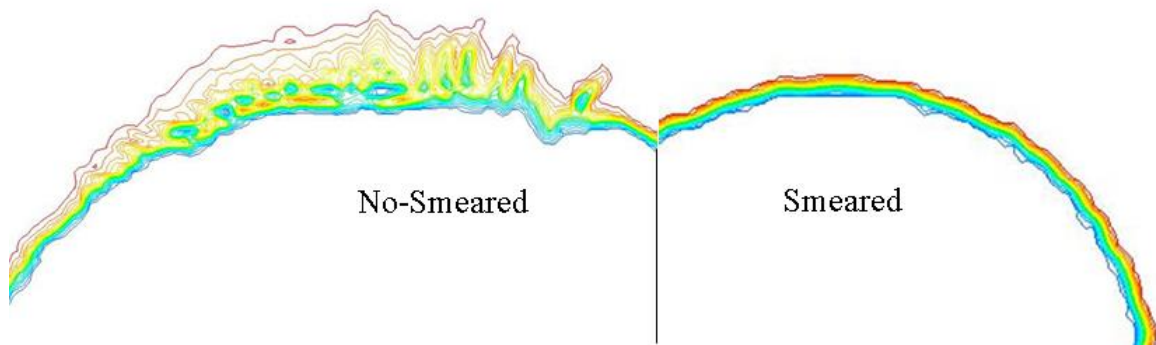


Fig. 3.12. Bubble shapes by using different phase change models

Summary

This chapter describes the general theory of computational fluid dynamics, discretization schemes, interface capturing methods, phase change models, and set up of the simulation domains. Validations have been made against classic theoretic solutions and experiment results from literature. Specifically, the first case validates the coupled level set and VOF method against classic lubrication theory and Shikazono's experiment results, the second case validates the coalescence phenomenon against an experiment result, and the third case validates the phase change model against the classic Stefan problem and super-heated gas bubble correlation. Simulation results are well in agreement with validating benchmarks, thus laying a solid foundation for studies in the following chapters.

4 Nucleate to confined bubbly flow transition

The transition from nucleate to confined bubbly flow in mini/micro channel seems less chaotic than that in larger channels. In tubes with a diameter larger than a few centimeters, nucleate bubbles could rising and merge randomly. However, in mini/micro channels, due to the channel confinement, nucleate bubbles rise and merge in a more orderly way. In certain cases, even symmetry merging is observed. In this chapter, a simple nucleate-to-confined bubbly flow transition model is presented. It assumes that after the onset of nucleate, two symmetrical bubbles are moving up in the vicinity of the wall. After a certain time they have grown large enough to meet and merge. A few assumptions are summarized as follows:

- 1 the bubbles are generated symmetrically with respect to the central plan of the circular tube.
- 2 the flow is laminar.
- 3 the roughness and the thickness of the tube wall is neglected.

This chapter is a summary of a published paper(Liu & Palm, 2016) by the author.

4.1 Boundary and initial conditions

A 1.6mm long micro channel with a diameter of 0.64mm is studied in this section (Fig. 4.1). Gravity has a -Z direction. Only a quarter of the tube is calculated because two perpendicular and symmetric boundaries are defined at the center of the tube, which reduces computational time significantly.

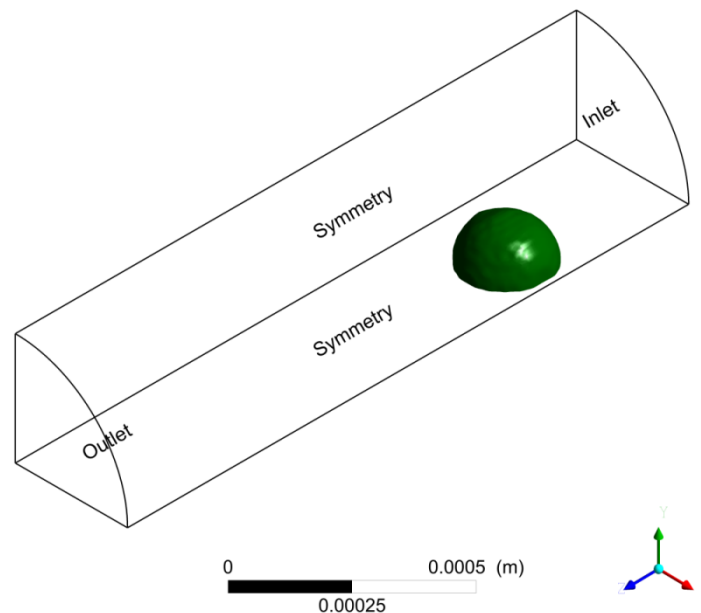


Figure 4.1. Simulation domain and bubble placement. Bubbles' initial radiuses are 0.11mm and are placed 0.4mm from the inlet. Inlet Reynolds number is 549 and the wall heat flux is 14 or 28 kW/m². Saturation temperature is 300.15K. Blue arrow points to Z direction, red arrow to X direction and green arrows to Y direction.

A single-phase steady simulation is performed before and the result is used as initial condition for the two-phase study. The wall is set to be no-slip velocity boundary and a constant heat flux (14/28 kW/m²) is supplied at it.

A uniform velocity (0.256m/s) and temperature (300.15K) boundary condition is used at the inlet for both the single- and two- phase simulation. Renolyds numbers of all the cases are smaller than 2100 which means they are laminar flows. The value of contact angle Θ_{\max} between fluid R134a and aluminum wall is 14° (Vadgama & Harris, 2007).

The thermal entry length corresponding to the given inlet velocity (0.256m/s) can be calculated by equation (58). In this section the value is 82D, which means all cases are in the thermal entry region.

$$\frac{L_e}{D} = 0.05Re \cdot Pr \quad (58)$$

A pair of spherical “embryo bubbles” are introduced attach to the wall initially. Their distances from the inlet are 0.4mm and are initialized above a critical size(Carey, 1992), The operating pressures are 7.06bar (saturated temperatures 300.15K).

4.2 A comparison with a visualization

This section presents a case where two pairs of bubbles rising side by side and merging laterally. A comparison between our simulation and a visualization study (Owhaib, 2009) under the same conditions is illustrated by Fig. 4.2. It concerns two pairs of bubbles sliding along a wall in a upward R134a flow in a 0.64mm wide channel. It is clearly show that that bubbles coalescence consist of three stages: sliding, merging and post-merging (departure).

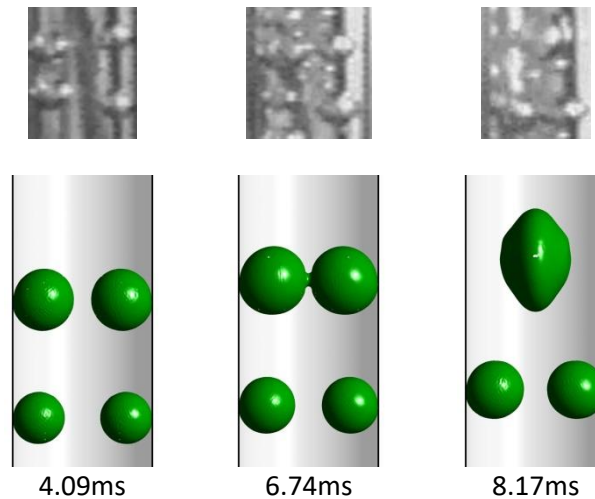


Figure 4.2

Comparison of an experimental visualization and the present simulation at different times. Boundary conditions: $q = 5 \frac{kW}{m^2}$, mass flux $G = 112 \text{ kg} \cdot \frac{m^2}{s}$, saturation temperature $T_{sat} = 300.15 \text{ K}$.

4.3 A simple model of bubble merging

This section presents a simple model of bubble merging, which makes flow regime transfer from isolated bubbles to confined bubbly flow. It assumes that two identical spherical bubbles rising symmetrically in a channel and coalesce. The coalescence is primarily caused by evaporation and it is one of the flow regime transition mechanism.

4.3.1 Dynamics of the growing and merging process

Slightly different from section 4.2, only two bubbles but not two pairs of bubbles (four bubbles in total) rising side by side are presented in this simple model. As Fig. 4.3 shows, two identical spherical bubbles rise and grow in a channel with a heated wall. At 4ms, the two bubbles have grown big enough to merge. This merging period is an extremely quick process where the surface tension force pulls the two bubbles away from the wall within one mini-second. The new merging bubble initially expands in the radial direction first (4.5ms for $q=28 \text{ kW/m}^2$, and 6.4ms for $q=14 \text{ kW/m}^2$), and then quickly contract (4.9ms for $q=28 \text{ kW/m}^2$, and 6.7ms for $q=14 \text{ kW/m}^2$).

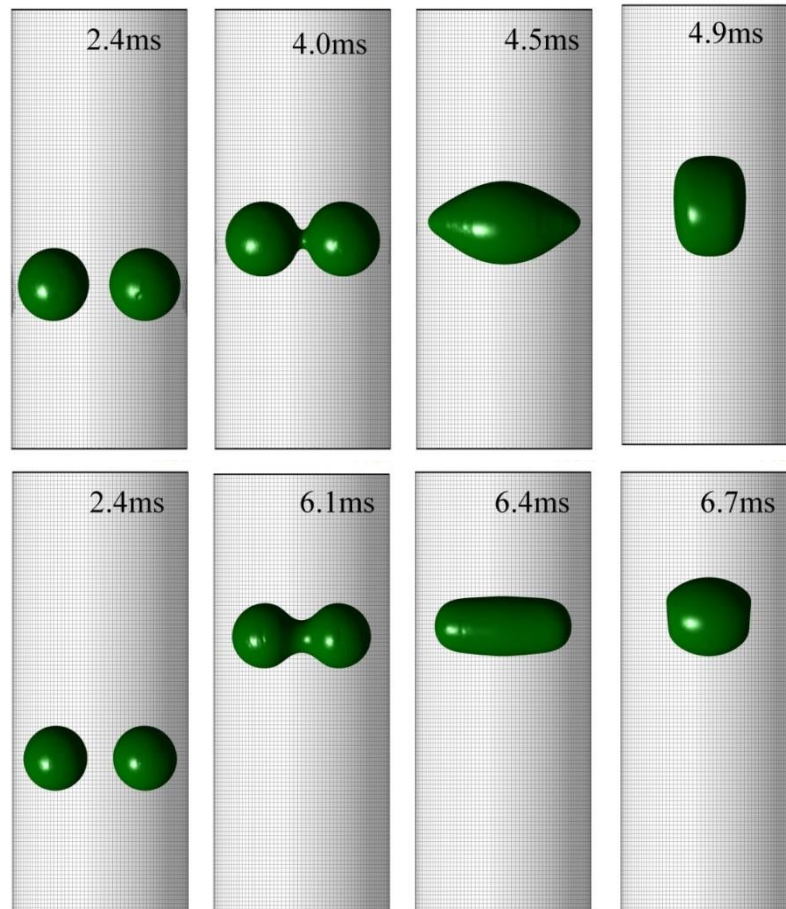


Figure 4.3

Changes in bubble shape with time. Constant wall heat flux $q = 28$ (top) and 14 (bottom) $\frac{\text{kW}}{\text{m}^2}$, inlet $\text{Re} = 549$, saturation temperature $T_{\text{sat}} = 300.15 \text{ K}$.

Fig. 4.4 presents velocity fields around the bubbles of case $q=28 \text{ kW/m}^2$. The velocity field is relatively uniform initially (1.9ms) but distorted by the merging process (4.0-4.5ms). The expansion of the bubble along the centerline causes a vortex close to the wall.

The bubbles' vertical (axial) and radial velocities are presented in Fig. 4.5. Both are defined as the mean velocity of the whole gas bubble and the minus values denote that they are moving toward the channel center. Both velocities peak during the merging process due to the surface tension (4-4.5ms).

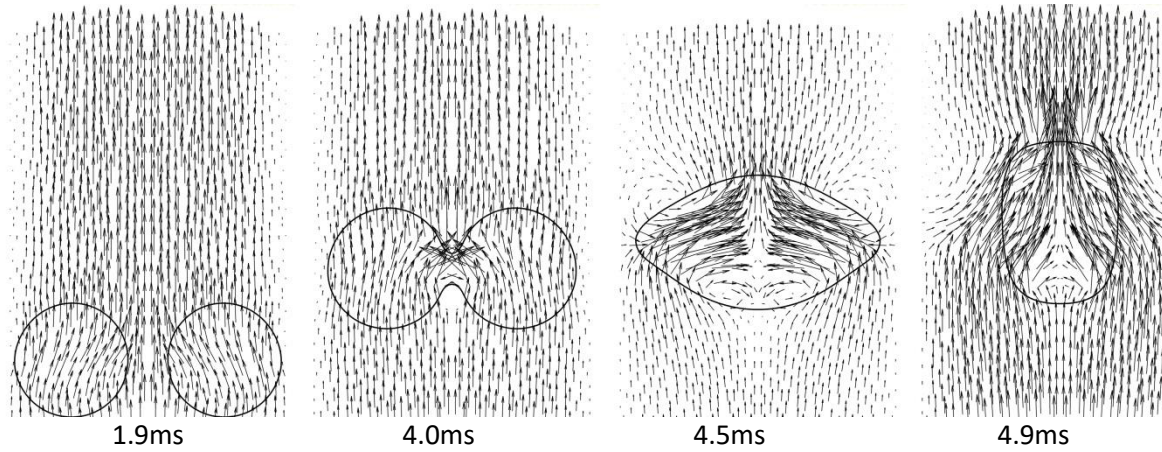


Figure 4.4

Fluid velocity at the central plane at different stages of the merging process. Boundary conditions: constant wall heat flux $q = 28 \frac{\text{kW}}{\text{m}^2}$, inlet $\text{Re} = 549$, saturated temperature = 300.15 K .

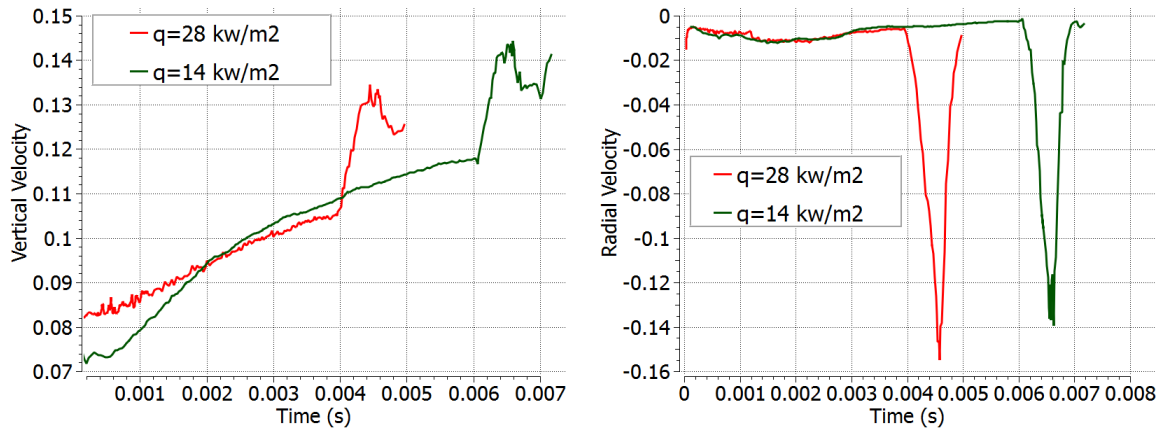


Figure 4.5

Bubble velocity (m/s) at different stages. Boundary conditions: constant wall heat flux $q = 14 \text{ and } 28 \frac{\text{kW}}{\text{m}^2}$, inlet $\text{Re} = 549$, saturation temperature = 300.15 K .

4.3.2 Heat transfer

Fig. 4.6 illustrates the temperature field of channel cross section of case $q=28 \text{ kW/m}^2$. In the first stage of merging (sliding), the temperature in part of the thermal boundary layer (closing to the bubbles) is decreased mainly due to the bubbles' evaporation. The thermal boundary layer is continuously "ironed" by the bubbles upward movement. During the merging process (4.5ms), the thermal boundary layer is thinned by the new merging bubble's expansion. However, after that it rebounds.

Fig. 4.6 presents the wall temperature. Initially (2.0ms), the local wall temperature at the point closest to the bubbles ($0.004\text{mm} < Z < 0.006\text{mm}$) is the lowest, which is mostly due to the bubble's contact. As the bubbles departure from the wall, this local temperature increases and then keeps almost constantly.

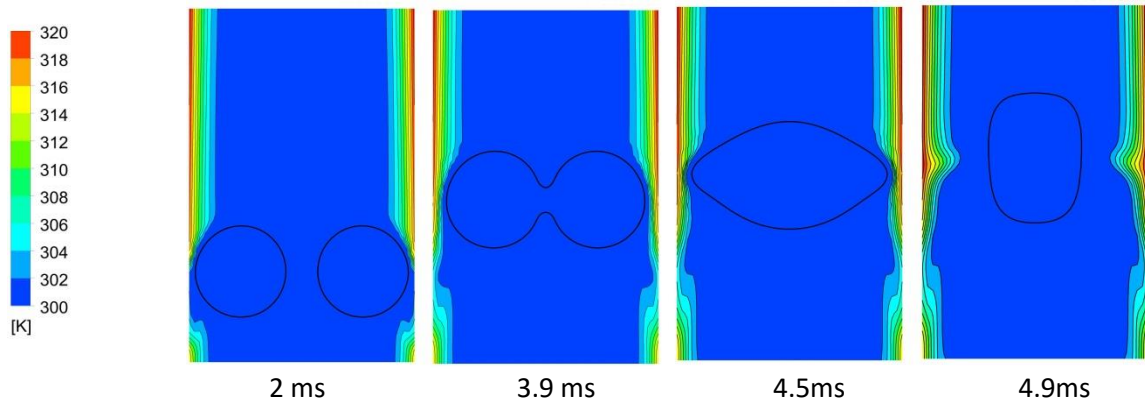


Figure 4.6

Temperature contour at different stages. Boundary conditions: constant wall heat flux: $q = 28 \frac{\text{kW}}{\text{m}^2}$, inlet $\text{Re} = 549$, and saturation temperature $T_{\text{sat}} = 300.15 \text{ K}$.

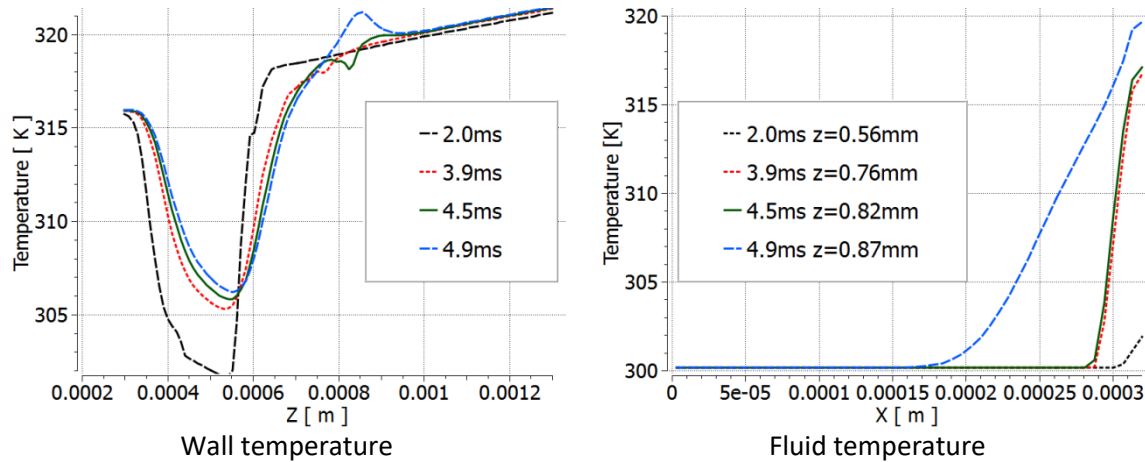


Figure 4.7

Wall (left) and fluid temperature (right) at different stages. Boundary conditions: constant wall heat flux $q = 28 \frac{\text{kW}}{\text{m}^2}$, inlet $\text{Re} = 549$, and saturation temperature $T_{\text{sat}} = 300.15 \text{ K}$.

The fluid temperature of the cross section is plotted in Fig. 4.7. It represents the temperature of fluid around the bubbles at a line in YZ plane. The line changes its vertical position (Z coordinates) as the bubbles moving upwards (0.56 0.76 0.82 0.87mm at 2.0, 3.9, 4.5, 4.9ms respectively). In the sliding process (2.0ms), the thermal boundary layer is very thin (0.01mm) and the fluid temperature around the bubbles almost equal to the saturation temperature (300.15 K). In the merging process, the boundary layer grows to about 0.03mm and fluid temperature increases to as high as 317K, because the bubbles have left the wall.

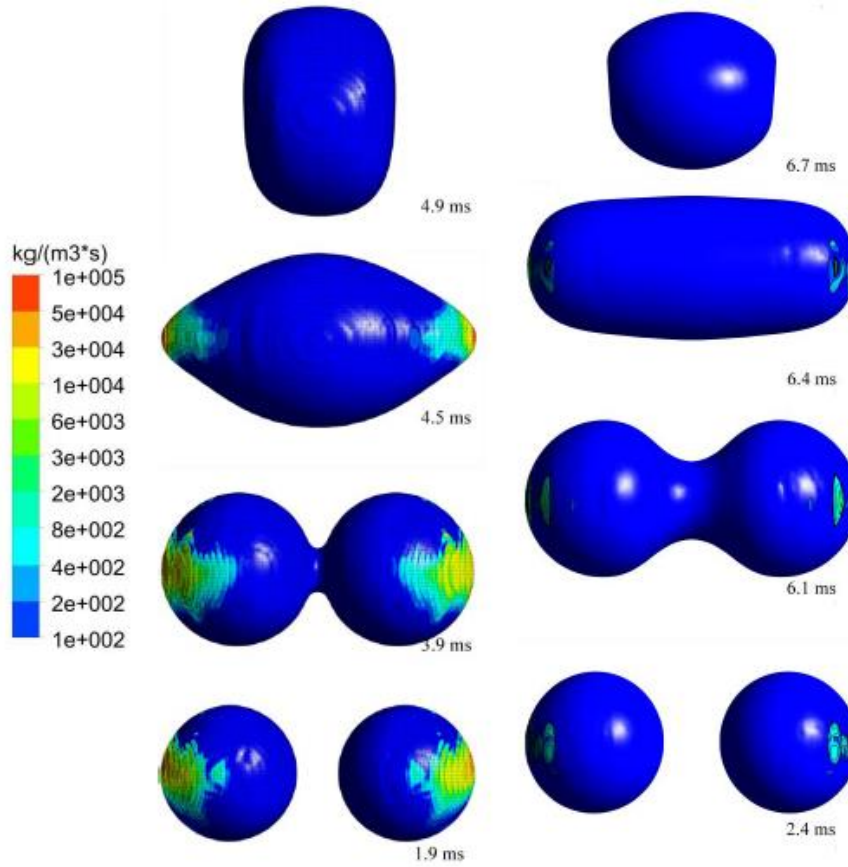


Figure 4.8

Evaporation rate contour at different times. Constant wall heat flux $q = 28 \frac{kW}{m^2}$ (Left), and $14 \frac{kW}{m^2}$ (Right), with inlet $Re = 549$, and saturation temperature $T_{sat} = 300.15 K$.

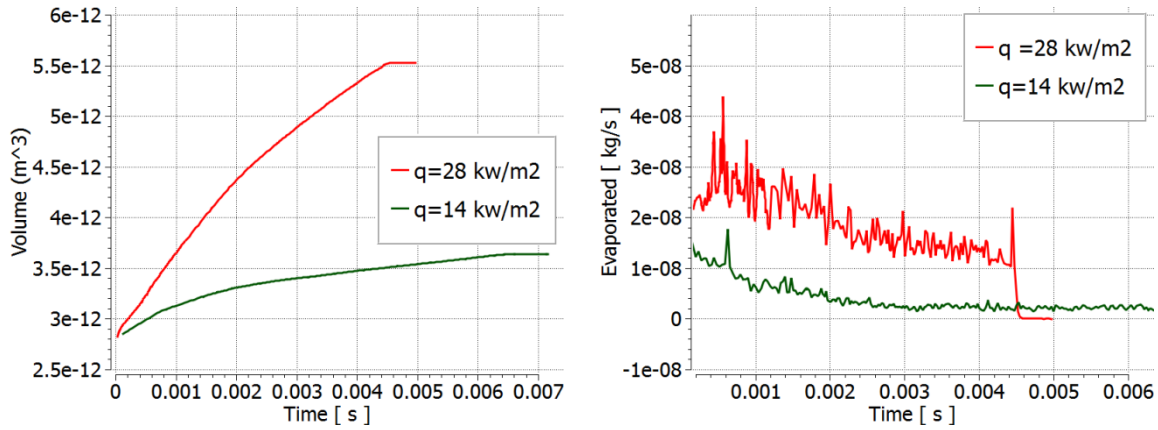


Figure 4.9

Bubble growth and total evaporation rate at different times. Constant wall heat flux $q = 14$ and $28 \frac{\text{kW}}{\text{m}^2}$, inlet Reynolds number $Re = 549$, and saturation temperature is $T_{sat} = 300.15$.

The contour of the evaporation rate at the bubbles is shown in Fig. 4.8. Most evaporation takes place at bubbles' gas-liquid interface near the wall. Both evaporation rate and interface area are high in the sliding stage and decreases with the moving and merging of bubbles.

Fig. 4.9 illustrates the bubble growth and the total evaporation rate. It indicates that a higher wall heat flux causes a higher bubble growth rate. Bubbles grow bigger during the sliding and merging process. However, their evaporation rate decreases along this period. When the bubbles departure from the wall in case $q = 28 \text{ kW/m}^2$, the evaporation has even declined to zero.

4.3.3 Sub-cooling effects

Fig. 4.10 presents bubbles growth under saturated or sub-cooled inlet conditions. Under sub-cooled inlet condition, bubbles grow slower (Fig. 4.11) and do not merge even though the sub-cooling degree is only one Kelvin.

The fluid temperature of channel cross section is drawn in Fig. 4.12. Bubble movement disturbs the thermal boundary layer and lower wall temperature. In the sub-cooled case, both evaporation and condensation take place. Bubbles receive heat from the thermal boundary layer and emit heat at the center of channels.

A bubble heat transfer coefficient is defined as the ratio of heat flux to temperature difference between the wall and the bulk fluid as follows

$$h_b = \frac{q}{T_w - T_{f,bulk}} \quad (59)$$

Fig. 4.13 plots the heat transfer coefficient in saturated and sub-cooled conditions. Saturated heat transfer coefficient is higher than that in sub-cooled inlet condition. And both are higher than single-phase convection.

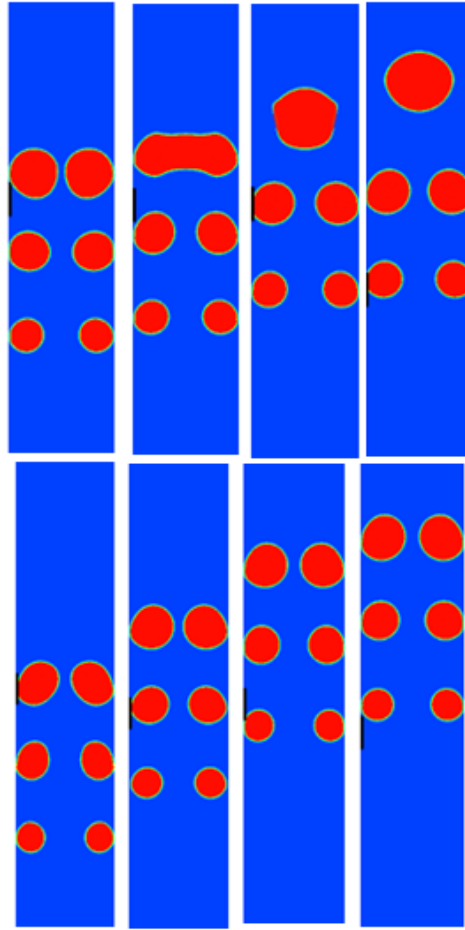


Fig. 4.10. Bubbles movement in saturated (top) and one degree sub-cooled (down) conditions.

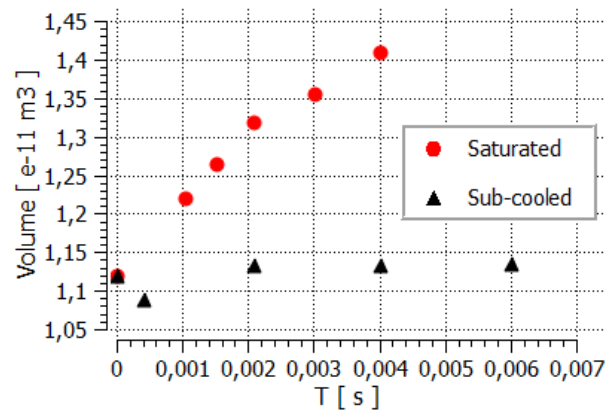


Fig. 4.11. Bubbles volume in saturated and subcooled conditions $q = 10 \frac{kW}{m^2}$, $\dot{m} = 335 \frac{kg}{m^2 \cdot s}$

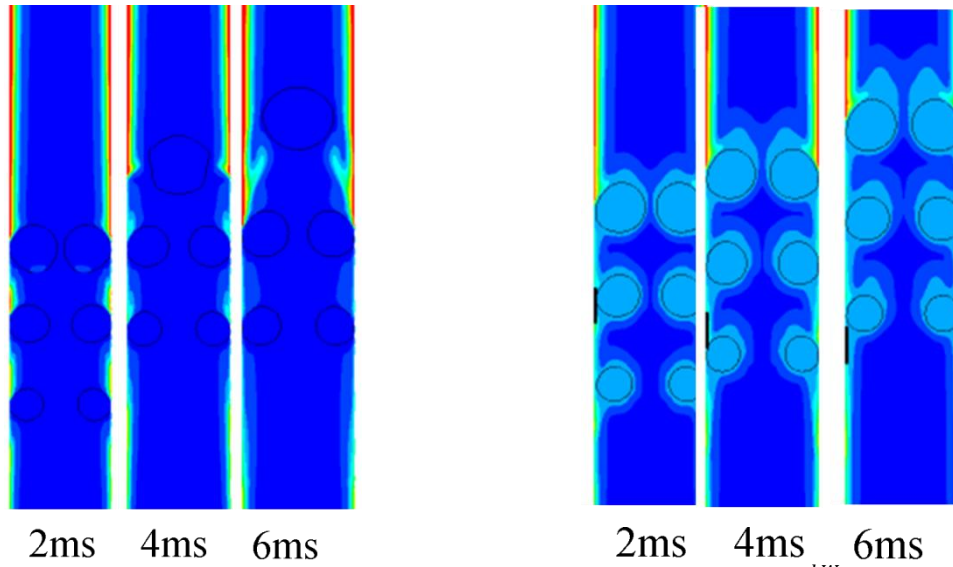


Fig. 4.12. Temperature profile in saturated and subcooled conditions $q = 10 \frac{kW}{m^2}$, $\dot{m} = 335 \frac{kg}{m^2 \cdot s}$

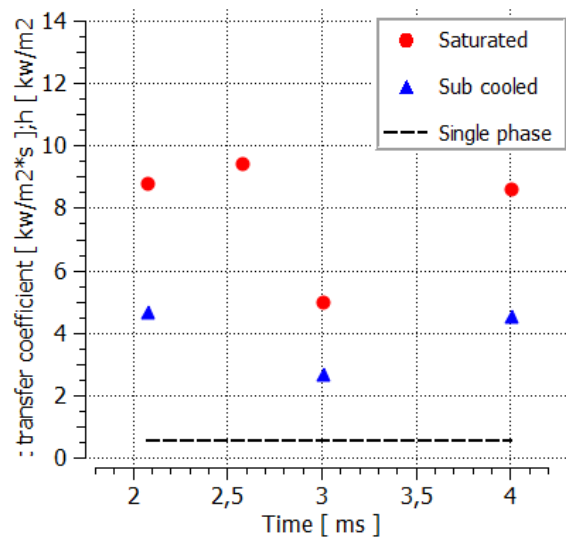


Fig. 4.13. Heat transfer in saturated and subcooled conditions $q = 10 \frac{kW}{m^2}$, $\dot{m} = 335 \frac{kg}{m^2 \cdot s}$

4.4 Multiple bubbles merging

Three pairs of bubbles merging are studied in this section. A single-phase steady laminar simulation with a constant wall heat flux is performed at the beginning and the result is used as the initial condition for the multiphase simulation. A constant heat flux (5, 10 or 15 kW/m²) is supplied at the wall. A no-slip velocity boundary condition is applied for the wall. The system operating pressure is 7.06bar.

Table 4.1. Simulation parameters for multiple bubbles merging

Saturation temperature (K)	300.15				305.15		
initial radius (mm)	0.08/0.1/.12				0.1/0.12/0.14		
	Case 1	Case 2	Case 3	Case 4	Case 5	Case 6	Case 7
mass flux(kg/m ² *s)	56	56	112	200	200	200	335
heat flux (kW/m ²)	5	10	5	5	10	15	10
initial volume (10 ⁻¹² m ³)	6.7	6.7	6.7	6.7	6.7	6.7	6.7
Reynolds Number	198	198	396	712	712	712	1098

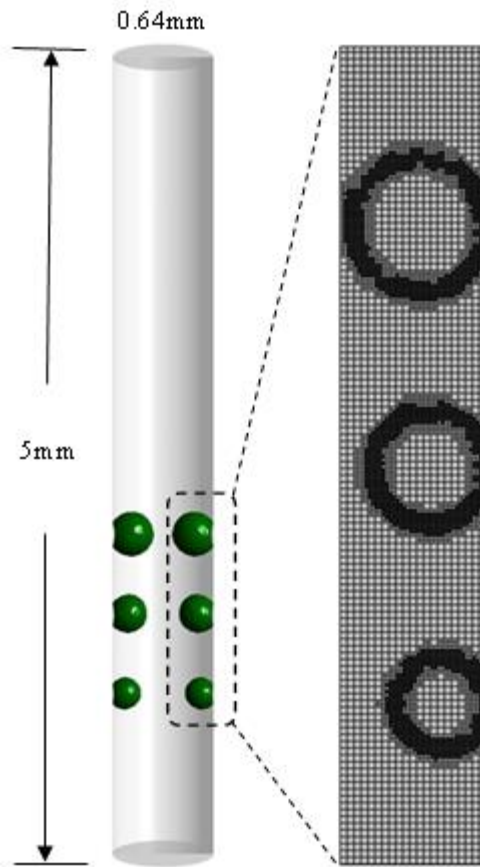


Fig. 4.14. The simulation domain is a 5 mm long cylinder with a diameter of 0.64 mm placed vertically. The bubbles' diameters are 0.1, 0.12 and 0.14 mm for cases with high saturation temperature (305.15K) and 0.08, 0.1, and 0.12 mm for cases with low saturation temperature (300.15 K).

Uniform velocity and temperature boundary conditions are used at the inlet for the single-phase simulation, and the results are used as the inlet condition for the multiphase simulation. Some of the important settings are listed in Table 4.1.

These values imply that the inertia force is negligible compared to viscous force and there is a laminar flow regime since the Reynolds numbers of all cases are much smaller than 2100. The value of contact angle θ_{max} is 13° which comes from experimental results of the flow of R134a through an aluminum wall (Vadgama & Harris, 2007).

4.4.1 Effects of heat flux

Fig.4.15 illustrates the cross-section fluid temperature contour as well as the bubbles' shapes with different wall heat flux. Under the same mass flux and saturation temperature, bubbles grow faster with high heat flux (15 kW/m^2) than in low heat flux ($q = 5\text{ kW/m}^2$). In the latter case, the leading bubble pair has not grown large enough to merge until the end of calculation.

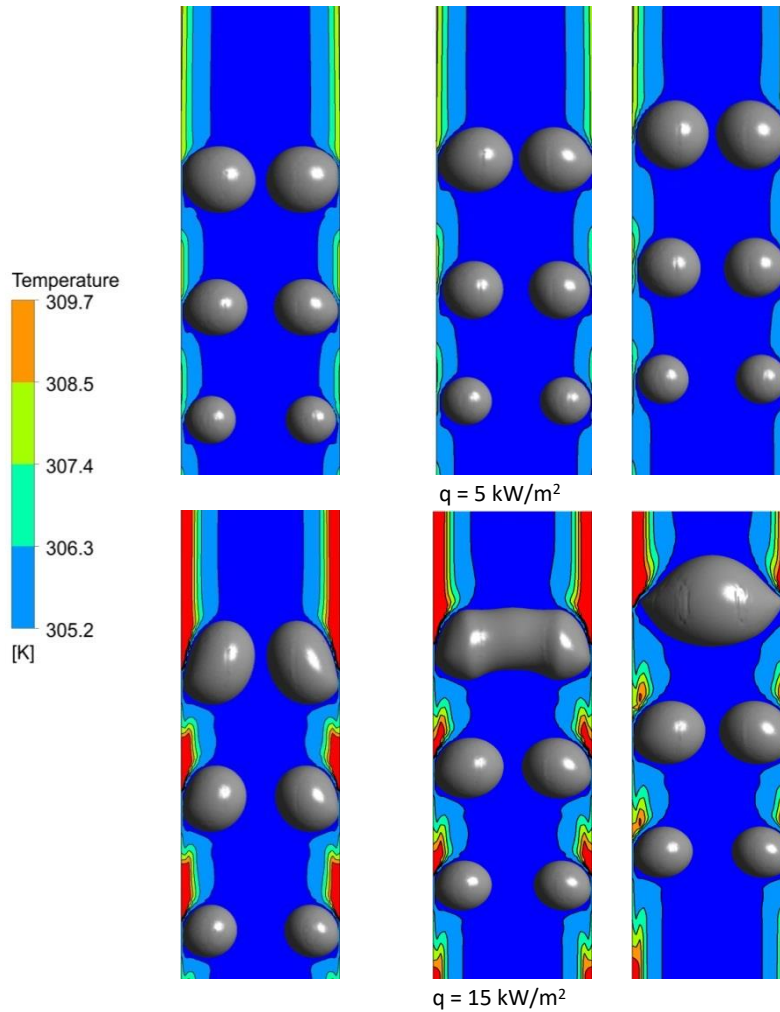


Fig. 4.15. Bubbles grow at different wall heat fluxes. The time span between two snapshots is 0.5ms and the first snapshot is taken at time 1.0ms. Mass flux $G=335 \text{ kg}^*/\text{m}^2/\text{s}$, and saturated temperature $T_{\text{sat}}=305.15 \text{ K}$.

Fig. 4.15 plots bubble growth under different mass flux and saturation temperature (pressure) condition. Three different wall heat fluxes are examined here, namely: 5, 10, and $15 \text{ kW}/\text{m}^2$. Under either saturation temperature (305.15 or 300.15K), the bubbles' growth rate increases with rising wall heat flux.

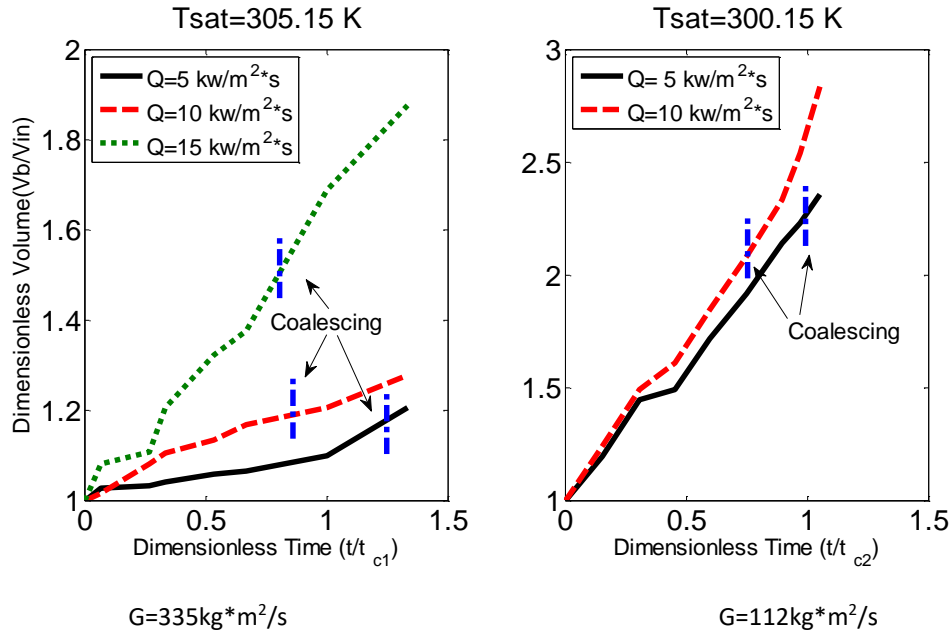


Fig. 4.16. Bubbles' volume versus time at different heat fluxes. V_b and V_{in} are the bubble volume and initial total bubble volume of six bubbles respectively. t_{c1} and t_{c2} are the coalescing time for two case groups and have values of 1.5 and 6.7ms respectively.

4.4.2 Effect of mass flux

The movement of three pairs of bubbles under four different mass fluxes (56, 112, 200, and 335 kg/m²/s) is examined in this section. All are laminar flows since their Reynolds numbers are smaller than 2100.

Fig. 4.17 and Fig. 4.18 show velocity streamlines and bubble growth rates under different mass fluxes. A declining mass flux leads to an increasing bubble growth rate. This is due to a lower mass flux having a higher liquid temperature field when heat flux remains unchanged. Therefore bubbles with lower inlet mass flux will usually grow faster and merge earlier (Fig. 4.18).

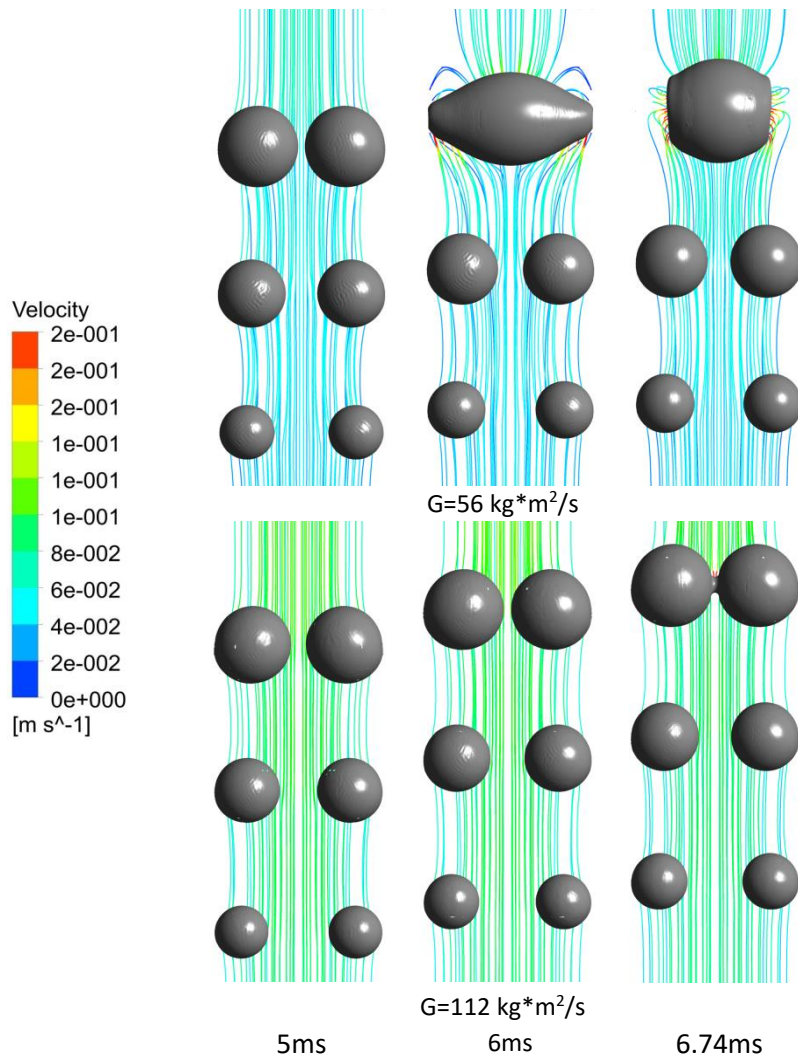


Fig. 4.17. Bubbles grow with different inlet mass fluxes. Boundary conditions: constant wall heat flux $q = 5\text{ kW/m}^2$, saturated temperature $T_{\text{sat}}=303.15\text{ K}$.

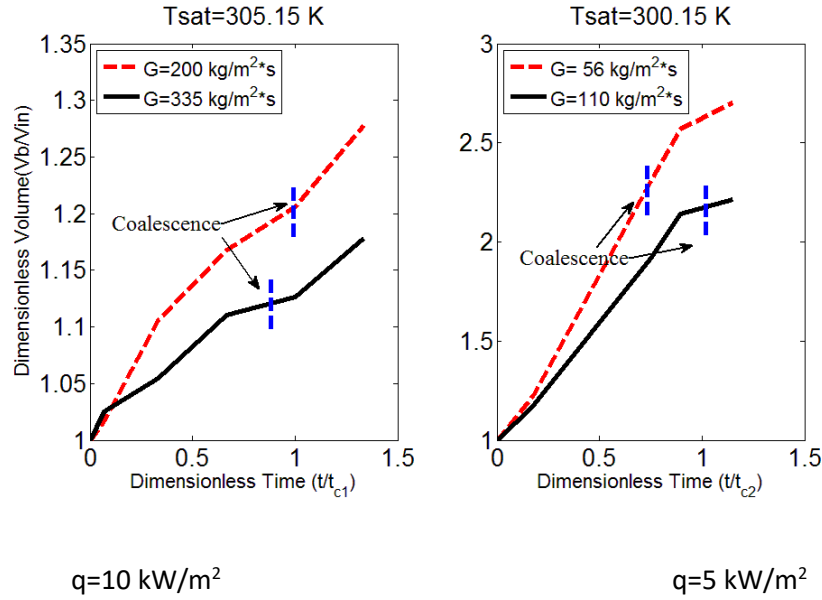


Fig. 4.18. Bubbles grow with different mass fluxes. V_b and V_{in} are the bubble volume and initial total bubble volume of three bubble pairs respectively. t_{c1} and t_{c2} are the coalescing time for two case groups and have values of 1.5 and 6.7ms respectively.

4.5 Summary

This chapter performs a three-dimensional numerical study of the bubbles' growth and merging during convective boiling in a micro channel with a diameter of 0.64 mm with a constant heat flux at the wall, fully developed velocity profile at the inlet, constant fluid temperature at the inlet and in most cases at the saturation temperature. The dynamics and heat transfer of the bubbles during the sliding and merging process have been investigated in detail. The results show that the process is complicated. It is also found that this merging process plays a key role in the heat transfer of flow boiling in micro channels. The following conclusions can be drawn based on the study:

- 1 The transition process can be roughly divided into three stages: sliding, merging and post-merging stages. The latter two stages are both extremely fast processes which take less than one millisecond. The dynamics and heat transfer are very different in these three stages.
- 2 In the sliding stage, bubbles have a relatively high growth rate but low velocity (both vertical and transverse velocities). The thermal boundary layer is highly distorted and thinned close to the bubble during this time, and therefore a relatively high rate of heat transfer is taking place between the fluid and channel wall.
- 3 In the merging stage, surface tension is so strong that the formation of a new bubble can take place within one millisecond. The expansion of the bubble along the radial direction makes the bubble protrude into the thermal boundary layer and hence enhances heat transfer. During this stage the bubble has a relatively moderate growth rate.

4 After that, the bubble contracts at a very fast pace and the majority of it has left the thermal boundary layer. It also pulls the fluid from the wall which locally makes the thermal boundary layer thicker. During this post-merging stage the bubble has a very low (even zero) bubble growth rate.

5 Both the mass flux and the heat flux affect the bubbles' growth and merging. A lower mass flux or a higher wall heat flux leads to a higher bubble growth rate and mostly an earlier merging under low Reynolds numbers.

6 The bubbles will merge with each other during saturated boiling after departing from the wall. Conversely, the merging does not occur in the calculation domain under the sub-cooled condition due to a much lower bubble growth rate.

7 Heat transfer enhancement in saturated flow boiling is mainly due to evaporation, and it is therefore simply a temperature controlled process. However, the sub-cooled process has a more complicated mechanism. The effects of the sub-cooling degree, heat flux and mass flux may play an important role and need to be further studied.

5 Confined bubbly flow regime

This chapter is based on a published conference paper (Liu, Palm, & Anglart, 2012) and one manuscript. The first paper investigates a single confined bubble, and the second studies a confined bubble train moving in a micro channel.

5.1 Single confined bubble

After a certain distance from the micro channel's inlet, the fluid has usually been heated up to its boiling temperature and boiling begins. The point at which boiling begins remains a debatable topic, although the majority of research community believes that vapor trapped in the small caves of the wall initiates this process. The newly generated bubbles are surrounded by a superheated liquid boundary layer which makes them grow and merge rapidly. This process is extremely fast and turbulent, and thus after only a very short time all bubbles in the same transverse position have merged into a large bubble and the flow has evolved to bubbly flow regime. The bubble can grow to a few millimeters, which is the same magnitude as the size of the micro channel. Thus the bubble is "confined" by the channel's wall and this flow regime is only observed in micro or mini channels. The heat transfer mechanism of this flow regime is believed to be different from other parts of the channel. In this section, a single confined bubble will be examined. The effect of surface tension, Reynolds number, and initial bubble shapes will also be studied.

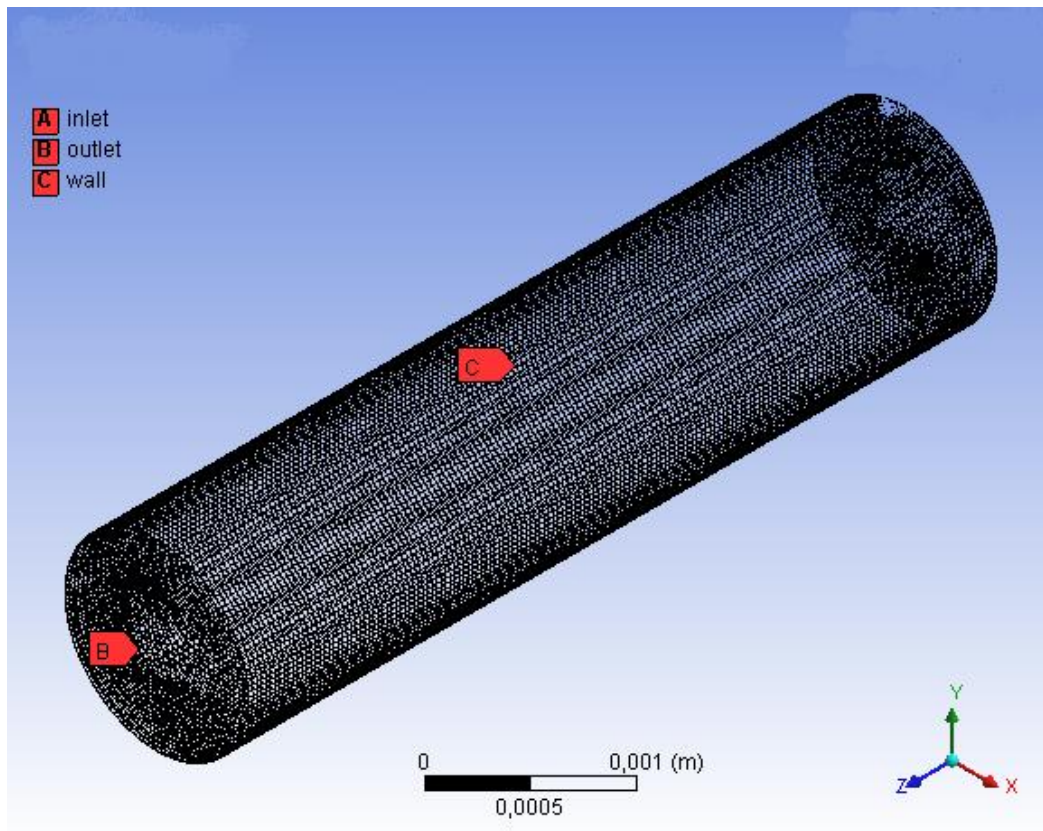


Fig. 5.1 Simulation domain of the micro channel. Its diameter is 0.64mm and its length is 5mm.

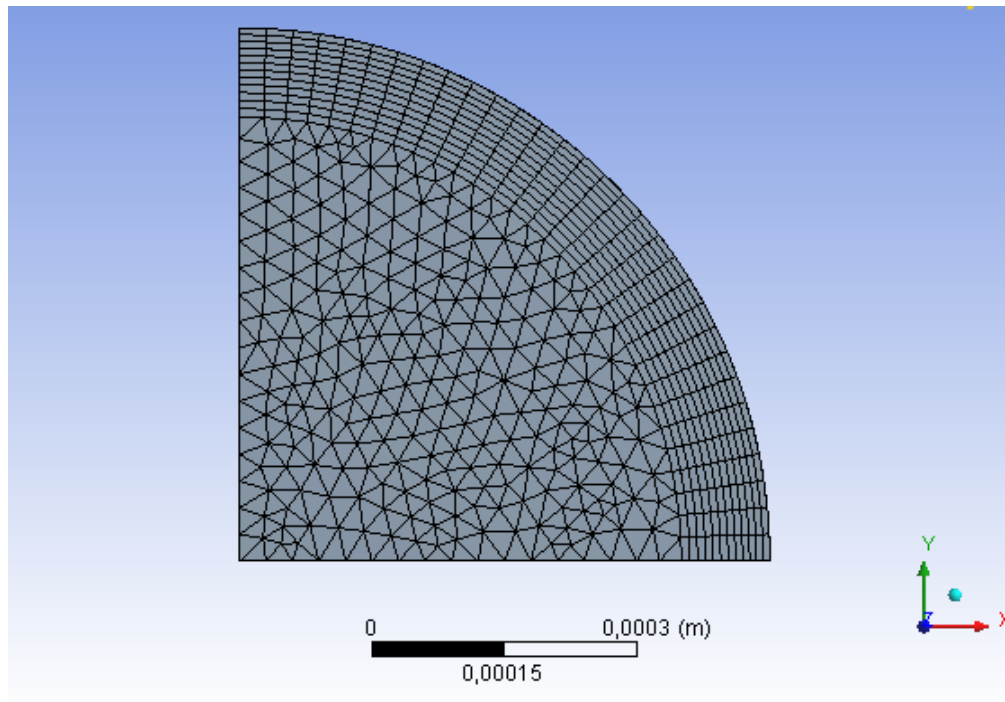


Fig. 5.2 Mesh generation of a channel for a single confined bubble

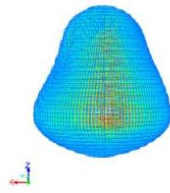
As illustrated in Fig. 5.1, the simulation domain is a 5mm long cylinder with a diameter of 1.24mm. A constant heat flux is provided through the wall and a constant liquid R134a flux is injected into the inlet. The system operating pressure is 7.06bar. Since the channel is very small, we chose a very small time step – 10^{-5} – to ensure the courant number Co is always smaller than one. At the beginning, a spherical gas bubble is initialized with a volume of $0.636 \times 10^{-9} \text{ m}^3$. This value is chosen so that the bubble will be confined by the channel wall. The details of the boundary and initial conditions are listed in Table 5.1.

Table 5.1 Simulation parameters for a single confined bubble

Length mm	Diameter mm	Heat flux kW/m^2	Inlet temperature K	Pressure bar	Time step s	Residence tolerance	Initial volume m^3	Inlet velocity m/s
5	0.64	15- 102	299	7	10^{-5}	10^{-7}	0.636×10^{-9}	0.1

5.1.1 Comparison with experimental visualization

A comparison with an experimental visualization is shown in Fig. 5.3 with the same boundary conditions. Due to the inertia force, the bubble's head is smoother and smaller than its tail. The convex shape of the tail is a result of surface tension domination.



Simulation



Experiment

5.3 Simulated bubble shape compared with experimental visualization $q=55\text{kW/m}^2$,

We initialize a cylindrical and a spherical bubble at the beginning with the same volume. The final shapes of the bubbles is illustrated in Fig. 5.4. As this figure shows, both bubbles have evolved to the same shape which is also in accordance with the experimental visualization. As they move up along the channel, both of them change shape with time due to the forces (gravity, inertia and surface tension) exerted on them. The cylindrical bubble will become spherical at the bottom as a result of surface tension, while the spherical bubble will be elongated by the inertia force along the flow direction. After a very short time (less than 3ms) they will become more or less bullet-shaped due to the balance of forces.

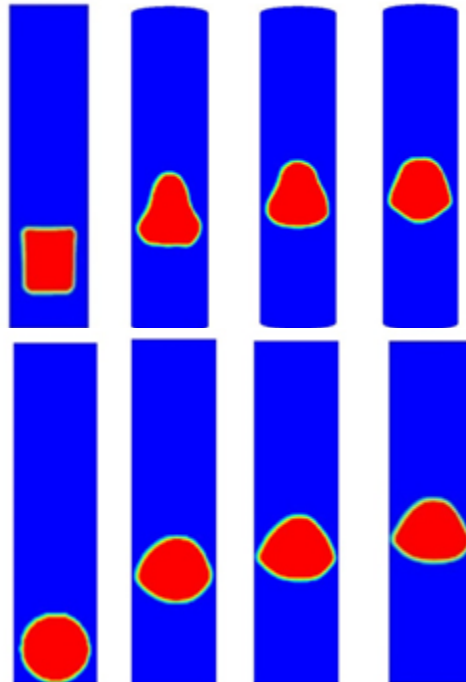


Fig. 5.4. Bubble shape with: cylindrical initial shape (top); spherical initial shape (down). Heat flux is 55kW/m^2 , inlet velocity is 0.1m/s .

5.1.2 Effect of contact angle

The surface tension plays a key role in micro channels. One of its most significant effects on bubble dynamics is at the contact region where three phases interact with each other. Usually a contact angle is formed in this region and its value is calculated from the well-known Young's equation (Young, 1805) as follows:

$$\sigma_{sv} - \sigma_{sl} = \sigma_{lv} \cos \theta \quad (60)$$

, where σ is the surface tension and subscripts s, v and l denote solid, vapor and liquid respectively. The contact angle varies from 0 to π depending on materials of fluid and wall. Fig. 5.5. illustrates two different contact angle formations by a liquid droplet on a smooth solid surface. If the liquid is replaced by a vapor bubble then the contact angle should be replaced by $(\pi - \theta)$.

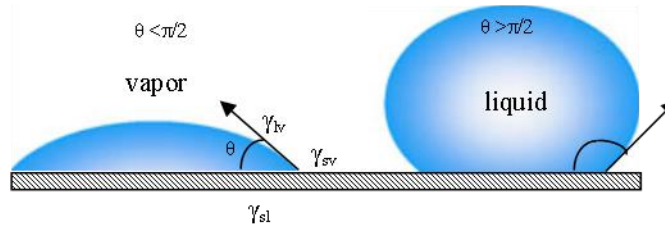


Fig. 5.5. Contact angles formed by liquid drops on a smooth homogeneous solid surface

In micro channel flow boiling, the contact angle can range from a few degrees to as large as $\pi/2$. The dominating factors are fluid material, wall material, temperature and even wall roughness. In this section three contact angle values (i.e. 8, 20, and 40°) are evaluated. As Fig. 5.6 shows, the bubble with the larger contact angle is more round. The bubble with a contact angle of 40° expands so widely in a radial direction that it reaches the channel's wall. This direct contact with the wall usually leads to a significant increase in wall temperature, and a drop in heat transfer coefficient. The bubbles with contact angles of 20 and 8° appear longer and do not have this problem. However, the bubble with a small contact angle (8°) has a thicker liquid layer than the one with a relatively larger contact angle (20°). This thick layer usually leads to higher thermal resistance and thus should be avoided in cooling applications.

40°C 20°C 8°C

Fig. 5.6. Effect of contact angle. Inlet velocity $v = 0.1 \text{ m/s}$, $q = 55 \text{ kw/m}^2$

5.1.3 Effect of inlet velocity

Inlet velocity also plays an important role in bubble dynamics. As the inlet velocity increases, the inertia force increases too, which makes the bubble more elongated. Conversely, a decreasing inlet velocity makes the bubble expand in the radial direction. It may thereby make the liquid film thinner and enhance the heat transfer. Fig. 5.7 shows different bubble shapes with inlet velocity increases from 0.1 to 0.3 m/s.

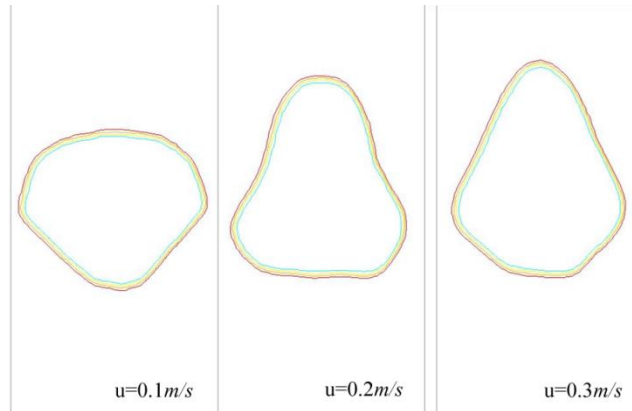


Fig. 5.7 Bubble shape with different inlet velocity $v = 0.1 \text{ m/s}$, $q = 55 \text{ kw/m}^2$

5.2 Multi confined bubbles moving in micro channels

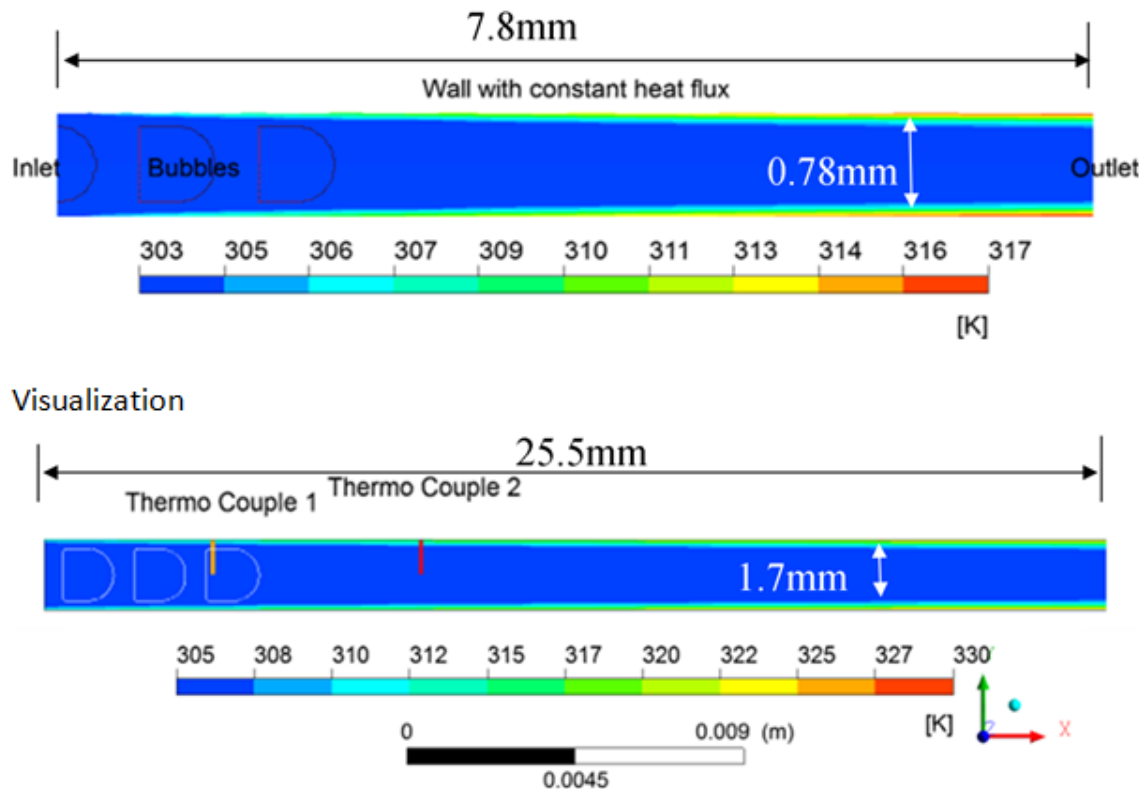
When confined bubbles move sequentially in the channel, it is believed that not only are they affected by the channel wall and fluid, they also affect each other. Details of the interaction of bubbles in isothermal flow study can be found in literature. Wijngaarden & Jeffrey (1976) calculated the velocities of identical bubbles in a bubble cloud and proposed a new method for the calculation. Batchelor & Green (1972) has given a theoretical analysis of two rigid spheres in immersed fluid and has found a relationship between the relative velocity and bubble separating distance. Ruzicka (2000, 2005) modelled a bubble chain rising in line at low Reynolds numbers (20-300). Typical phenomena in bubble interactions such as merging, separating, pairing-off, re-pairing, and oscillation were observed. Bubble interactions in flow boiling have been studied less. Magnini (M. Magnini et al., 2013b) investigated the influence of a leading bubble on its trailing bubble. Studies of the interactions between more than two bubbles in flow boiling have not been reported in the literature. In this section the phenomenon of multi bubble interactions is investigated numerically.

5.2.1 Boundary and initial parameters

As sketched in Fig. 5.8, a 7.8mm long channel with a diameter of 0.78mm is set up for visualization validation, and a 25.5mm long channel with a diameter of 1.77mm is set up for heat transfer study. An axisymmetric boundary condition is applied at the central line of the tube. The micro channel is vertical oriented which means the gravity vector pointing in $-x$ direction. A constant heat flux boundary condition (14 kw/m^2) is set for the wall. Non-slip velocity boundary conditions are chosen for momentum equation. Since the Reynolds numbers of all cases are smaller than 2100, a laminar solver is chosen. The inlet and the outlet are set to be the velocity inlet and the pressure outlet respectively.

A steady single-phase simulation with the above boundary conditions is performed and the result is used as the initial conditions for the multiphase simulation. Two bubbles consisting of a half spherical head (diameter 0.6mm for 0.78mm tube and diameter 1.4mm for 1.7mm) and cylindrical body (the same diameter as the head, and length 0.3mm for both tubes) are placed close to the inlet. For the visualization case, a third bubble with only a round head is placed

exactly at the inlet, and for the heat transfer case, the third bubble is placed with both a round head and a cylindrical body. The body with the same diameter and volume as its previous counterpart would be entering the channel during the simulation as a period inlet volume fraction condition has been set for it. Finally, the fourth bubble is placed and enters the channel manually after a certain time. The model of Plesset and Zwick is used to predicate the bubble generation and growth – or the bubble frequency if we assume the bubbles detach from the wall at $r = d/2$ and do not coalesce.



Heat transfer

Fig. 5.8. Sketch of two micro channels with different diameters (0.78 and 1.7mm). Three bubbles are initialized, and the cross section plane temperature profile is illustrated as a contour.

5.2.2 A comparison with a visualization

As shown by Fig. 5.9, a visualization of multi bubble flow in a micro channel with diameter of 0.78mm is compared to the simulation result and the movement of the bubbles is predicted well by the simulation. While the trailing three bubbles do not change too much, the leading bubble has grown significantly after about 4ms.

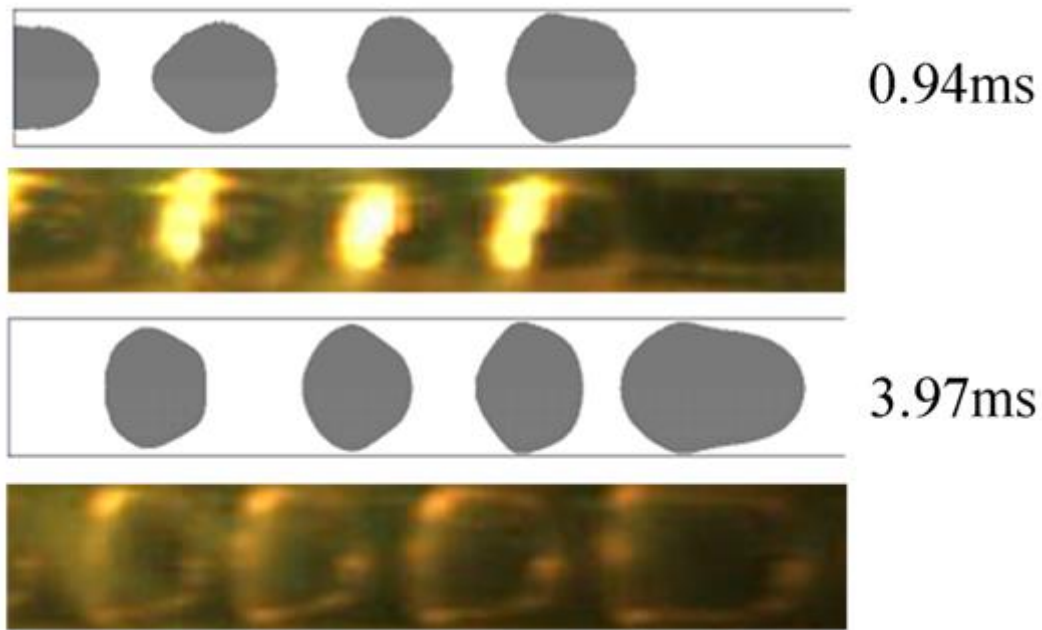


Fig. 5.9. Bubbles' movement compares to experiment visualization, $d=0.78\text{mm}$, heat flux= 14kw/m^2 , pressure= 7.06bar

5.2.3 Bubbles' dynamics

Bubbles' dynamics without heat transfer have been studied extensively. According to Taylor's law, the bubble velocities are a function of the capillary number. Evaporating bubbles moving in micro channel boiling have only been reported very recently, and bubble chain during convective boiling in small channels has not been reported to the author's knowledge.

Three cases with different bubble numbers (2, 3, and 4) are studied. Since the bubbles are growing, two bubble velocities – nose and tail – are defined. The tail velocities reflect the bubble movement and tail deformation, and the nose velocities reflect the bubble movement as well as the bubbles' growth. Comparing all tail velocities to the well-known Bretherton's correlation (Fig. 5.11), all data points fall within a range of $\pm 20\%$. This variation is partly caused by the deformation of the tail, which is further a consequence of bubble interaction.

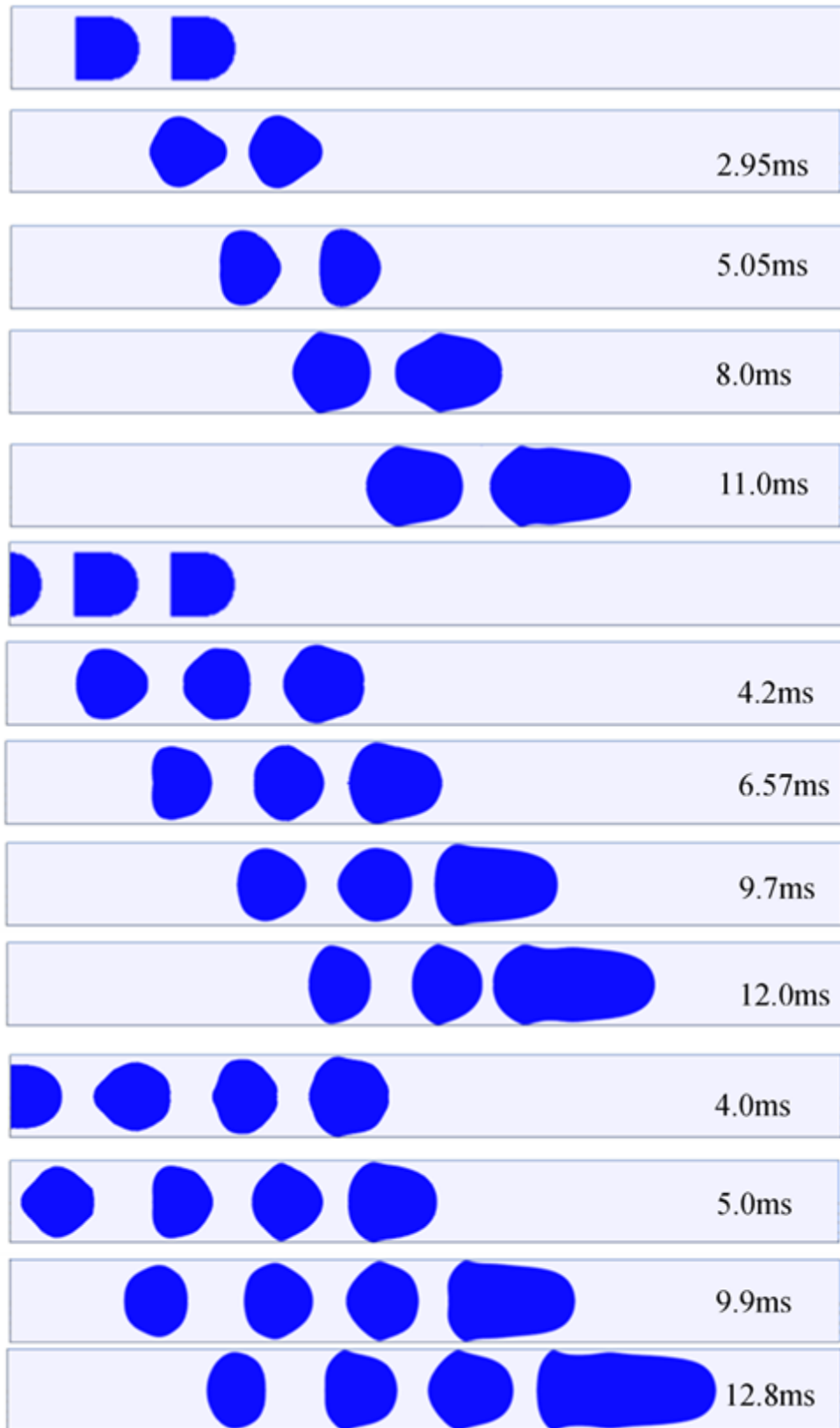


Fig. 5.10. Bubbles' movement in a micro channel. $D=0.78\text{mm}$, heat flux= 14kw/m^2 .

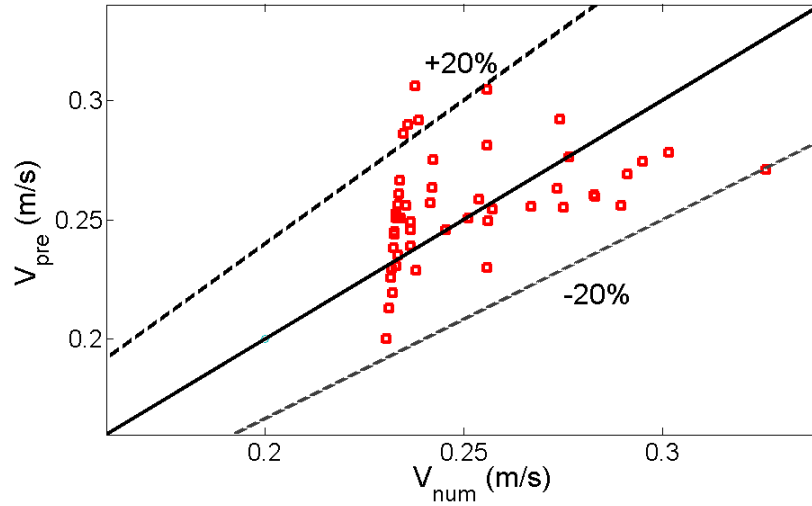


Fig. 5.11. Bubbles' tail velocities in a micro channel with diameter $D=0.78\text{mm}$, heat flux= 14kw/m^2 .

5.2.4 Heat transfer

The volume of the bubbles is illustrated in Fig. 5.12. The solid lines denote the leading bubble, the dots and triangles denote middle bubbles, and the dashed lines denote trailing bubbles. Red color represents the two-bubble case, green represents the three-bubble case, and blue represents the four-bubble case. The leading bubble's growth rate is the highest when comparing middle and trailing bubbles in all three cases and their growth rate converges with each other. The middle bubbles grow indifferently in the three-bubble and four-bubble cases. However, the trailing bubble grows faster in the two-bubble case. This is because in the two-bubble case, the trailing bubble is moving slower than its counterpart in the three-bubble and four-bubble cases due to a lack of an expansion force behind it. This means that the thermal boundary layer in front of it has more time to recover, thus leading to a higher superheat degree.

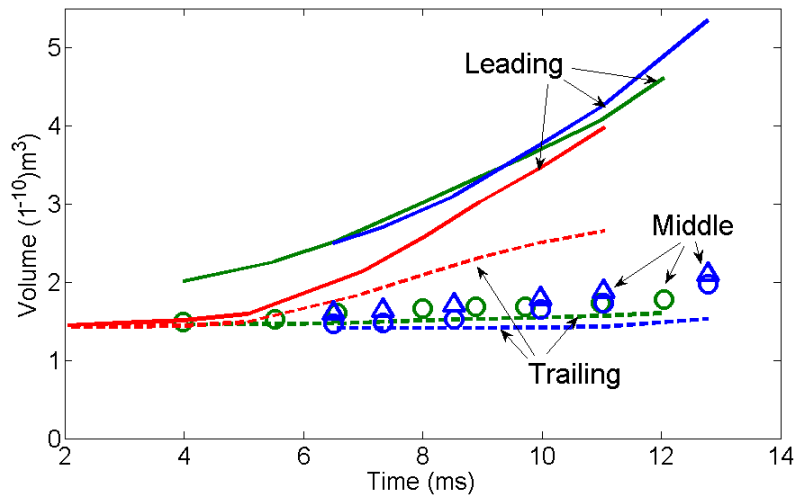


Fig. 5.12. Bubbles' volume in a micro channel. $D=0.78\text{mm}$, heat flux= 14kw/m^2 .

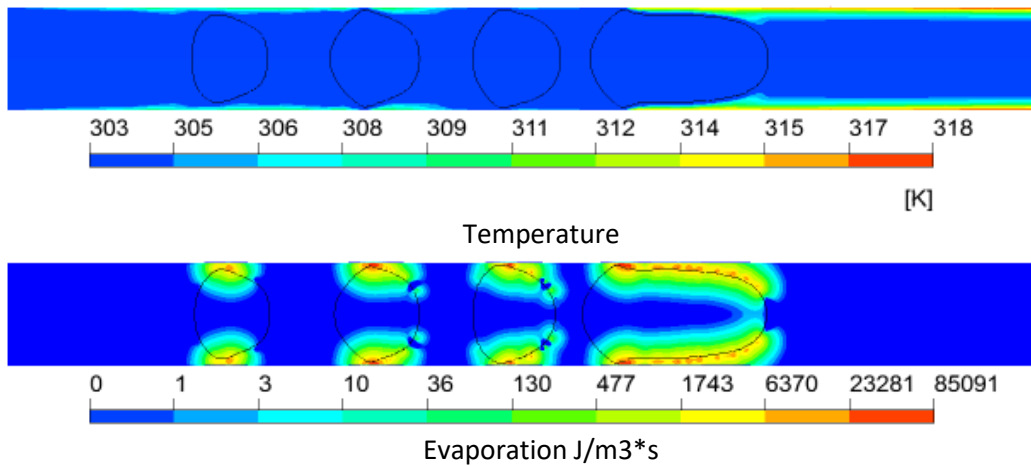


Fig. 5.13. Bubbles' temperature and diffused evaporation profile at time 11ms. $D=0.78\text{mm}$, heat flux= 14kw/m^2 .

The first bubble also has a greater contact area with the super-heated thermal boundary layer, which leads to a higher total evaporation rate.

Since the thermal boundary layer has been “ironed out” by the leading bubble, the local heat transfer coefficient of the region behind it increases dramatically when it passes by. As Fig. 5.14 indicates, a thermocouple (thermocouple 2) is placed 6mm from the inlet to measure the temperature of the wall at this point. The result shows that it significantly decreases after the leading bubble has passed, and the temperature at this time is very close to that of experimental measuring results.

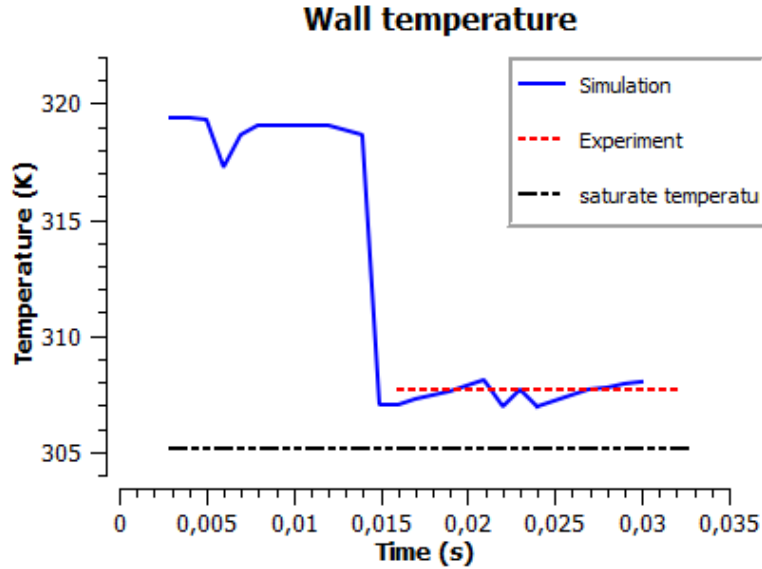


Fig. 5.14. Wall temperature measured by thermocouple 2 at 6mm from the inlet (Owhaib 2010). $D=1.7\text{mm}$, heat flux= 10kw/m^2 , pressure =7.06bar.

Summary

An axisymmetric numerical model is established to study multi bubbles moving consecutively in convective boiling in micro channels. Visualization and heat transfer comparison are carried out with existing experiment results and good agreement is observed. Two cases with different channel diameter and wall heat flux are investigated. Based on the results, several conclusions can be drawn, as follows:

- 1 Bubbles have different growth rates during the moving process. The first bubble, coming into contact with the warmest liquid at boundary layer, has the highest growth rate.
- 2 All bubbles' evaporation rates increase as they move up the channel where the liquid temperature is higher. After a certain time, all this evaporation density exceeds the input heat density.
- 3 The wall temperature drops significantly when bubbles pass by but will recovery slowly afterwards.

6 Slug to annular flow transition

Slug is one of the characteristic flow regimes in micro channel flow boiling. It originates from the confined bubbly flow and evolves into annular flow, which is also common in macro size channels and represents a major part of the flow in terms of length. It usually occupies more than 60% of a micro channel depending on operating conditions. The transition between these two regimes plays a key role in both the heat transfer and flow dynamics. This chapter is based on the author's published journal paper: "A numerical study on the transition from slug to annular flow in micro-channel convective boiling" (Liu et al., 2017b).

6.1 Initial and boundary conditions

The simulation set-up is in accordance with a published experiment (Tibirica & Ribatski, 2014). Specifically, a channel with a diameter of 0.4mm and a length of 6mm is heated with a constant heat flux. One validation case and eight studying cases are set up according to certain initial and boundary conditions as listed in Table 6.1. A sketch of the simulation domain is illustrated in Fig. 6.1. Gravity is neglected so that an axisymmetric boundary condition is applied at the center of the channel to reduce computational load and a high degree of accuracy is maintained. At first (0ms), the whole channel is filled with liquid R245fa at saturated temperature (304.15K). Then saturated liquid R245fa starts entering the inlet with a mass flux of $400\text{kg}/(\text{m}^2\cdot\text{s})$ and the wall is heated with a constant heat flux at the same time. After $(t_0-0.3)\text{ms}$, the temperature and velocity profile have nearly been developed (Fig. 6.2) and a bubble and an annulus are initialized in the channel (Fig. 6.1) according to different parameters listed in Table 6.1. A two-phase simulation for 0.3ms then starts in order to obtain a smooth surface of the bubble and annulus.

Table 6.1. Initial and boundary conditions for slug to annular transient flow

Parameters	Test	Transition flow				Single bubble flow			
		Case 1	Case 2	Case 3	Case 4	Case 5	Case 6	Case 7	Case 8
Bubble length <i>mm</i>	0.8	1.0	1.0	0.8	1.0	1.0	1.0	0.8	1.0
Bubble diameter	0.185	0.185	0.185	0.185	0.185	0.185	0.185	0.185	0.185
Separating distance <i>mm</i>	0.12	0.15	0.15	0.15	0.15	0.15	0.15	0.15	0.15
A second bubble	Yes	No	No	No	No	No	No	No	No
Annulus length	2.0	2.0	2.0	2.0	2.0	N/A	N/A	N/A	N/A
Neck length <i>mm</i>	0.8	0.8	0.8	0.8	0.8	N/A	N/A	N/A	N/A
Heat flux <i>kw/m²</i>	180	160	80	160	160	160	80	160	160
Ca	0.008	0.008	0.008	0.008	0.004	0.008	0.008	0.008	0.004



Fig. 6.1. Sketch of the micro channel, bubble and annulus placement.

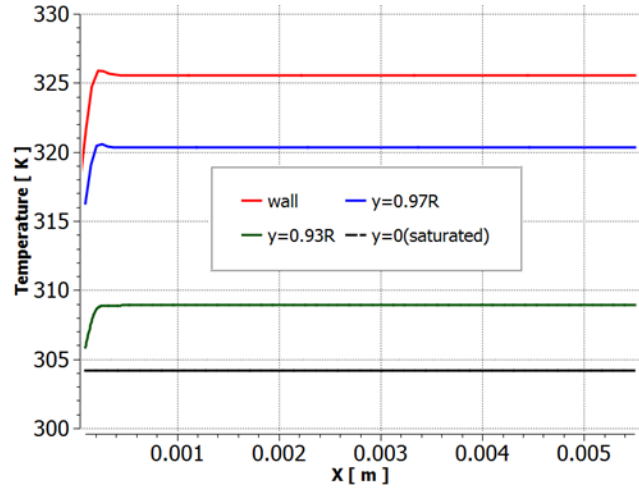


Fig. 6.2. Wall and film temperature at time $t_0-0.3\text{ms}$ for $q=160\text{ kw/m}^2$

6.2 A validating case

Fig. 6.3 illustrates a comparison with the experimental visualization (Tibirica & Ribatski, 2014). When the bubble grows (0.4ms), it pushes the liquid ahead and makes notches in the tail of the annulus, which are marked by dark arrows in the experimental snapshots. After a short time (0.6ms), the notches become concave while the head of the bubble is pushed back and becomes almost flat. After 0.8ms, the expanding force pulls the bubble head to coalescence with the annulus tail. Two small droplets are produced at the merging region when the bubble and the annulus coalesce. Fig. 6.4 presents a comparison of the bubble length between the experiment and our numerical simulation.

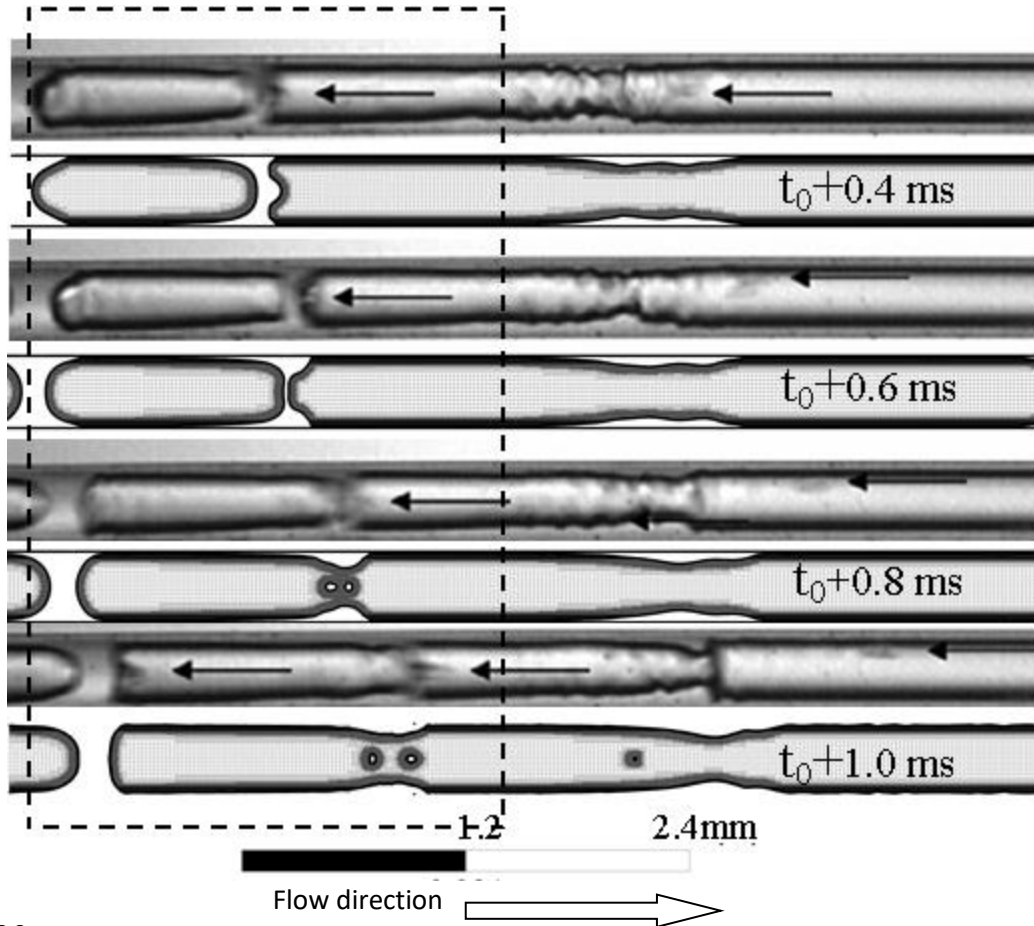


Fig. 6.3.
Bubble shapes compared with an experiment (Tibirica & Ribatski, 2014). The time span between two consecutive pictures is 0.2 ms. $q=180 \text{ kw/m}^2$, $G=400 \text{ kg/m}^2\text{s}$, $D=0.4 \text{ mm}$, $T_{\text{sat}}= 304.15 \text{ K}$

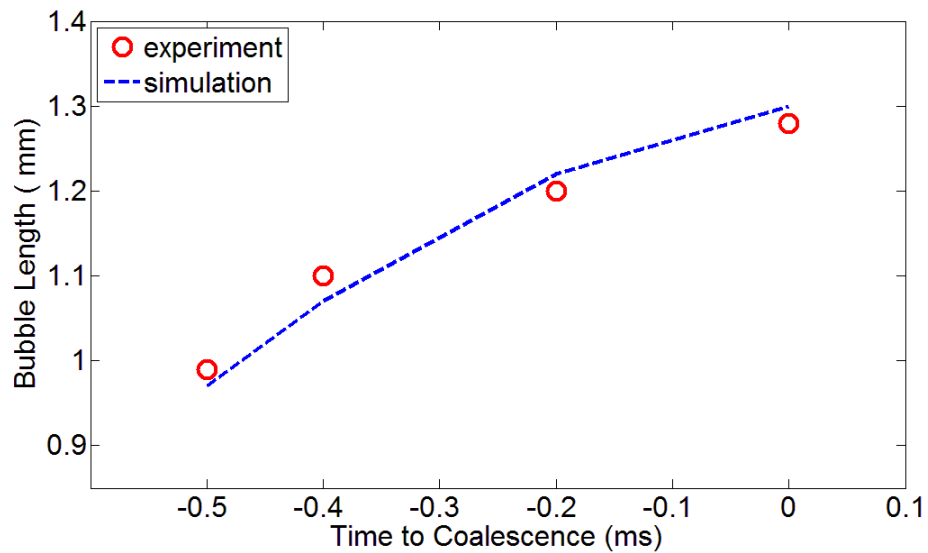


Fig. 6.4. Bubble length vs time. $q=180 \text{ kw/m}^2$, $G=400 \text{ kg/m}^2\text{s}$, $D=0.4 \text{ mm}$, $T_{\text{sat}}= 304.15 \text{ K}$

6.3 Flow regime transition

In this section, four single bubbly flow cases and four transition flow cases are compared. The wall heat flux is $q=160 \text{ kw/m}^2$, the separating distance between the bubble and the annulus is 0.15mm , and there is no second bubble presented at the inlet of the channel. The differences are listed in Table 6.1 and the control parameters are highlighted in green.

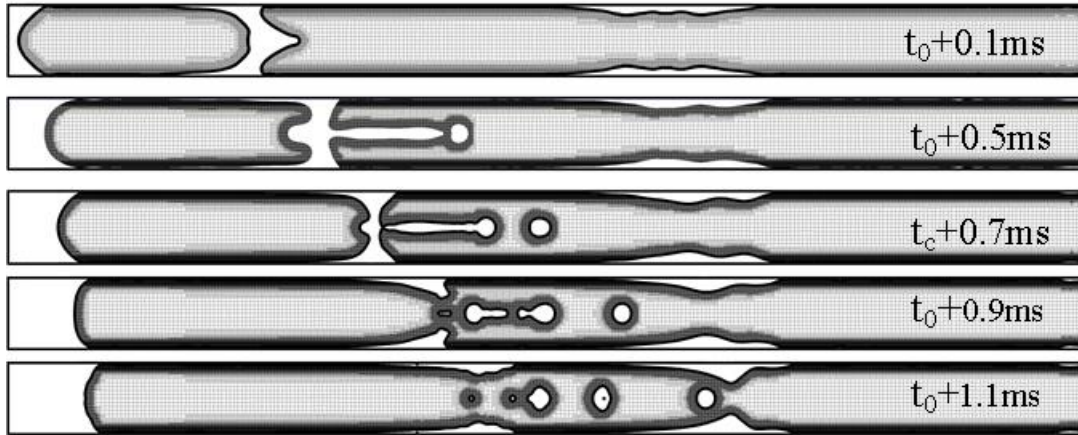


Fig. 6.5. Flow regime transition. $q=160 \text{ kw/m}^2$, $G=400 \text{ kg/m}^2$, $Ca=0.008$, $T_{sat}= 304.15\text{K}$

Fig. 6.5 illustrates how the bubble and the annulus coalesce. In comparison with the validation case, the annulus deformation is much more severe in this case due to higher evaporation, i.e. a much deeper notch is made in the end of the annulus. In addition, four small droplets are produced by the coalescence.

Fig. 6.6 compares the bubble shape 0.1ms before the coalescence in transition to that in the flow of single bubble. It indicates that the bubble in the transition flow is longer than the one in the single bubbly flow.

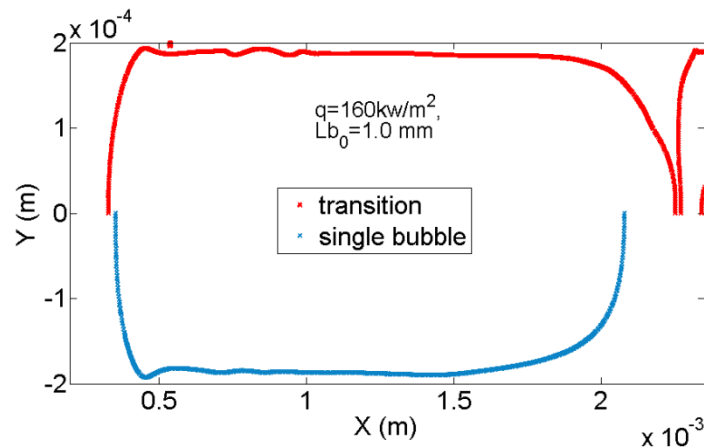


Fig. 6.6. Bubble shapes 0.1ms before coalescence ($t_0+0.8\text{ms}$). $G=400 \text{ kg/m}^2$, $Ca=0.008$, $T_{sat}= 304.15 \text{ K}$

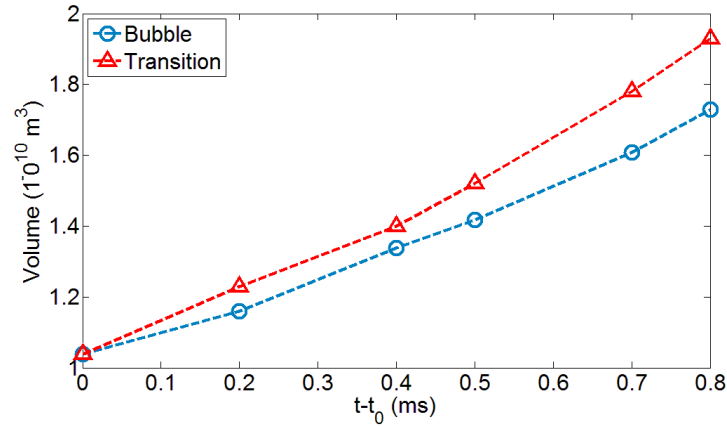


Fig. 6.7. Bubble volume versus time. $q=160 \text{ kw/m}^2$, $G=400 \text{ kg/m}^2$, $Ca=0.008$, $T_{\text{sat}}= 304.15 \text{ K}$

This contradicts the idea that the resistance of the leading annulus would make the trailing bubble shorter. A likely explanation would be that the evaporating force is so strong that it overcomes this resistance. This hypothesis is confirmed by the fact that the volume of the bubble in transition flow is also larger (Fig. 6.7).

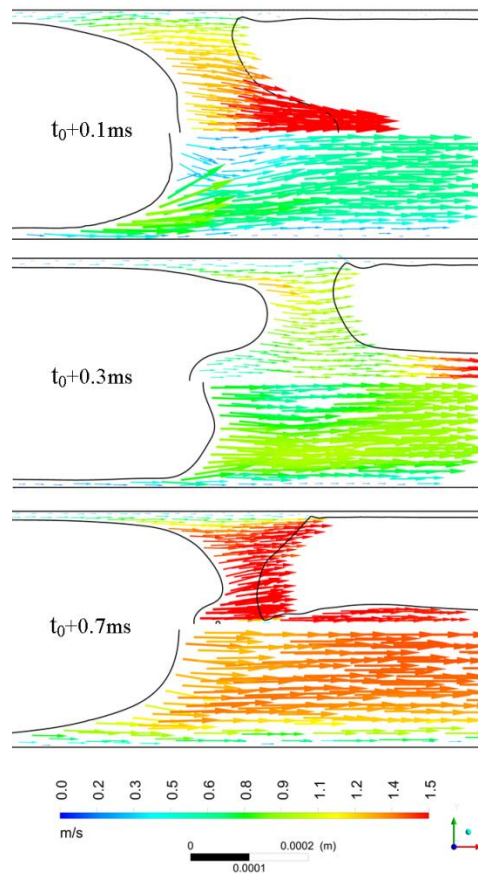


Fig. 6.8. Velocity field of the liquid slug. $q=160 \text{ kw/m}^2$, $G=400 \text{ kg/m}^2$, $Ca=0.008$, $T_{\text{sat}}= 304.15 \text{ K}$

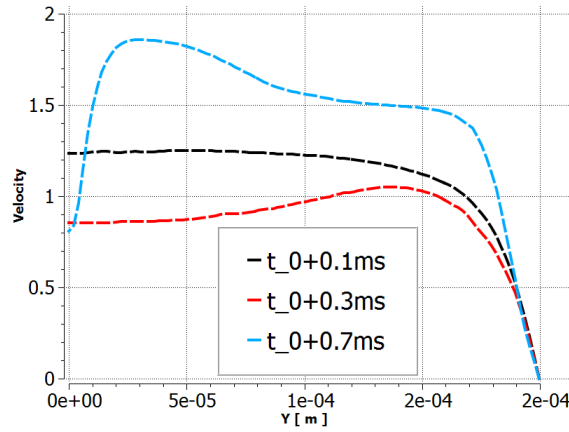


Fig. 6.9. Velocity 0.1mm in front of the bubble in the transition flow. $q=160 \text{ kw/m}^2$, $G=400 \text{ kg/m}^2$, $Ca=0.008$, $T_{sat}= 304.15 \text{ K}$

As can be seen in Fig. 6.8, the velocity field of the liquid slug between the bubble and the annulus is different in the transition flow than in front of the bubble in the single bubbly flow. In the transition flow, the bubble expansion is very strong at the beginning ($t_0+0.1\text{ms}$) so that the velocity in front of it is high (Fig. 6.9). In the next phase, this velocity (especially in the middle of the tube) decreases slightly ($t_0+0.3\text{ms}$). This is probably because the evaporation rate is slightly lower at this time. Before the coalescence ($t_0+0.7\text{ms}$), it increases again. In the single bubbly flow, however, this velocity is a monotonic function of time. The reason is that the presence of the annulus makes the expansion pulse. The reason for this phenomenon lies in the force balance between the evaporating momentum and the surface tension of the annulus tail. The evaporating momentum force pushes the liquid slug forward and the surface tension prevents it. The former force depends on the super-heated thermal boundary layer, which is not steady state, and the surface tension depends on local interface curvature, which is also not constant. At the beginning ($t_0+0.1\text{ms}$), the evaporating momentum force is large and the surface tension is relatively small, thus the forward velocity vector is large. In the next phase ($t_0+0.3\text{ms}$), the evaporating momentum decreases slightly or remains constant, but the surface tension forces increase (the local curvature of interface increases). Adding on the increase of liquid mass, the liquid slug has been slowed down.

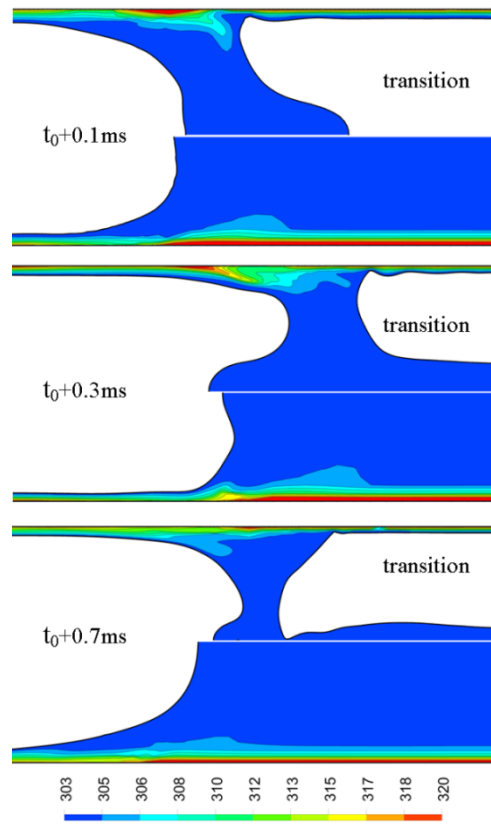


Fig. 6.10. Temperature field of the liquid slug. $q=160 \text{ kw/m}^2$, $G=400 \text{ kg/m}^2$, $Ca=0.008$, $T_{\text{sat}}= 304.15 \text{ K}$

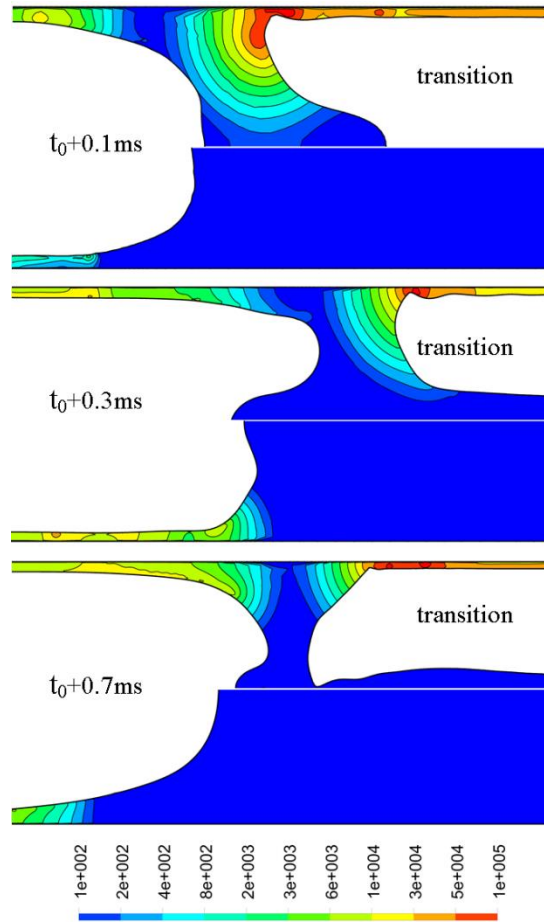


Fig. 6.11. Evaporation rate ($\text{kg/m}^3\cdot\text{s}$) contour of the liquid slug. $q=160 \text{ kw/m}^2$. $G=400 \text{ kg/m}^2$, $Ca=0.008$, $T_{\text{sat}}= 304.15 \text{ K}$

The thermal boundary layer in both the transition flow and the single bubbly flow is disturbed by the movement of the bubble. As Fig. 6.10 illustrates, there is no significant difference at the beginning. However, after a short time (0.3ms), the longer front of the bubble in the transition flow makes the thermal boundary layer more “turbulent”.

Most of the evaporation takes place in the thin liquid film. As Fig. 6.11 shows, the highest evaporation is at the rear of the annulus. In the bubble part, the evaporation rate in the transition flow is higher at the beginning ($t_0+0.1\text{ms}$). This difference makes the bubble in the transition flow expand faster and the velocity in front of it higher (as mentioned in the velocity field analysis). Nevertheless, this difference disappears after a short time ($t_0+0.3\text{ms}$), and appears again before the coalescence ($t_0+0.7\text{ms}$).

6.3.1 Effect of heat flux

The wall heat flux is believed to play a dominant role in micro channel flow boiling. A micro channel with a lower wall heat flux of 80kw/m^2 is studied in order to examine the heat flux influence. It is found (Fig. 6.12) that – not surprisingly – the bubble grows slower and the coalescence process is less intense than with a higher wall heat flux of 160kw/m^2 .

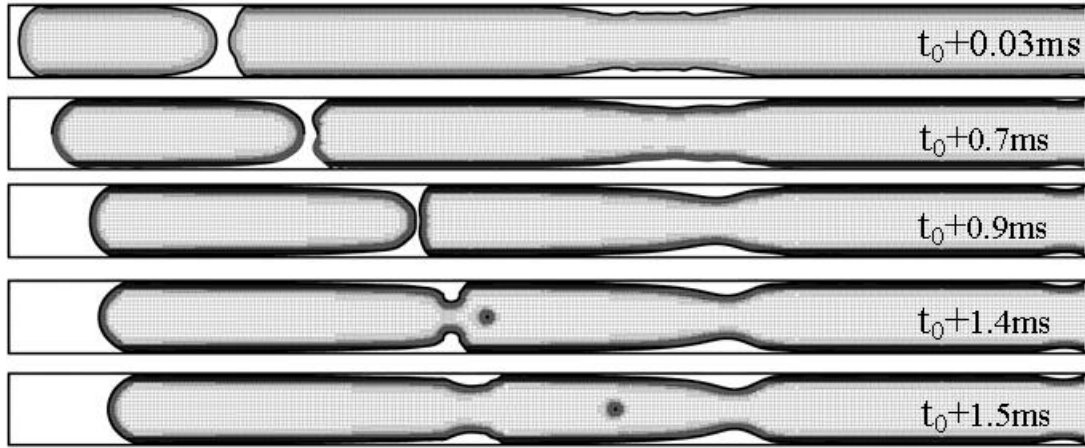


Fig. 6.12. Flow regime transition with lower heat flux. $G=400 \text{ kg/m}^2$, $Ca=0.008$, $L_{b0}=1.6 \text{ mm}$, $T_{sat}= 304.15 \text{ K}$

It is found (Fig. 6.13) that under this heat flux, the bubbles in both the transition flow and the single bubble flow grow almost identically.

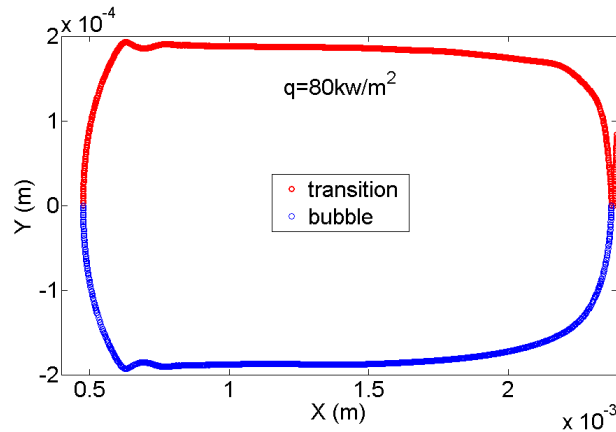


Fig. 6.13. Bubble shapes before coalescence. $G=400 \text{ kg/m}^2$, $Ca=0.008$, $L_{b0}=1.0 \text{ mm}$, $T_{sat}= 304.15 \text{ K}$

6.3.2 Effect of initial bubble length

The initial bubble length is also of interest in our study. As we all know, most of the evaporation takes place in the thin film region, and the area of this region is proportional to the bubble length. In order to study this effect, a shorter initial bubble length is examined: i.e. 1.2mm. The study has found a milder coalescence (Fig. 6.14). A notch is made by the bubble expansion, although the length is shorter. Only two droplets are produced by the coalescence. The coalescence time is, surprisingly, almost the same.

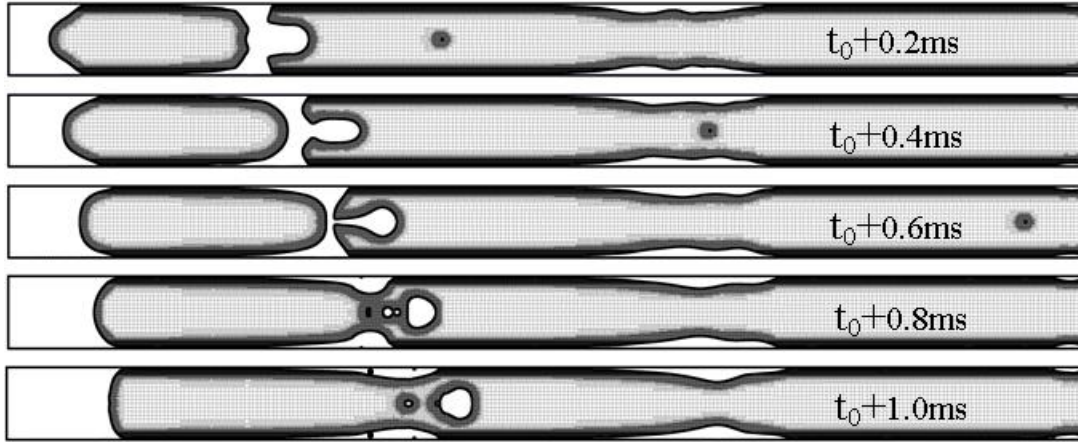


Fig. 6.14. Flow regime transition with shorter initial bubble length. $q=160 \text{ kw/m}^2$, $G=400 \text{ kg/m}^2$, $Ca=0.008$, $T_{sat}= 304.15 \text{ K}$

It is also surprising to find that the bubble in the transition flow is actually slightly shorter than the one in the single bubbly flow just before the coalescence (Fig. 6.15).

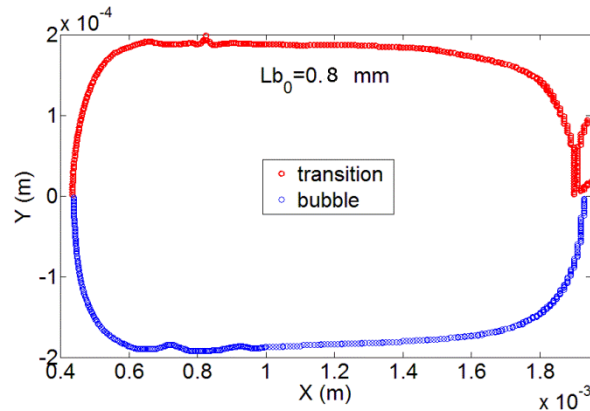


Fig. 6.15. Bubble shapes before coalescences. $q=160 \text{ kw/m}^2$, $G=400 \text{ kg/m}^2$, $Ca=0.008$, $T_{sat}= 304.15 \text{ K}$

6.3.3 Effect of surface tension

Surface tension force becomes significant when characteristic length goes down. In micro-scale phenomena it is usually a dominant factor for dynamics and heat transfer. The capillary number is a widely used dimensionless number for measuring the ratio between viscous force and surface tension. Two cases with capillary numbers 0.008 and 0.004 are examined here. In Fig. 6.16 it is shown that the higher surface tension (lower Ca) leads to a less severe transition. An interesting finding is that two droplets are produced even before the coalescence at time $t_0+0.6\text{ms}$.

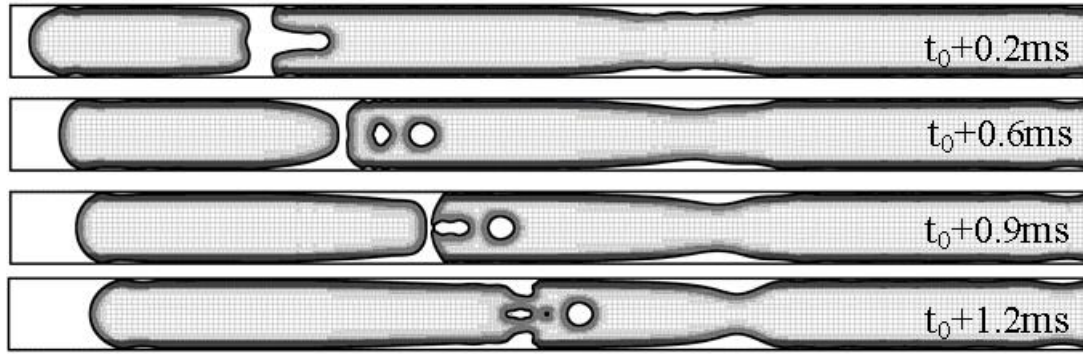


Fig. 6.16. Flow regime transition with higher surface tension. $q=160 \text{ kw/m}^2$, $G=400 \text{ kg/m}^2$, $L_{b0}=1.2 \text{ mm}$, $T_{\text{sat}}= 304.15 \text{ K}$

A comparison of bubble shapes before the coalescence is shown in Fig. 6.17. The two bubbles are almost the same length but with slightly different shapes at the front: i.e. the one in transition has a more flat head.

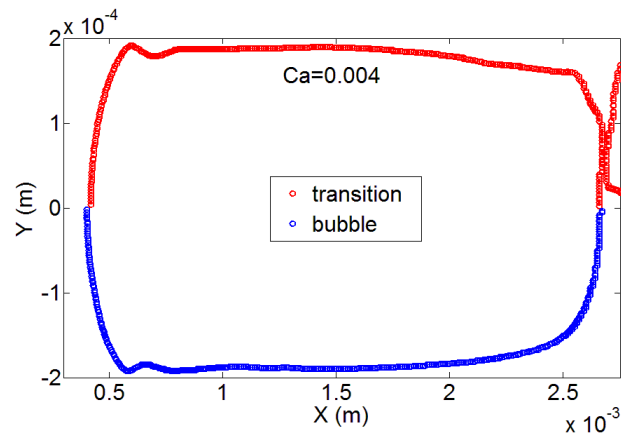


Fig. 6.17. Bubble shapes before coalescence. $q=160 \text{ kw/m}^2$, $G=400 \text{ kg/m}^2$, $L_{b0}=1.0 \text{ mm}$, $T_{\text{sat}}= 304.15 \text{ K}$

6.4 Summary

A numerical study of the transition from slug flow (elongated bubble flow) to annular flow in a micro channel with a diameter of 0.4 mm is conducted. The coupled level set and volume of fluid (CLSVOF) method and a non-equilibrium phase change model are applied to capture the two-phase interface and to calculate evaporation respectively. A new simple pre-calculation for the initialization is proposed to reduce computational load. The transition process is predicted well and is validated against a published experimental visualization. The flow regime transition and bubble growth are predicted well by the simulation. It is found that the expansion of the bubble will make a notch at the end of the annulus. This notch will contract and produces small droplets when the bubble and the annulus coalesce. The number of droplets produced depends on the initial bubble length, the wall heat flux and the surface tension (denoted by capillary number). The liquid slug between the bubble and the annulus is strongly influenced by the flow pattern transition. While the slug velocity in the transition process has a pulsing characteristic, it

is a monotonic function of time in the single bubbly flow. This dynamic characteristic leads to a deformation of both the bubble head and the annulus tail in the transition flow. When the bubble is long, the heat flux is high and the capillary number is low, the deformation is so strong that the bubble head is split into two parts by a large notch. These two parts can even reach the thermal boundary layer. The evaporation is thereby significantly enhanced in this deformed head region.

7 Conclusions

The present thesis develops and validates a novel numerical model by combining the coupled level set and VOF method with a non-equilibrium phase change model. Both models have been developed previously but the combination of these two methods is new, which yields accurate simulation results proven by validating against theoretical analysis and published experimental data. The classical one-dimensional Stefan problem and Scriven's kinetic theory are used as benchmarks for the phase change model validation. The surface tension model is validated by the well-known lubrication theory, and the coalescence is validated by an experimental visualization. All validations have achieved good agreement between simulation and validating benchmarks.

New phenomena including two flow regime transitions (i.e. isolated bubbles to confined bubbly flow, and slug to annular flow) and one single flow regime (multiple confined bubbly flow) are investigated. These new phenomena and studies reveal the transition mechanisms. In the first transition, the bubble coalescence is found to be dominant, while the evaporation is key in the second transition. A simplified symmetrical bubble coalescence model is proposed to present the first transition. The transitions are found to affect the local heat transfer significantly due to their unsteady characteristics, while the non-transition process has more stable local heat transfer coefficients.

The transition from isolated bubbly flow to confined bubbly flow can be roughly divided into three stages: sliding, merging and post-merging stages. The latter two stages are both extremely fast processes which take less than one millisecond. The dynamics and heat transfer are very different in these three stages. In the sliding stage, bubbles have relatively high growth rate but low velocity (both vertical and transverse velocities). The thermal boundary layer is highly distorted and thinned close to the bubble during this time and heat is therefore transferred with less resistance between the fluid and the channel wall. In the merging stage, the surface tension is so strong that the formation of a new bubble can occur within 1 millisecond. The expansion of the bubble along the radial direction makes the bubble protrude into the thermal boundary layer and hence enhances heat transfer temporarily. During this stage the bubble has a relatively moderate growth rate. Both the mass flux and the heat flux affect the bubble's growth and merging. A lower mass flux or a higher wall heat flux leads to a higher bubble growth rate and mostly an earlier merging under low Reynolds numbers. The bubbles will merge with each other during saturated boiling after departing from the wall. Conversely, the merge does not even occur under the sub-cooled condition due to a much lower bubble growth.

In the confined bubbly flow, a train of bubbles enters a channel filled with liquid which is superheated along the walls. Bubbles have different growth rates during the moving process. The first bubble, coming into contact with the warmest liquid at the boundary layer, has the highest growth rate. In addition, all bubbles' evaporation increases as they move up the channel where the liquid temperature is higher. After a certain time, all this evaporation heat exceeds the input heat flux due to the heat absorbed from the super-heated liquid around the bubbles.

The wall temperature drops significantly when bubbles pass by but will recovery slowly afterwards.

In the transition from slug to annular flow, the local wall heat transfer coefficient is increased by the coalescence of the annulus and the bubble. It is found that the expansion of the bubble will make a notch at the end of the annulus. The notch then contracts and produces small droplets when the bubble and the annulus coalesce. The number of droplets produced depends on the initial bubble length, the wall heat flux and the surface tension (represented by the capillary number). While the slug velocity in the transition process has a pulsing characteristic, it is a monotonic function of time in the single bubbly flow. This dynamic characteristic leads to a deformation of the bubble head in the transition flow. When the bubble is long, the heat flux is high and the capillary number is low (Fig. 6.5), the deformation is so strong that the annulus tail is split into two parts by a large notch. These two parts can even reach the thermal boundary layer. The evaporation is thereby significantly enhanced in this deformed head region.

7.2 Future plans and suggestions

Despite the research efforts made in this dissertation, a few challenges remain unsolved or the solutions can be improved. One of the most important challenges in electronic cooling is the conjugate heat transfer where the wall is also included. In this case, three phases – solid, liquid, and vapor – coexist, which makes coupling very difficult with existing models. Developing new models to address the problem is an urgent challenge. In addition, the level set function re-initialization equation is discretized by the MUSCL scheme. This scheme is not perfect compared to the weighted essential non-oscillation (WENO) scheme. A high order WENO scheme (3rd or 5th) is preferred when the interface is more distorted.

Nomenclature

Latin letters

A	area
C	coefficient
c	specific heat
Ca	capillary number
Co	courant number
D	diameter
Eo	Eotvos number
F	force
G	mass flux
H	enthalpy
k	thermal conductivity
\mathbf{k}	curvature
\mathbf{n}	normal vector
n	time step
L	length
Mo	Morton number
P	pressure
Pr	Prandtl number
q	heat flux
R_{int}	thermal resistance
Rg	gas constant
Re	Reynolds number
T	temperature
\mathbf{U}	velocity vector
V	volume
Z	vertical distance
We	Weber number

Greek Letters

α	volume fraction
β	growth constant
δ	thickness
θ	contact angle
μ	viscosity
ρ	density
σ	surface tension
Φ	level set function

Subscripts

b	bubble
c	condensation
d	diffusion
e	evaporation

<i>f</i>	fluid
<i>i</i>	grid number
<i>g</i>	gas
<i>l</i>	liquid
<i>gr</i>	grid
<i>int</i>	interface
<i>o</i>	operating condition
<i>v</i>	vapor
<i>w</i>	wall
<i>sat</i>	saturation

References

- Agostini, B., Revellin, R., & Thome, J. R. (2008). Elongated bubbles in microchannels. Part I: Experimental study and modeling of elongated bubble velocity. *International Journal of Multiphase Flow*, 34(6), 590-601.
- Ali, R. (2010). Phase Change Phenomena During Fluid Flow in Microchannels.
- Ali, R., Palm, B., & Maqbool, M. H. (2011). Flow boiling heat transfer characteristics of a minichannel up to dryout condition. *Journal of Heat Transfer*, 133(8), 081501.
- Anderson, J. D., & Wendt, J. (1995). *Computational Fluid Dynamics* (Vol. 206): Springer.
- Ansys, Q. (2011). FLUENT Theory Guide.
- Anwar, Z., Palm, B., & Khodabandeh, R. (2015). Flow boiling heat transfer, pressure drop and dryout characteristics of R1234yf: experimental results and predictions. *Experimental Thermal and Fluid Science*, 66, 137-149.
- Aussillous, P., & Quéré, D. (2000). Quick deposition of a fluid on the wall of a tube. *Physics of Fluids (1994-present)*, 12(10), 2367-2371.
- Barber, J., Brutin, D., Sefiane, K., & Tadrist, L. (2010). Bubble confinement in flow boiling of FC-72 in a “rectangular” microchannel of high aspect ratio. *Experimental Thermal and Fluid Science*, 34(8), 1375-1388.
- Batchelor, G., & Green, J.-T. (1972). The hydrodynamic interaction of two small freely-moving spheres in a linear flow field. *Journal of Fluid Mechanics*, 56(02), 375-400.
- Bhaga, D., & Weber, M. (1980). In-line interaction of a pair of bubbles in a viscous liquid. *Chemical Engineering Science*, 35(12), 2467-2474.
- BP. (2016). BP Energy Outlook 2016 *BP Energy Outlook* (2016 ed., pp. 98): BP.
- Brackbill, J. U., Kothe, D. B., & Zemach, C. (1992). A continuum method for modeling surface tension. *Journal of Computational Physics*, 100(2), 335-354.
- Brereton, G., & Korotney, D. (1991). Coaxial and oblique coalescence of two rising bubbles. *Dynamics of bubbles and vortices near a free surface, AMD*, 119.
- Bretherton, F. (1961). The motion of long bubbles in tubes. *Journal of Fluid Mechanics*, 10(02), 166-188.
- Carey, V. P. (1992). *Liquid-Vapor Phase-Change Phenomena* (Vol. 45).
- Chen, H., Xu, J., Xie, J., Xing, F., & Li, Z. (2014). Modulated flow patterns for vertical upflow by the phase separation concept. *Experimental Thermal and Fluid Science*, 52, 297-307.
- Chen, J. C. (1966). Correlation for boiling heat transfer to saturated fluids in convective flow. *Industrial & Engineering Chemistry Process Design and Development*, 5(3), 322-329.
- Chen, T., & Chung, J. (2003). Heat-transfer effects of coalescence of bubbles from various site distributions. *Proceedings of the Royal Society of London. Series A: Mathematical, Physical and Engineering Sciences*, 459(2038), 2497-2527.
- Chen, T., & Garimella, S. V. (2006). Measurements and high-speed visualizations of flow boiling of a dielectric fluid in a silicon microchannel heat sink. *International Journal of Multiphase Flow*, 32(8), 957-971.
- Cioncolini, A., Thome, J. R., & Lombardi, C. (2009). Algebraic turbulence modeling in adiabatic gas-liquid annular two-phase flow. *International Journal of Multiphase Flow*, 35(6), 580-596.
- Consolini, L., & Thome, J. R. (2010). A heat transfer model for evaporation of coalescing bubbles in micro-channel flow. *International Journal of Heat and Fluid Flow*, 31(1), 115-125.

- Cooper, M. (1984). Heat flow rates in saturated nucleate pool boiling—a wide-ranging examination using reduced properties. *Advances in Heat Transfer*, 16, 157-239.
- Dhir, V. K., Abarajith, H. S., & Li, D. (2007). Bubble Dynamics and Heat Transfer during Pool and Flow Boiling. *Heat Transfer Engineering*, 28(7), 608-624.
- Feireisl, E., Novotný, A., & Petzeltová, H. (2001). On the existence of globally defined weak solutions to the Navier—Stokes equations. *Journal of Mathematical Fluid Mechanics*, 3(4), 358-392.
- Fershtman, A., Shemer, L., & Barnea, D. (2016). Instantaneous heat transfer rate around consecutive Taylor bubbles. *International Journal of Heat and Mass Transfer*, 95, 865-873.
- Francois, M. M., Cummins, S. J., Dendy, E. D., Kothe, D. B., Sicilian, J. M., & Williams, M. W. (2006). A balanced-force algorithm for continuous and sharp interfacial surface tension models within a volume tracking framework. *Journal of Computational Physics*, 213(1), 141-173. doi: 10.1016/j.jcp.2005.08.004
- Garimella, S. V., Persoons, T., Weibel, J., & Yeh, L.-T. (2013). Technological drivers in data centers and telecom systems: Multiscale thermal, electrical, and energy management. *Applied Energy*, 107, 66-80.
- Golobic, I., Petkovsek, J., & Kenning, D. (2012). Bubble growth and horizontal coalescence in saturated pool boiling on a titanium foil, investigated by high-speed IR thermography. *International Journal of Heat and Mass Transfer*, 55(4), 1385-1402.
- Gong, S., & Cheng, P. (2013). Lattice Boltzmann simulation of periodic bubble nucleation, growth and departure from a heated surface in pool boiling. *International Journal of Heat and Mass Transfer*, 64(0), 122-132.
- Gungor, K. E., & Winterton, R. (1986). A general correlation for flow boiling in tubes and annuli. *International Journal of Heat and Mass Transfer*, 29(3), 351-358.
- Gupta, S. C. (2003). Chapter 1 The Stefan problem and its classical formulation. In S. C. Gupta (Ed.), *North-Holland Series in Applied Mathematics and Mechanics* (Vol. Volume 45, pp. 1-38): North-Holland.
- Han, Y., Kanno, H., Ahn, Y.-J., & Shikazono, N. (2015). Measurement of liquid film thickness in micro tube annular flow. *International Journal of Multiphase Flow*, 73, 264-274.
- Han, Y., & Shikazono, N. (2009). Measurement of the liquid film thickness in micro tube slug flow. *International Journal of Heat and Fluid Flow*, 30(5), 842-853.
- Han, Y., & Shikazono, N. (2010). The effect of bubble acceleration on the liquid film thickness in micro tubes. *International Journal of Heat and Fluid Flow*, 31(4), 630-639.
- Hardt, S., & Wondra, F. (2008). Evaporation model for interfacial flows based on a continuum-field representation of the source terms. *Journal of Computational Physics*, 227(11), 5871-5895.
- Hirt, & Nichols. (81). Volume of fluid (VOF) method for the dynamics of free boundaries.
- Hsu, Y., & Graham, R. W. (1961). An analytical and experimental study of the thermal boundary layer and ebullition cycle in nucleate boiling: National Aeronautics and Space Administration. Lewis Research Center, Cleveland.
- Issa, R. I. (1986). Solution of the implicitly discretised fluid flow equations by operator-splitting. *Journal of Computational Physics*, 62(1), 40-65.
- Kandlikar, S. G. (1990). A general correlation for saturated two-phase flow boiling heat transfer inside horizontal and vertical tubes. *Journal of Heat Transfer*, 112(1), 219-228.
- Kandlikar, S. G. (2010a). Scale effects on flow boiling heat transfer in microchannels: A fundamental perspective. *International Journal of Thermal Sciences*, 49(7), 1073-1085.

- Kandlikar, S. G. (2010b). Similarities and Differences Between Flow Boiling in Microchannels and Pool Boiling. *Heat Transfer Engineering*, 31(3), 159-167.
- Kenning, D. B. R., Wen, D. S., Das, K. S., & Wilson, S. K. (2006). Confined growth of a vapour bubble in a capillary tube at initially uniform superheat: Experiments and modelling. *International Journal of Heat and Mass Transfer*, 49(23–24), 4653-4671.
- Kheirabadi, A. C., & Groulx, D. (2016). Cooling of server electronics: A design review of existing technology. *Applied Thermal Engineering*, 105, 622-638.
- Klausner, J. F., Mei, R., Bernhard, D. M., & Zeng, L. Z. (1993). Vapor bubble departure in forced convection boiling. *International Journal of Heat and Mass Transfer*, 36(3), 651-662.
- Kunkelmann, C., & Stephan, P. (2010). Numerical simulation of the transient heat transfer during nucleate boiling of refrigerant HFE-7100. *International Journal of Refrigeration*, 33(7), 1221-1228.
- Legendre, D., Magnaudet, J., & Mougin, G. (2003). Hydrodynamic interactions between two spherical bubbles rising side by side in a viscous liquid. *Journal of Fluid Mechanics*, 497, 133-166.
- Li, D., & Dhir, V. K. (2007). Numerical Study of Single Bubble Dynamics During Flow Boiling. *Journal of Heat Transfer*, 129(7), 864.
- Ling, K., Son, G., Sun, D.-L., & Tao, W.-Q. (2015). Three dimensional numerical simulation on bubble growth and merger in microchannel boiling flow. *International Journal of Thermal Sciences*, 98, 135-147.
- Liu, Q., & Palm, B. (2016). Numerical study of bubbles rising and merging during convective boiling in micro-channels. *Applied Thermal Engineering*, 99, 1141-1151.
- Liu, Q., Palm, B., & Anglart, H. (2012). *Simulation on the flow and heat transfer characteristics of confined bubbles in micro-channels*. Paper presented at the ASME 2012 10th International Conference on Nanochannels, Microchannels, and Minichannels collocated with the ASME 2012 Heat Transfer Summer Conference and the ASME 2012 Fluids Engineering Division Summer Meeting.
- Liu, Q., Wang, W., & Palm, B. (2017a). Numerical study of the interactions and merge of multiple bubbles during convective boiling in micro channels. *International Communications in Heat and Mass Transfer*, 80, 10-17.
- Liu, Q., Wang, W., & Palm, B. (2017b). A numerical study of the transition from slug to annular flow in micro-channel convective boiling. *Applied Thermal Engineering*, 112, 73-81.
- Lörstad, D., & Fuchs, L. (2004). High-order surface tension VOF-model for 3D bubble flows with high density ratio. *Journal of Computational Physics*, 200(1), 153-176.
- Magnini, M. (2012). CFD Modeling of Two-Phase Boiling Flows in the Slug Flow Regime with an Interface Capturing Technique. *Doctoral thesis*.
- Magnini, M., Pulvirenti, B., & Thome, J. R. (2013a). Numerical investigation of hydrodynamics and heat transfer of elongated bubbles during flow boiling in a microchannel. *International Journal of Heat and Mass Transfer*, 59(0), 451-471.
- Magnini, M., Pulvirenti, B., & Thome, J. R. (2013b). Numerical investigation of the influence of leading and sequential bubbles on slug flow boiling within a microchannel. *International Journal of Thermal Sciences*, 71, 36-52.
- Maqbool, M. H., Palm, B. (2012). *Flow boiling of ammonia and propane in mini channels*. KTH.
- Mukherjee, A., & Kandlikar, S. G. (2005). Numerical simulation of growth of a vapor bubble during flow boiling of water in a microchannel. *Microfluidics and Nanofluidics*, 1(2), 137-145.

- Nichita, B. A., Zun, I., & Thome, J. R. (2010). A Level Set Method Coupled With a Volume of Fluid Method for Modeling of Gas-Liquid Interface in Bubbly Flow. *Journal of Fluids Engineering*, 132(8), 081302.
- Nourgaliev, R., Wiri, S., Dinh, N., & Theofanous, T. (2005). On improving mass conservation of level set by reducing spatial discretization errors. *International Journal of Multiphase Flow*, 31(12), 1329-1336.
- Okawa, T., Ishida, T., Kataoka, I., & Mori, M. (2005). An experimental study on bubble rise path after the departure from a nucleation site in vertical upflow boiling. *Experimental Thermal and Fluid Science*, 29(3), 287-294.
- Olsson, E., & Kreiss, G. (2005). A conservative level set method for two phase flow. *Journal of Computational Physics*, 210(1), 225-246. doi: 10.1016/j.jcp.2005.04.007
- Osher, S. (1993). A Level Set Formulation for the Solution of the Dirichlet Problem for Hamilton-Jacobi Equations. *Siam Journal on Mathematical Analysis*, 24(5), 1145-1152.
- Owhaib, P. (2009). Experimental Heat Transfer, Pressure Drop, and Flow Visualization of R 134a in Vertical MiniMicro Tubes. *PhD Thesis*.
- Qu, W., & Mudawar, I. (2003). Flow boiling heat transfer in two-phase micro-channel heat sinks—II. Annular two-phase flow model. *International Journal of Heat and Mass Transfer*, 46(15), 2773-2784.
- Renardy, Y., & Renardy, M. (2002). PROST: A Parabolic Reconstruction of Surface Tension for the Volume-of-Fluid Method. *Journal of Computational Physics*, 183(2), 400-421.
- Rohsenow, W. M. (1951). A method of correlating heat transfer data for surface boiling of liquids: Cambridge, Mass.: MIT Division of Industrial Cooperation,[1951].
- Ruzicka, M. (2000). On bubbles rising in line. *International Journal of Multiphase Flow*, 26(7), 1141-1181.
- Ruzicka, M. (2005). Vertical stability of bubble chain: Multiscale approach. *International Journal of Multiphase Flow*, 31(10), 1063-1096.
- Scriven, L. E. (1959). On the dynamics of phase growth. *Chemical Engineering Science*, 10(1-2), 1-13.
- Shah, M. (1982). Chart correlation for saturated boiling heat transfer: equations and further study. *ASHRAE Trans.:(United States)*, 88(CONF-820112-).
- Siedel, S., Cioulachtjian, S., & Bonjour, J. (2008). Experimental analysis of bubble growth, departure and interactions during pool boiling on artificial nucleation sites. *Experimental Thermal and Fluid Science*, 32(8), 1504-1511.
- Son, G., Dhir, V., & Ramanujapu, N. (1999). Dynamics and heat transfer associated with a single bubble during nucleate boiling on a horizontal surface. *Journal of Heat Transfer*, 121(3), 623-631.
- Son, G., & Hur, N. (2002). A coupled level set and volume-of-fluid method for the buoyancy-driven motion of fluid particles. *Numerical Heat Transfer Part B-Fundamentals*, 42(6), 523-542.
- Son, G., Ramanujapu, N., & Dhir, V. K. (2002). Numerical Simulation of Bubble Merger Process on a Single Nucleation Site During Pool Nucleate Boiling. *Journal of Heat Transfer*, 124(1), 51.
- Sun, D. L., & Tao, W. Q. (2010). A coupled volume-of-fluid and level set (VOSET) method for computing incompressible two-phase flows. *International Journal of Heat and Mass Transfer*, 53(4), 645-655.
- Sun, T., Li, W., & Yang, S. (2013). Numerical simulation of bubble growth and departure during flow boiling period by lattice Boltzmann method. *International Journal of Heat and Fluid Flow*, 44, 120-129.

- Sussman, M. (2003). A second order coupled level set and volume-of-fluid method for computing growth and collapse of vapor bubbles. *Journal of Computational Physics*, 187(1), 110-136.
- Sussman, M., Fatemi, E., Smereka, P., & Osher, S. (1998). An improved level set method for incompressible two-phase flows. *Computers & Fluids*, 27(5-6), 663-680.
- Sussman, M., & Puckett, E. G. (2000). A Coupled Level Set and Volume-of-Fluid Method for Computing 3D and Axisymmetric Incompressible Two-Phase Flows. *Journal of Computational Physics*, 162(2), 301-337. doi: 10.1006/jcph.2000.6537
- Sussman, M., Smereka, P., & Osher, S. (1994). A Level Set Approach for Computing Solutions to Incompressible Two-Phase Flow. *Journal of Computational Physics*, 114(1), 146-159.
- Taylor, G. (1961). Deposition of a viscous fluid on the wall of a tube. *Journal of Fluid Mechanics*, 10(02), 161-165.
- Thome, J. R., & Collier. (1994). Flow boiling in a uniformly heated circular tube.
- Thome, J. R., Dupont, V., & Jacobi, A. M. (2004). Heat transfer model for evaporation in microchannels. Part I: presentation of the model. *International Journal of Heat and Mass Transfer*, 47(14-16), 3375-3385.
- Thome, J. R., Revellin, R., Agostini, B., & Park, J. E. (2008). Recent advances in thermal modeling of micro-evaporators for cooling of microprocessors. *Proceedings of the Asme International Mechanical Engineering Congress and Exposition 2007, Vol 8, Pts a and B*, 1583-1592.
- Tibirica, C. B., & Ribatski, G. (2014). Flow patterns and bubble departure fundamental characteristics during flow boiling in microscale channels. *Experimental Thermal and Fluid Science*, 59, 152-165.
- Tryggvason, G., Bunner, B., Esmaeeli, A., Juric, D., Al-Rawahi, N., Tauber, W., . . . Jan, Y. J. (2001). A Front-Tracking Method for the Computations of Multiphase Flow. *Journal of Computational Physics*, 169(2), 708-759.
- Vadgama, B., & Harris, D. K. (2007). Measurements of the contact angle between R134a and both aluminum and copper surfaces. *Experimental Thermal and Fluid Science*, 31(8), 979-984.
- Van der Geld, C. (2009). The dynamics of a boiling bubble before and after detachment. *Heat and Mass Transfer*, 45(7), 831-846.
- van der Pijl, S. P., Segal, A., Vuik, C., & Wesseling, P. (2005). A mass-conserving Level-Set method for modelling of multi-phase flows. *International Journal for Numerical Methods in Fluids*, 47(4), 339-361. doi: Doi 10.1002/Fld.817
- Van Helden, W., Van der Geld, C., & Boot, P. (1995). Forces on bubbles growing and detaching in flow along a vertical wall. *International Journal of Heat and Mass Transfer*, 38(11), 2075-2088.
- Webb, R. L., & Gupta, N. S. (1992). A critical review of correlations for convective vaporization in tubes and tube banks. *Heat Transfer Engineering*, 13(3), 58-81.
- Welch, S. W. J., & Rachidi, T. (2002). Numerical computation of film boiling including conjugate heat transfer. *Numerical Heat Transfer Part B-Fundamentals*, 42(1), 35-53.
- Wijngaarden, L. v., & Jeffrey, D. (1976). Hydrodynamic interaction between gas bubbles in liquid. *Journal of Fluid Mechanics*, 77(01), 27-44.
- Wu, D., Marcinichen, J. B., & Thome, J. R. (2013). Experimental evaluation of a controlled hybrid two-phase multi-microchannel cooling and heat recovery system driven by liquid pump and vapor compressor. *International Journal of Refrigeration*, 36(2), 375-389.

- Yang, X., James, A. J., Lowengrub, J., Zheng, X., & Cristini, V. (2006). An adaptive coupled level-set/volume-of-fluid interface capturing method for unstructured triangular grids. *Journal of Computational Physics*, 217(2), 364-394.
- Young, T. (1805). An essay on the cohesion of fluids. *Philosophical Transactions of the Royal Society of London*, 95, 65-87.
- Youngs, D. L. (1982). Time-dependent multi-material flow with large fluid distortion. *Numerical methods for fluid dynamics*, 24(2), 273-285.
- Zhang, L., & Shoji, M. (2003). Nucleation site interaction in pool boiling on the artificial surface. *International Journal of Heat and Mass Transfer*, 46(3), 513-522.